

# Contents

2	<b>1 Introduction</b>	<b>3</b>
3	<b>2 Pixel detectors</b>	<b>5</b>
4	2.1 Signal formation . . . . .	5
5	2.2 Charge Coupled Devices . . . . .	7
6	2.3 Hybrid pixels . . . . .	7
7	2.4 CMOS MAPS and DMPAS . . . . .	9
8	2.4.1 DMAPS: large and small fill factor . . . . .	10
9	2.4.2 A modified sensor . . . . .	11
10	2.5 Analog front end . . . . .	13
11	2.5.1 Preamplifier . . . . .	13
12	2.6 Readout logic . . . . .	14
13	<b>3 Use of pixel detectors</b>	<b>17</b>
14	3.1 Tracking in HEP . . . . .	17
15	3.1.1 Hybrid pixels at LHC and at SuperKEKB . . . . .	18
16	3.1.2 First attempts to MAPS . . . . .	21
17	3.2 Other applications . . . . .	23
18	3.2.1 Applicability to FLASH radiotherapy . . . . .	23
19	<b>4 TJ-Monopix1</b>	<b>28</b>
20	4.1 The sensor . . . . .	29
21	4.2 Front end . . . . .	31
22	4.2.1 ALPIDE-like . . . . .	32
23	4.3 Readout logic . . . . .	33
24	<b>5 Arcadia-MD1</b>	<b>37</b>
25	5.1 The sensor . . . . .	37
26	5.2 Readout logic and data structure . . . . .	38
27	5.2.1 Matrix division and data-packets . . . . .	38
28	<b>6 Characterization</b>	<b>41</b>
29	6.1 TJ-Monopix1 characterization . . . . .	41
30	6.1.1 Threshold and noise: figure of merit for pixel detectors . . . . .	41
31	6.1.2 Linearity of the ToT . . . . .	45
32	6.1.3 Calibration of the ToT . . . . .	47
33	6.1.4 Changing the bias . . . . .	50
34	6.1.5 Measurements with radioactive sources . . . . .	52

35	6.1.6	Dead time measurements . . . . .	53
36	6.2	ARCADIA-MD1 characterization . . . . .	55
37	<b>7</b>	<b>Test beam measurements</b>	<b>56</b>
38	7.1	Apparatus description . . . . .	56
39	7.1.1	Accelerator . . . . .	57
40	7.1.2	Mechanical carriers . . . . .	58
41	7.2	Measurements . . . . .	58
42	7.2.1	MIP spectrum using cosmic rays as source . . . . .	63
43	<b>A</b>	<b>Pixels detector: a brief overview</b>	<b>64</b>
44	A.1	Radiation damages . . . . .	64
45	<b>Bibliography</b>		<b>67</b>
46	Characterization of monolithic CMOS pixel sensors for charged particle detectors and		
47	for high intensity dosimetry		

<sup>48</sup> **Chapter 1**

<sup>49</sup> **Introduction**

<sup>50</sup> Since the 1980s, when the fabrication of device with very small electrodes (50-100  $\mu\text{m}$ )  
<sup>51</sup> became a practical possibility, pixel detectors have been widely employed for imaging and  
<sup>52</sup> tracking charged particles in the vertex region of experiments at accelerators. Thanks to  
<sup>53</sup> their excellent spatial resolution, today even better than 10  $\mu\text{m}$ , they allow for true three-  
<sup>54</sup> dimensional space-point determination even at high particle fluxes and in particular for  
<sup>55</sup> the identification of secondary vertices of short-lived particles such as  $\tau$  and B mesons. Re-  
<sup>56</sup> quirement imposed by accelerator are stringent and they will become even more with the  
<sup>57</sup> increase of luminosity; in this scenario CMOS Monolithic Active Pixel Sensors (MAPS),  
<sup>58</sup> based on the technology of CMOS cameras, are being developed to improve the perfor-  
<sup>59</sup> mance of the hybrid pixel detectors, which currently constitute the state-of-art for large  
<sup>60</sup> scale pixel detector, in particular by reducing the amount of material, power consumption  
<sup>61</sup> and pixel dimension. Indeed, while hybrid pixels are made by two parts, the sensor and  
<sup>62</sup> the electronics, welded together through microconnection, the MAPS integrate them all  
<sup>63</sup> on the same wafer.

<sup>64</sup> Experiments such as ALICE at LHC and STAR at RHIC have already introduced the  
<sup>65</sup> CMOS MAPS technology in their detectors. ALICE Tracking System (ITS2), upgraded  
<sup>66</sup> during the LHC long shut down in 2019-20, was the first large-area ( $\sim 10 \text{ m}^2$ ) silicon vertex  
<sup>67</sup> detector based on CMOS MAPS. Thanks to the reduction of the material budget, ITS2,  
<sup>68</sup> which uses the ALPIDE chip developed by ALICE collaboration, obtained an amazing im-  
<sup>69</sup> provement both in the position measurement and in the momentum resolution, improving  
<sup>70</sup> the efficiency of track reconstruction for particle with very low transverse momentum (by  
<sup>71</sup> a factor 6 at  $p_T \sim 0.1 \text{ GeV}/c$ ). Further advancements in CMOS MAPS technology are  
<sup>72</sup> being aggressively pursued for the ALICE ITS3 and the Belle II vertex detector upgrades  
<sup>73</sup> (both foreseen around 2026-27) and by the R&D53 collaboration for the upgrade at HL-  
<sup>74</sup> LHC, with the goals of further reducing the sensor thickness and improving the readout  
<sup>75</sup> speed of the devices, while keeping power consumption at a minimum.

<sup>76</sup> Beside tracking, the development of pixel detectors is a very active field with many  
<sup>77</sup> applications: a noteworthy example of detector originally used in particle physics, and  
<sup>78</sup> later employed mainly for medical imaging, but also in space and for art authentication, is  
<sup>79</sup> Medipix, a hybrid system developed at CERN within the Medipix collaboration. Among  
<sup>80</sup> medical applications, a possible use of CMOS MAPS could be in dosimetry: in the last few  
<sup>81</sup> years the search of radiotherapy oncological treatments with high intensity beams (FLASH  
<sup>82</sup> mode) is requiring new dosimeters, both for the therapies as well as new beam-monitors  
<sup>83</sup> (especially for focused very high energy electron beams), which are capable of deal with

84 extreme dose rate (up to 40 Gy/s).

85 I have studied the characteristics of two ALPIDE-like CMOS MAPS chips and tested  
86 them under different front end configuration. The first chip, the TJ-Monopix1 from the  
87 Monopix series, is a TowerJazz MAPS fabricated in 180 nm CMOS technology with an  
88 active area of  $1 \times 2\text{cm}^2$  (448×224 pixels) and is one of the prototypes for the Belle II vertex  
89 detector upgrade. The second chip, called Main Demonstrator-1, has an active area of  
90  $1.28 \times 1.28\text{cm}^2$  (512×512 pixels) is produced by LFoundry in 110 nm CMOS technology  
91 and designed by the ARCADIA (Advanced Readout CMOS Architectures with Depleted  
92 Integrated sensor Arrays) group; it is intended to be a general purpose device with possible  
93 use in medical scanners, space experiments, future lepton colliders and also possibly X-ray  
94 applications with thick substrates. The main differences between the two chips are in the  
95 output signal type and in the readout sequence of the matrix. Concerning the former  
96 point TJ-Monopix1 returns an analog output information, that is the time over threshold  
97 of the pulse which can be related with the charge released by the particle in the sensor,  
98 while MD1 returns only a digital information; regarding the latter, instead, TJ-Monopix1  
99 has a completely sequential readout, while MD1 grossly combines the information of the  
100 hits before the readout in order to reduce the data transmission time.

101 I have set up two test systems for the two chips in the INFN clean laboratories and  
102 characterized the devices electrically, with measurement related with the front end, the  
103 threshold, the noise and the dead time. The mean minimum stable threshold evolved  
104 through different generation of chips and at nowadays chips it is less than  $500\text{ e}^-$ , allowing  
105 thinner sensors with smaller signals: TJ-Monopix1 has proven to be in agreement with  
106 this, having a threshold of  $\sim 400\text{ e}^-$  to be compared with the  $2\text{ ke}^-$  signal expected in  
107 an epitaxial layer of  $25\text{ }\mu\text{m}$ . However this moving down requires a **rumore basso,  $\sim\text{e}^-$  in**  
108 **TJ-Monopix1.** Moreover, since one of the main challenges of MAPS are the differences  
109 between pixels, due to process parameters variation across the wafer, which make the  
110 sensor response nonuniform, I have measured the threshold and noise dispersions across  
111 the matrix, **numeri.** All these measurements are important to verify the design parameters  
112 of the chip comparing the results with the values obtained by the simulation. Moreover  
113 I have studied the response of the analog signal recorded by TJ-Monopix1, that is the  
114 time over threshold, and in order to have an absolute value in electrons of it, I performed  
115 an calibration using a Fe55 x-ray source. Then, we have tested TJ-Monopix1 at very high  
116 intensity using the electron beam of the ElectronFlash accelerator recently installed at  
117 Santa Chiara hospital in Pisa; up to now I have participated in the design of the setup  
118 needed for test beam measurement, **while the analysis of the data are going on besides a**  
119 **simulation of the going on.**

<sub>120</sub> **Chapter 2**

<sub>121</sub> **Pixel detectors**

<sub>122</sub> Pixel detectors are semiconductor detectors which are segmented in two dimensions: this  
<sub>123</sub> distinguish them from the strip detectors, such that a single plane of detector already  
<sub>124</sub> provides both the coordinates of impact of the detected particle. Their operation is based  
<sub>125</sub> on the p-n junction (fig. 2.1). A p-n junction is built by bringing in contact two n  
<sub>126</sub> and p doped silicon crystals. At the boundary, recombination of both charge carriers  
<sub>127</sub> occurs forming a region, the depletion zone, which is free of charge carriers. The charged  
<sub>128</sub> donors<sup>+</sup> and acceptor<sup>-</sup>, that remain ionised in the n-type and p-type regions, features a  
<sub>129</sub> space charge and create an electric field across the junction, causing a drift current in the  
<sub>130</sub> opposite direction to the diffusion one, through which the junction reaches an equilibrium  
<sub>131</sub> state. Assuming a constant space change, the electric field is linear and reach a maximum  
<sub>132</sub> at the boundary of the *p* and *n* layers.

<sub>133</sub> **2.1 Signal formation**

<sub>134</sub> When a charged particle passes through a pixel and loses energy by ionization only a  
<sub>135</sub> part of that energy is used to generate electron-hole pairs, since another part is used for  
<sub>136</sub> other processes, as lattice excitation. The average energy needed to create a pair at 300 K  
<sub>137</sub> in silicon is  $w_i = 3.65 \text{ eV}$ , that is more than the mean ionization energy because of the  
<sub>138</sub> interactions with phonon, since for a minimum ionizing particle (MIP) the most probable  
<sub>139</sub> value (MPV) of charge released in the semiconductor is  $0.28 \text{ keV}/\mu\text{m}$ , hence the number  
<sub>140</sub> of electrons-vacuum pairs is:

$$\langle \frac{dE}{dx} \rangle \frac{1}{w_i} \sim 80 \text{ e/h} \sim \frac{1.28 \cdot 10^{-2} fC}{\mu\text{m}} \quad (2.1)$$

<sub>141</sub> Because of the splitting of the energy depositon between the two different processes, the  
<sub>142</sub> number  $N_{e/h}$  of couples generated undergoes fluctuations that usually follow a Poisson  
<sub>143</sub> distribution; thus the fluctuations of  $N_{e/h}$  is equal to  $\sigma_{e/h} = \sqrt{N_{e/h}}$ . Under the constraint  
<sub>144</sub> of complete absorption of a particle, the energy resolution improves of a factor  $\sqrt{F}$ , where  
<sub>145</sub> F is called the Fano factor and determines the ultimate limit of energy resolution for  
<sub>146</sub> semiconductors. F is a function of the material and temperature and for silicon is equal  
<sub>147</sub> to  $\sim 0.115$ .

<sub>148</sub> In order to avoid a loss signal, it is fundamental that pairs e/h are produced in the  
<sub>149</sub> depleted region of the semiconductor, where the probability of recombination with charge  
<sub>150</sub> carriers is low. For this reason pixel detectors are commonly reverse biased: a positive  
<sub>151</sub> bias is given to the *n* electrode and a negative to the *p* in order to grow the depletion zone

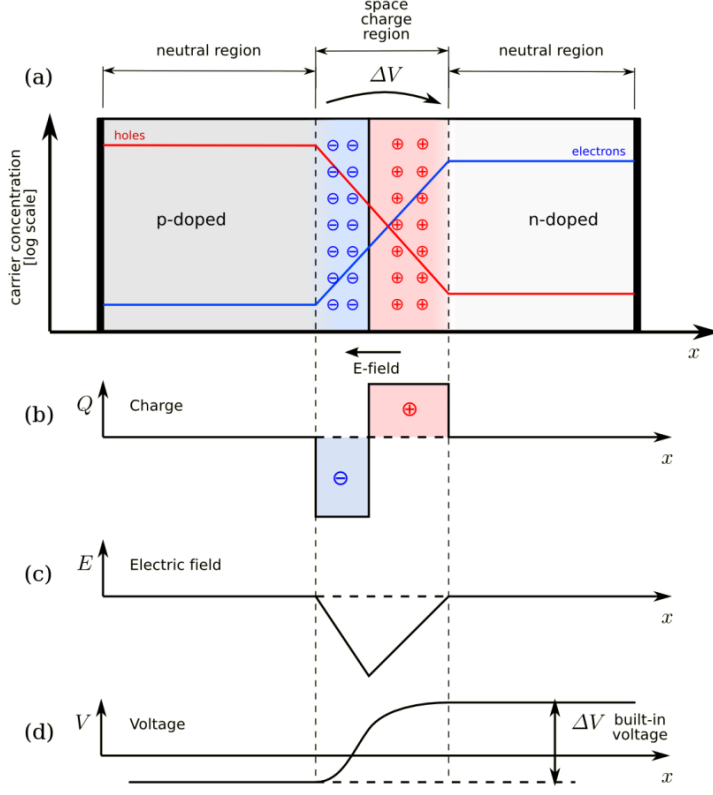


Figure 2.1: The structure of a p-n junction. (a) structure, (b) space charge density, (c) electric field distribution and (d) potential distribution.

in the epitaxial layer within the bulk. The width of the depletion region depends on the external bias  $V_{ext}$ , the resistivity  $\rho$  and also with the dopant:

$$d_n \sim 0.55 \sqrt{\frac{\rho}{\Omega cm} \frac{V_{ext}}{V}} \mu m \quad d_p \sim 0.32 \sqrt{\frac{\rho}{\Omega cm} \frac{V_{ext}}{V}} \mu m \quad (2.2)$$

Thus, high resistivity wafers ( $100 \Omega cm - k\Omega cm$ ) are typically preferred because they allow bigger depletion zone with smaller voltage bias.

The charges created within the sensor are separated by an electric field and collected at their respective electrodes ( $p$  for holes and  $n$  for electrons)<sup>1</sup>; by the drift of these charges, a signal  $i_e$  is generated on the electrode  $e$  as stated by the Shockley-Ramo's theorem:

$$i_e(t) = -q v(t) E_{WF,e} \quad (2.3)$$

where  $v(t)$  is the instantaneous velocity of the charge  $q$  and  $E_{WF}$  is the weighting field, that is the field obtained biasing the electrode  $e$  with 1V and all the others with 0V. The drift velocity of the charge depends on the electric field and on the mobility of the particle:

$$v = \mu(E) E \quad (2.4)$$

where  $\mu(E)$  is a function of the electric field and is linear in  $E$  only for small  $E$ : at higher values the probability of interactions with optical phonons increases, the mobility drops

<sup>1</sup>Even if in principle both the electrode can be used to read the signal, for pixel detectors, where the number of channel and the complexity of readout are high, only one is actually used. In strip and pad detectors, instead, is more common a dual-side readout

164 and this leads to a saturation of the velocity (fig. 2.2). Typical values for electrons and  
 165 holes mobility in silicon at room temperature are  $\mu_n \sim 1450 \text{ cm}^2/\text{Vs}$ ,  $\mu_h = 500$ .

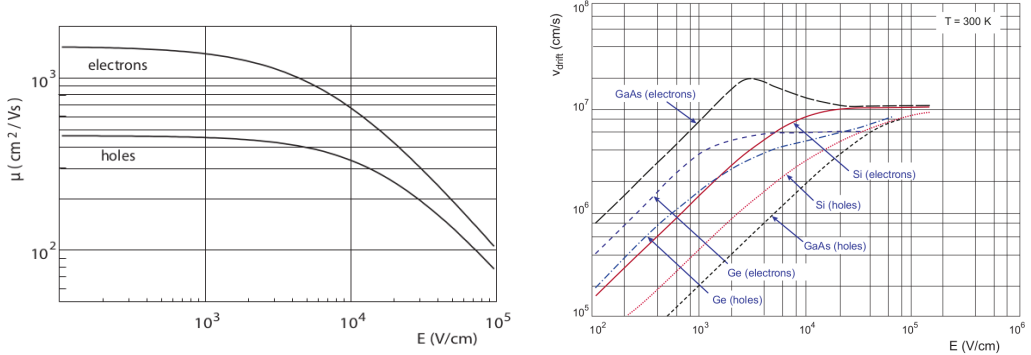


Figure 2.2: (a) Dependence of the mobility on the electric field. (b) Drift velocity at room temperature in different semiconductors

## 166 2.2 Charge Coupled Devices

167 In CCDs the charge is created in a very thin active epitaxial layer (typically 10  $\mu\text{m}$ ,  
 168 maximally about 30  $\mu\text{m}$ ) and then locally stored in a potential minimum which is created  
 169 by a MOS structure. The size of the CCD cells is typically in the range 10  $\mu\text{m}$  to 20  $\mu\text{m}$   
 170 such that spatial resolutions are of the order of a few micrometres. The collected charges  
 171 are moved stepwise from electrode to electrode (thus so called 'bucket chain') by applying a  
 172 potential with a clock with frequency of  $\sim$ MHz; despite of such high frequency, the readout  
 173 chain is completely sequential and this makes the entire process comparatively slow (tens  
 174 of ms). A particular type of CCD, the pnCCDs, are typically used to detect low energy  
 175 ( $<10$  keV) x-ray photons for their homogeneous spatial detection efficiency of photons.  
 176 The pnCCDs have a sideward depletion similar to silicon drift chambers that makes the  
 177 electric field stronger, compared with the normal CCDs. The pnCCDs designed for photon  
 178 imaging are often fabricated with high Z materials, to increase absorption efficacy.

## 179 2.3 Hybrid pixels

180 Hybrid pixels, which currently are the state-of-art technology for large scale pixel detectors  
 181 in most particle physics experiments, are made of two parts welded together through  
 182 microconnection (bump bond): the sensor and the electronics (fig. 2.3a). They provide a  
 183 practical system where the sensor and the ASIC (application specific integrated circuit)  
 184 can be optimized separately, which makes them really fast, capable of handling with rate  
 185 up to GHz. However a disadvantage of hybrid pixels is that they must be connected before  
 186 testing. For reasons related with the historical development, the n<sup>+</sup>-in-n sensors were the  
 187 first to be used; they demanded double-sided processing which guarantees the detector  
 188 functionality both before and after the type inversion of the n<sup>-</sup> doped bulk into p-type  
 189 after high quantity of radiation. The pn-diode is initially on the unstructured backside  
 190 of the sensor, while after, the depletion zone grows from the electrode side into the bulk.  
 191 This ensures that the signal can be sensed on the pixels even if the substrate is no longer  
 192 fully depleted, even though the bias voltage required for a sufficient depletion increases,

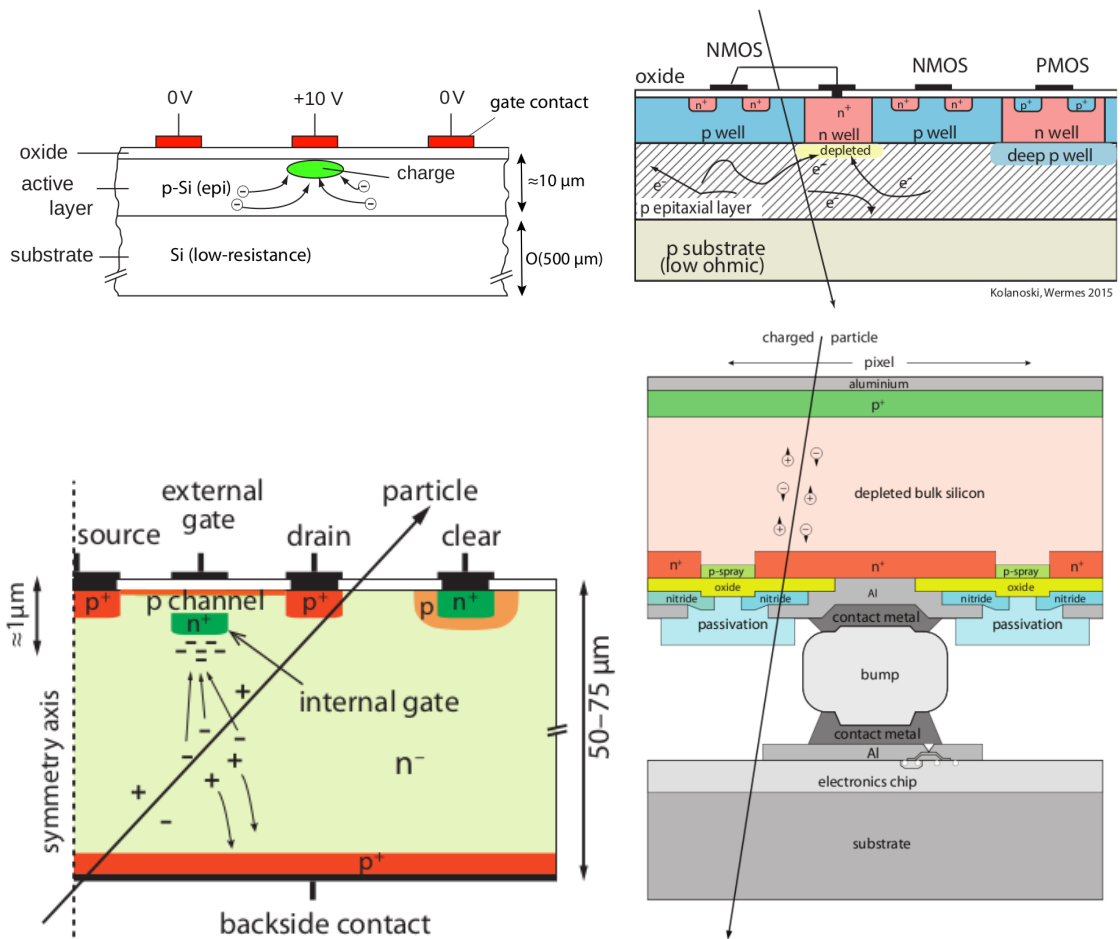


Figure 2.3: Concept cross-section of hybrid pixel (a) and of a DEPFET (b)

193 liming the detector lifetime up to a few years. With the availability of high quality p-  
194 substrate material ( $\gtrsim 2 \text{ k}\Omega\text{cm}$ ) the fabrication of n-in-p type sensors, which does not invert  
195 anymore, became the preferred choise leading also a huge advance in cost reduction due  
196 to no more need of double sided. However, the particular and sophisticated procedure to  
197 bond sensor and ASIC makes them difficult to produce, delicate (especially when exposed  
198 to high levels of radiation) and also expensive.

199 DEPFET are the first attempt towards the integration of the front end (FE) on the  
200 sensor bulk: they are typically mounted on a hybrid structure but the sensor also in-  
201 tegrates the first amplification stage. Each pixel implements a MOSFET (metal-oxide-  
202 semiconductor field-effect transistor) transistor (a p-channel in fig. 2.3b): a hole current  
203 flows from source to drain which is controlled by the external gate and the internal gate  
204 together. The internal gate is made by a deep  $n+$  implant towards which electrons drift  
205 after being created in the depletion region; the accumulation of electrons in the region  
206 underneath the n implant changes the gate potential and controls the transistor current;  
207 the removal of the signal charge from the internal gate is called "Clear". DEPFET typ-  
208 ically have a good S/N ratio: this is principally due to the amplification on-pixel, which  
209 guarantees any charge losses, and to the large depletion region. They can be operated in-  
210 dividually or integrated in the readout nodes of other detectors, as for example silicon drift  
211 chambers, but they always need to be connected to an ASIC with a readout circuit on it.  
212 In recent years, the sensor development was driven by an intensive R&D and prototyping  
213 for x-ray imagers and the ILC vertex detector.

## 214 2.4 CMOS MAPS and DMPAS

215 Monolithic active pixels accommodate on the same wafer both the sensor and the FE  
216 electronics, with the second one implanted on top within a depth of about  $1 \mu\text{m}$  below  
217 the surface. MAPS have been first proposed and realized in the 1990s and their practical  
218 usage has been enabled by the development of the electronic sector, which guarantees the  
219 halving of CMOS transistors dimension at least every two years, as stated by the Moore's  
220 law. As a matter of fact the dimension of components, their organization on the pixel  
221 area and logic density are important issues for the design and for the layout. Compared  
222 to CCDs, the readout time is dramatically reduced by the in-pixel amplification and  
223 discrimination, typically followed by a sparsified readout not requiring the signal to be  
224 transported anymore over thousands of pixels; as aside effect, the radiation tolerance is  
225 also greatly increased by sensing the signal charge directly within its own pixel.

226 A critical parameter for accelerator experiments is the material budget, which repre-  
227 sents the main limit factor for momentum measurement resolution in a magnetic field;  
228 since hybrid pixels are thicker ( $\sim$  hundreds of  $\mu\text{m}$ ) than monolithic ones (even less than  
229  $100 \mu\text{m}$ ). Using the latter the material budget can be down by a third: typical values for  
230 hybrid pixels is  $1.5 \% X_0$  per layer, while for monolithic  $0.5 \% X_0$ . Compared to MAPS,  
231 among other disadvantages of hybrid pixels there is the bigger power consumption, that  
232 requires also a bigger cooling system, leading to a futher increase of material.

233 Monolithic active pixel can be distinguished between two main categories: MAPS and  
234 depleted MAPS (DMPAS). MAPS (figure a ??) have typically an epitaxial layer in a from  
235 range  $1 \mu\text{m}$  to  $20 \mu\text{m}$  and, since they are not depleted, the charge is mainly collected by  
236 diffusion rather than by drift. This makes the path of charges created in the bulk longer  
237 than usual, making them slow (of order of  $100 \text{ ns}$ ). Moreover, the collection can be partial,

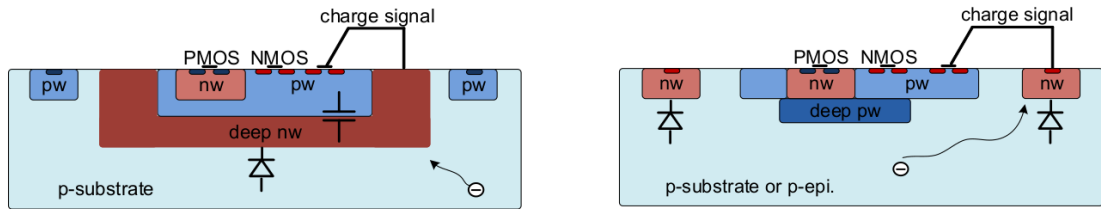


Figure 2.4: Concept cross-section with large and small fill factor

238 especially after irradiation of the detector (look at A for radiation damages), when the  
 239 trapping probability becomes higher. In figure ?? it is shown as example of CMOS MAPS:  
 240 the sensor implements an n well as collection diode; to prevent the others n wells (which  
 241 contain PMOS transistor) of the electronic circuit competing in charge collection and to  
 242 shield the CMOS circuit from the substrate, additional underlying deep p well are needed.  
 243 DMAPS are instead MAPS depleted with  $d$  typically in  $\sim 25 \mu\text{m}$  to  $150 \mu\text{m}$  (eq. 2.2) which  
 244 extends from the diode to the deep p-well, and sometimes also to the backside (in this  
 245 case if one wants to collect the signal also on this electrode, additional process must be  
 246 done).

#### 247 2.4.1 DMAPS: large and small fill factor

248 There are two different sensor-design approaches (figure 2.4) to DMAPS:

- 249 • large fill factor: a large collection electrode that is a large deep n-well and that host  
 250 the embedded electronics
- 251 • small fill factor: a small n-well is used as charge collection node

252 To implement a uniform and stronger electric field, DMAPS often uses large electrode  
 253 design that requires multiple wells (typically four including deep n and p wells); with this  
 254 layout the total capacity of the sensor increases because of the addition of a new term  
 255 (fig. 2.5), which contributes to the total amplifier input capacity ( $\sim 100 \text{ fF}$ ). In addition  
 256 to the capacity between pixels ( $C_{pp}$ ) and between the pixel and the backside ( $C_b$ ), a non-  
 257 negligible contribution comes from the capacities between wells ( $C_{SW}$  and  $C_{WW}$ ) needed  
 258 to shield the embedded electronics. These capacities affect the thermal and 1/f noise of  
 259 the charge amplifier and the  $\tau_{CSA}$  too:

$$260 \quad ENC_{thermal}^2 \propto \frac{4 kT}{3 g_m \tau_{sh}} \frac{C_D^2}{261} \quad \tau_{CSA} \propto \frac{1}{g_m} \frac{C_D}{C_f} \quad (2.5)$$

262 where  $g_m$  is the transconductance,  $\tau_{sh}$  is the shaping time. Among the disadvantages com-  
 263 ing from this large input capacity there is a coupling between the sensor and the electronics  
 264 resulting in cross talk noise on neighbouring electrodes; indeed, since digital switching in  
 265 the FE electronics does a lot of oscillations, this problem is especially connected with the  
 266 intra wells capacities. So, larger charge collection electrode sensors provide a uniform elec-  
 267 tric field in the bulk that results in short drift path and so in good collection properties,  
 268 especially after irradiation, when trapping probability can become an issue.

269 The small fill-factor variant, instead, benefits from a small capacity (5 fF to 20 fF), but  
 270 suffers from a non uniform electric field and from all the issue related to that (slowness  
 271 and high trapping probability). As we'll see these two different types of sensor require

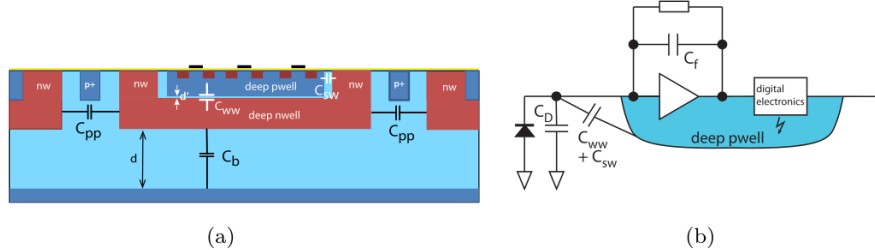


Figure 2.5:  $C_{pp}$ ,  $C_b$ ,  $C_{WW}$ ,  $C_{SW}$

	small fill factor	large fill factor
small sensor C	✓ (< 5 fF)	✗ ( $\sim 100$ 200 fF)
low noise	✓	✗
low cross talk	✓	✗
velocity performances	✓	✗ ( $\sim 100$ ns)
short drift paths	✗	✓
radiation hard	✗	✓

Table 2.1: Small and large fill factor DMAPS characteristics

270 different amplifier: the large electrode one is coupled with a charge sensitive amplifier,  
271 while the small one with a voltage amplifier (sec 2.5.1).

#### 272 2.4.2 A modified sensor

273 A process modification, developed by CERN in collaboration with the foundries, which  
274 has become the standard solution to combine the characteristics of a small fill factor  
275 sensor (small input amplifier capacity) and of a large fill factor sensor (uniform electric  
276 field), is the one carried out for ALICE upgrade about ten years [1]. A compromise  
277 between the two sensors could also be making smaller pixels, but this solution requires  
278 reducing the electronic circuit area, so a completely new pixel layout should be though.  
279 The modification consists in inserting a low dose implant under the electrode and one of  
280 its advantage lies in its versatility: in fact, both standard and modified sensor are often  
281 produced for testing.

282 Before the process modification, the depletion region extends below the diode towards  
283 the substrate, and it does not extend much laterally, even if a high bias is applied to the  
284 sensor (fig. 2.6). After the modification, two distinct pn junctions are built: one between  
285 the deep p well and the n<sup>-</sup> layer, and the other between the n<sup>-</sup> and the p<sup>-</sup> epitaxial  
286 layer, extending to the whole area of the sensor. Since deep p well and the p-substrate are  
287 separated by the depletion region, the two p electrodes can be biased separately<sup>2</sup> and this  
288 is beneficial to enhance the vertical electric field component. The doping concentration is  
289 a trimmer parameter: it must be high enough to be greater than in the epitaxial layer in  
290 order to prevent the punchthrough between p-well and the substrate, but it must also be  
291 low enough to allow the depletion for reasonable bias values.

<sup>2</sup>This is true in general, but it can be denied if other doping characteristics are implemented, and we will see that this is the case of TJ-Monopix1

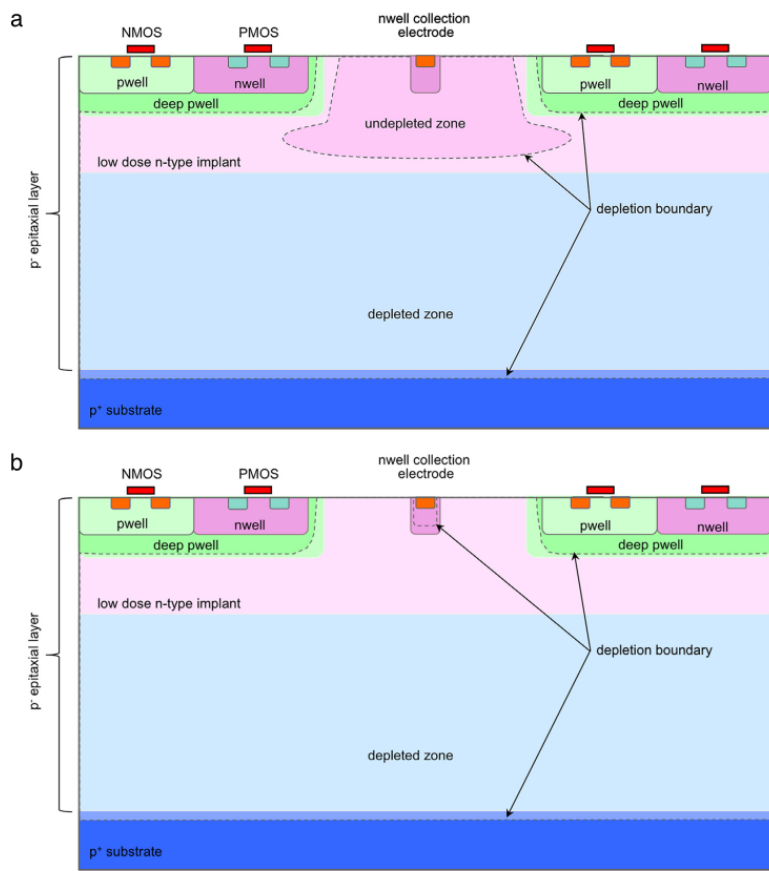


Figure 2.6: A modified process for ALICE tracker detector: a low dose n implant is used to create a planar junction. In (a) the depletion is partial, while in (b) the pixel is fully depleted.

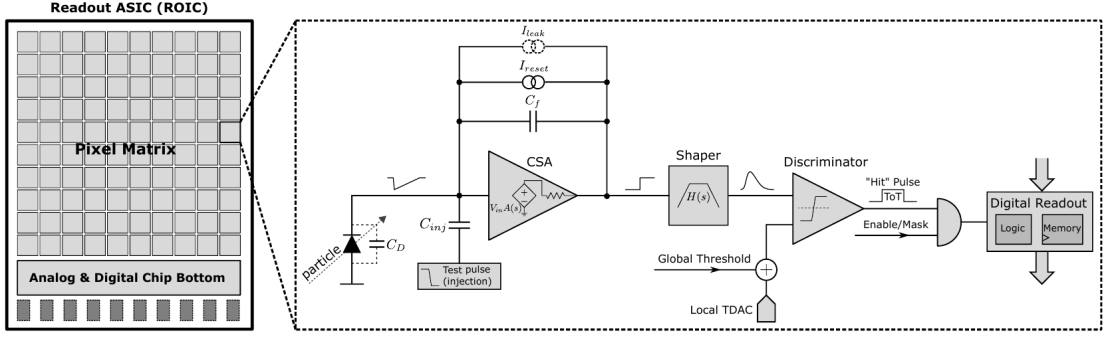


Figure 2.7: Readout FE scheme: in this example the preamplifier is a charge sensitive one (CSA) but changing the capacitive feedback into a resistive one, this can be converted in a voltage or current amplifier.

## 2.5 Analog front end

After the creation of a signal on the electrode, the signal enters the front end circuit (fig.2.7), ready to be molded and transmitted out of chip. Low noise amplification, fast hit discrimination and an efficient, high-speed readout architecture, consuming as low power as possible, are the goal of the readout integrated electronics (ROIC). The main parts of the analog front end chain are a preamplifier (that often is the only amplification stage) with a reset to the baseline mechanism and a leakage current compensation, a shaper (a band-pass filter) and finally a discriminator. The whole chain must be optimized and tuned to improve the S/N ratio. It is very important both not to have a large noise before the amplification stage in order to not multiply that noise, and chose a reasonable threshold of the discriminator to cut noise-hits much as possible.

### 2.5.1 Preamplifier

Even if circuits on the silicon crystal are only constructed by CMOS, a preamplifier can be processed as an operational amplifier (OpAmp) where the gain is determined by the input and feedback impedance (first step in figure 2.7):

$$G = \frac{v_{out}}{v_{in}} = \frac{Z_f}{Z_{in}} \quad (2.6)$$

Depending on whether a capacity or a resistance is used as feedback, respectively a charge or a voltage amplifier is used: if the voltage input signal is large enough and has a sharp rise time, the voltage sensitive preamplifier is preferred. Consequently, this flavor doesn't suit to large fill factor MAPS whose signal is already high enough:  $v_{in} = Q/C_D \approx 3 \text{ fC}/100 \text{ pF} = 0.03 \text{ mV}$ , but it's fine for the small fill factor ones:  $v_{in} = Q/C_D \approx 3 \text{ fC}/3 \text{ pF} = 1 \text{ mV}$ .

In the case of a resistor feedback, if the signal duration is longer than the discharge time ( $\tau = R_S C_D$ ) of the detector the system works as current amplifier, as the signal is immediately transmitted to the amplifier; in the complementary case (signal duration longer than the discharge time) the system integrates the current on the  $C_D$  and operates as a voltage amplifier.

## 318 2.6 Readout logic

319 The readout logic includes the part of the circuit which takes the FE output signal, pro-  
 320 cesses it and then transmit it out of pixel and/or out of chip; depending on the situation  
 321 of usage different readout characteristics must be provided. To store the analogical in-  
 322 formation (i.e. charge collected, evolution of signal in time, ...) big buffers and a large  
 323 bandwidth are needed; the problem that doesn't occur, or better occur only with really  
 324 high rate, if one wants record only digital data (if one pixel is hit 1 is recorded, and if not  
 325 0 is recorded).

326 A common compromise is to store the time over threshold (ToT) of the pulse in clock  
 327 cycle counts; this needs of relatively coarse requirement as the ToT can be trimmed down  
 328 to use only a dozen bits but, being correlated (and hopefully linear) with the deposited  
 329 charge, it provides a sufficient information. The ToT digitalization usually takes advantage  
 330 of the distribution of a clock (namely BCID, bunch crossing identification) on the pixels'  
 331 matrix. The required timing precision is better than  $\sim 25$  ns, that corresponds to the period  
 332 between bunch collisions at LHC; for such reason a reasonable BCID-clock frequency for  
 pixels detector is 40 MHz.

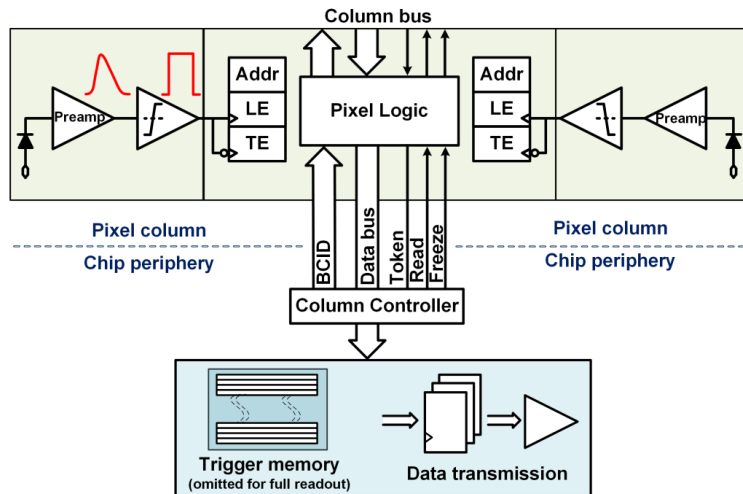


Figure 2.8: Column drain R/O scheme where ToT is saved

333 Moreover, the readout architecture can be full, if every hit is read, or triggered, if a  
 334 trigger system decides if the hit must be stored or not. On one hand the triggered-readout  
 335 needs buffers and storage memories, on the other the full readout, because there is no  
 336 need to store hit data on chip, needs an high enough bandwidth. A triggered readout is  
 337 fundamental in accelerator experiments where the quantity of data to store is very large  
 338 and some selection has to be applied by the trigger: to give an order of magnitude, at LHC  
 339 more than 100 TBit/s of data are produced, but the storage limit is about 100 MBit/s  
 340 [2](pag. 797). Typically, the trigger signal is processed in a few  $\mu s$ , so the pixel gets it  
 341 only after a hundred clock cycles from the hit arrival time: the buffer depth must be able  
 342 to handle such high trigger latency.

344 After having taken out the data from the pixel, it has to be transmitted to the end  
 345 of column (EoC) where a serializer delivers it out of chip, typically to an FPGA. There  
 346 are several ways of transmitting data from a pixel to the EoC: one of the most famous  
 347 is the column-drain read out, developed for CMS and ATLAS experiments [3]. All the

348 pixels in a double-column share a data bus and only one pixel at a time, according to  
 349 a priority chain, can be read. The reading order circuit is implemented by shift register  
 350 (SR): when a hit arrives, the corresponding data, which can be made of timestamp and  
 351 ToT, is temporarily stored on a RAM until the SR allows the access to memory by data  
 352 bus. Even if many readout architectures are based on the column-drain one, it doesn't suit  
 353 for large size matrices. The problem is the increasing number of pixels on a column would  
 354 also raise the number of pixels in the priority chain, which would result in a slowdown of  
 355 the readout.

356 If there isn't any storage memory, the double-column behaves as a single server queue  
 357 and the probability for a pixel of waiting a time  $T$  greater than  $t$ , with an input hit rate  
 358 on the column  $\mu$  and an output bandwidth  $B_W$  is [4]:

$$P(T > t) = \frac{\mu}{B_W} e^{-(B_W - \mu)t} \quad (2.7)$$

359 To avoid hit loss (let's neglect the contribution to the inefficiency of the dead time  $\tau$  due  
 360 to the AFE), for example imposing  $P_T > t \sim 0.001$ , one obtains  $(B_W - \mu) t_t \sim 6$ , where  
 361  $t_t$  is the time needed to transfer the hit; since  $t_t$  is small, one must have  $B_W \gg \mu$ , that  
 means a high bandwidth [4].

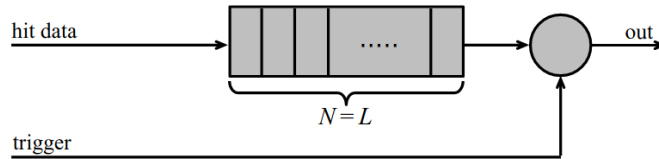


Figure 2.9: Block diagram of a pipeline buffer: N is the dimension of memory buffer and L is the trigger latency expressed in BCID cycles

362 Eq.2.7 is actually an approximation, since each pixel sees a different bandwidth de-  
 363 pending on the position on the queue: the first one sees the full bandwidth, while the next  
 364 sees a smaller one because it can be occasionally blocked by the previous pixel. Then,  
 365 the bandwidth seen by the pixel  $i$  is  $B_i = B - \sum_j \mu_j$ , where  $\mu_j$  is the hit rate of the  $j$ th  
 366 pixel. The efficiency requirement on the bandwidth and the hit rate becomes:  $B_{W,i} > \mu_i$ ,  
 367 where the index  $i$  means that the constraint is for a single pixel; if all the N pixels on a  
 368 column have the same rate  $\mu = N\mu_i$ , the condition reduces to  $B_W > \mu$ . The bandwidth  
 369 must be chosen such that the mean time between hits of the last pixel in the readout chain  
 370 is bigger than that. In order to reduce the bandwidth, a readout with zero suppression  
 371 on pixel is typically employed; this means that only information from channels where the  
 372 signal exceeds the discriminator threshold are stored.

374 If, instead, the signal is locally stored until a trigger signal arrives, the input rate to  
 375 column bus  $\mu'$  is reduced compared to the hit rate  $\mu$  as:  $\mu' = \mu \times r \times t$ , where  $r$  is the  
 376 trigger rate and  $t$  is the bunch crossing period. In this situation there is a more relaxed  
 377 constraint on the bandwidth, but the limiting factor is the buffer depth: the amount of  
 378 memory designed depends both on the expected rate  $\mu$  and on the trigger latency  $t$  as  
 379  $\propto \mu \times t$ , which means that the higher the trigger latency the lower the hit rate to cope  
 380 with.

381 In order to have an efficient usage of memory on pixels' area it's convenient grouping  
 382 pixels into regions with shared storage. Let's compare two different situations: in the first  
 383 one a buffer is located on each pixel area, while in the second one a core of four pixels

<sup>384</sup> share a common buffer (this architecture is commonly called FE-I4).

Consider a 50 kHz single pixel hits rate and a trigger latency of 5  $\mu s$ , the probability of

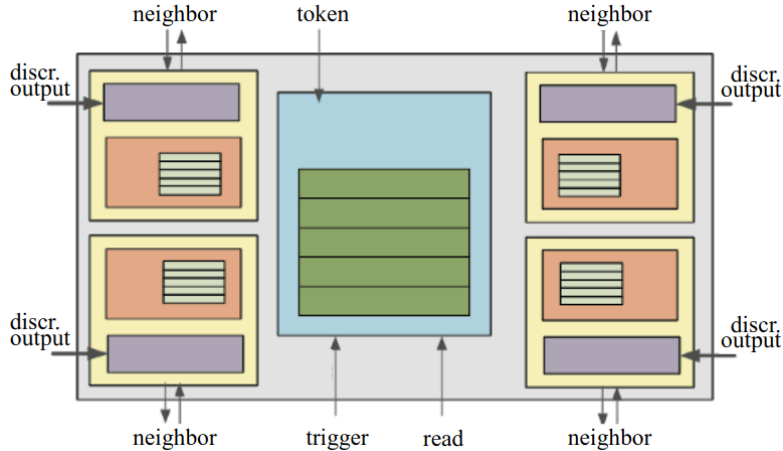


Figure 2.10: Block diagram of the FE-I4 R/O. Read and memory management section is highlighted in light blue; latency counters and trigger management section are highlighted in green; hit processing blocks are highlighted in purple; ToT counters and ToT management units are highlighted in orange

<sup>385</sup>

<sup>386</sup> losing hits is:

$$P(N > 1|\nu) = 1 - P(N = 0|\nu) - P(N = 1|\nu) = 1 - e^{-\nu}(1 + \nu) \approx 2.6\% \quad (2.8)$$

<sup>387</sup> where I have assumed a Poissonian distribution with mean  $\nu = 0.25$  to describe the counts  
<sup>388</sup> N.

<sup>389</sup> To get an efficiency  $\epsilon$  greater than 99.9 % a 3 hit depth buffer is needed:

$$P(N > 3|\nu) = 1 - \sum_{i=0}^3 P(N = i|\nu) < 0.1\% \quad (2.9)$$

<sup>390</sup> Consider the second situation: if the average single pixel rate is still 50 kHz, grouping four  
<sup>391</sup> pixels the mean number of hits per trigger latency is  $\nu = 0.25 \times 4 = 1$ . To get an efficiency  
<sup>392</sup> of 99.9% (eq. 2.9) a buffer depth of 5 hits in the four-pixels region, instead of 3 per pixels,  
<sup>393</sup> is needed.

394 **Chapter 3**

395 **Use of pixel detectors**

396 There always was a tight relation between the development of cameras and pixel detectors since 1969, when the idea of CCDs, thanks to whom Boyle and Smith were awarded  
397 the Nobel Prize in Physics in 2009, revolutionized photography allowing light to be captured electronically instead of on film. Even though the CMOS technology was already  
398 known when CCDs spread, the costs of productions were too high to allow the diffusion  
399 of these sensors for which would take almost 20 years. From that period on, the  
400 fast diffusion of CMOS was mainly due to the less cost than CCD, and the less power  
401 supply required. Nowadays CCDs are still preferred over MAPS in astronomy, where the  
402 astronomical sources' rate are low enough to cope with slow readout time (tens of ms).  
403

404 The principal use cases of pixel detectors are particle tracking and imaging: in the  
405 former case individual charged particles have to be identified, in the latter instead an  
406 image is obtained by the usually un-triggered accumulation of the impinging radiation.  
407 Also the demands on detectors performance depends on their usage, in particular tracking  
408 requires high spatial resolution, fast readout and radiation hardness.  
409

410 **3.1 Tracking in HEP**

411 At first the physics world overlooked the CCDs, and all pixel in general, as against the  
412 gaseous detector for tracking: there was no need to replace these ones which had a sufficient  
413 good resolution ( $100\text{ }\mu\text{m}$ ). Since 1974, with the measurement of the invariant mass of the  
414 J/Psi and the affirmation of the quark model, all experiments start to look for better  
415 spatial resolutions in order to achieve the possibility of reconstructing short lived particle.

416 Historically, the first pixel detector employed in particle physics was a CCD: it was  
417 installed in the spectrometer at the CERN's Super Proton Synchrotron (SPS) by the  
418 ACCMOR Collaboration (Amsterdam, CERN, Cracow, Munich, Oxford, RAL) at mid  
419 1980s, with the purpose of studying the (at the time) recently-discovered charm particles.  
420 The second famous usage of CCDs took place at SLAC in the Large Detector (SLD) during  
421 the two years 1996-98, where the CCD technology was adopted instead of the microstrip  
422 detectors for their excellent spatial resolution (cell size  $22\times 22\text{ }\mu\text{m}^2$  giving a resolution of  
423  $\sim 5\text{ }\mu\text{m}$ ) thanks to the sufficient time for readout between two successive collisions (160 ms).

424 From that period on particle tracking in experiments have been transformed radically:  
425 it was mandatory for HEP experiments to build an inner vertex detector, where the general  
426 tasks are:

- 427 • pattern recognition with the identification of particle tracks at large backgrounds and

428 pile-up

- 429 • measurement of vertices (primary and secondary)
- 430 • multi-track and vertex separation in the core of jets
- 431 • measurement of specific ionization
- 432 • momentum measurement combining with other detectors informations

433 In 1991, the more demanding environments led to the development of hybrid pixel  
434 detectors: a dedicated collaboration, RD19, was established at CERN with the specific goal  
435 of defining a semiconductor micropattern detector with an incorporated signal processing  
436 at a microscopic level. In those years a wide set of prototypes of hybrid pixel has been  
437 manufactured; among the greatest productions a mention goes to the huge ATLAS and  
438 CMS vertex detectors. From the middle of 2013 a second collaboration, RD53, has been  
439 established with the new goal of finding a pixel detector suitable for phase II future  
440 upgrades of those experiments. Even if the collaboration is specifically focused on design  
441 of hybrid pixel readout chips (aiming to 65 nm tecnique so that the electronics fits within  
442 the pixel area), also other options have been taken in account and many test have been done  
443 on MAPS. Requirements imposed by HL-LHC will become tigher in time: for example, a  
444 dose and radiation of 5 Mrad and  $10^{16}$ NIEL are exepected after 5 years of operation. Time  
445 resolution, material budget and power consumption are also issues for the upgrade: to  
446 distinguish different events from different bunches a time resolution better than 25 ns for  
447 a bunch crossing frequency of 40 MHz is required, and also a material budget lower than  
448 2% and a power consuption lower than 500 mW/cm<sup>2</sup> are required.

449 Amidst the solutions proposed 3D silicon detector, invented by Sherwood Parker in  
450 1995, and MAPS are the most promising. In 3D sensors the electrode is a narrow column  
451 of n-type implanted vertically across the bulk instead of being implanted on the wafer's  
452 surface. The charge produced by the impinging particle is then drifted transversally within  
453 the pixel, and, as the mean path between two electrode can be soufficent low, the trap  
454 probability is not an issue. Even if 3D detector are adequately radiation hard and are a  
455 strong contender for hybrid pixel modules, especially in the innermost pixel detector layer,  
456 the fabrication process is currently low volume, making them unlikely to cover large areas.

### 457 3.1.1 Hybrid pixels at LHC and at SuperKEKB

#### 458 **ATLAS**

459 With CMS, ATLAS is one of two general-purpose detectors at the LHC and has the largest  
460 volume detector ever constructed for a particle collider (46 m long and 25 m in diameter).  
461 The Inner Tracker (ITk) consists of three different systems all immersed in a magnetic  
462 field parallel to the beam axis whose main components are: the pixel, the micro-strips and  
463 transition radiation trackers. Concerning the pixel detector, they installed a 3-layer hybrid  
464 pixel detector in 2007 and an additional one inserted within the original detector envelope  
465 and therefore called insertable B-layer (IBL) in 2014. 92 million pixels are divided in 4  
466 barrel layers and 3 disks in each end-cap region, covering a total area of 1.9 m<sup>2</sup> and having  
467 a 15 kW of power consumption.

468 As stated by the ATLAS collaboration the pixel detector is exposed by an extreme  
 469 particle flux: "By the end of Run 3<sup>1</sup>, the number of particles that will have hit the  
 470 innermost pixel layers will be comparable to the number it would receive if it were placed  
 471 only a few kilometres from the Sun during a solar flare". Considering that the particle  
 472 density will increase even more with HL-LHC, radiation hardness is definitively target to  
 473 achieve. The most ambitious goal is employ a MAPS-based detector for the inner-layer  
 474 barrels, and for this reason the RD53 collaboration is designing many MAPS prototypes  
 475 (as for example TJ-Monopix1, which I will talk about in chapter 4) and performing test.  
 476 Up to now this possibility will be eventually implemented during the second phase of the  
 477 HL-LHC era, as at the start of high-luminosity operation the selected option is the hybrid  
 478 one. The sensor will be bonded with ITkPix, the first full-scale 65 nm hybrid pixel-readout  
 479 chip developed by the RD53 collaboration. Regarding the sensor, a valuable option is  
 480 using 3D pixels, which have already proved themselves in ATLAS, for the IBL, where they  
 481 were introduced in a limited acceptance range and introduced a new readout integrated  
 482 circuit called FE-I4. Also the complexity of the readout will be raised, as the number of  
 483 pixels will be increased of a factor about 7, passing from 92 millions to 6 billion.

#### 484 CMS

485 The CMS hybrid pixel detector has been upgraded in 2017, when, with the replacement  
 486 of a piece of the beam pipe, a layer has been added to the detector at 3 cm from it.  
 487 124 million pixels are divided between the barrel pixel detector (BPIX) and the forward  
 488 disks (FPIX), with sensors which are different from each other and produced by different  
 489 foundries. The sensors have an area equal to 100  $\mu\text{m}$  by 150  $\mu\text{m}$  and have been produced  
 490 on 285  $\mu\text{m}$  to 300  $\mu\text{m}$  thick wafers.

491 The time resolution is 25 ns, and the information coming from the detector are stored on  
 492 chip for the Level-1 trigger latency ( $\sim 4 \mu\text{s}$ ). The upgrade baseline ROIC was redesigned for  
 493 the outer 3 layers, replacing analog signal readout with on-chip ADCs and digital readout  
 494 at higher rate. reads out the pulse height information for each pixel.

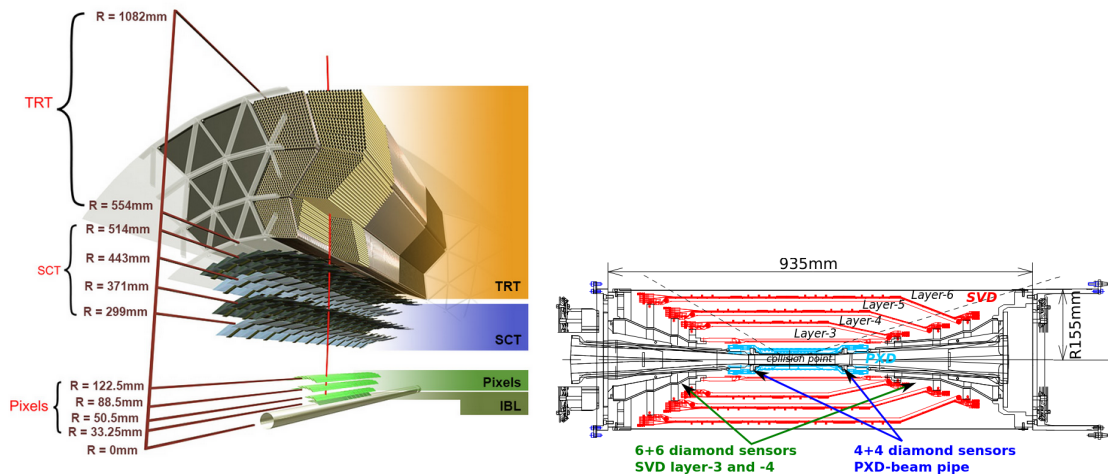


Figure 3.1: (a), (b) Since an accidental beam background enhancement can damage the VXD, diamond detectors are installed in order to monitoring it.

<sup>1</sup>Run 3 start in June 2022

495 **LHCb**

496 LHCb is a dedicated heavy-flavour physics experiment that exploits pp interactions at  
497 14 TeV at LHC. It was the last experiment to upgrade the vertex detector, the Vertex  
498 Locator (VELO), replacing the silicon-strip with 26 plane pixel detector (beacause of the  
499 fixed target geometry) in May 2022. As the instantaneous luminosity in Run3 is increased  
500 by a factor  $\lesssim 10$ , much of the readout electronics and of the trigger system have been  
501 developed in order to cope with the large interaction rate. To place the detector as close as  
502 possible to the beampipe and reach a better track reconstruction efficiency and resolution,  
503 the VELO has a surprising feature: during the injection of LHC protons it is parket at  
504 3 cm from the beams and only when the stability is reach it is moved at  $\sim 5$  mm. Readout  
505 speed is a priority for the detector that use a triggerless readout at 40 MHz collision rate,  
506 producing 20 Gbps per ROIC. The Velopix, which is the hybrid system designed for LHCb,  
507 is made bonding sensors, each measuring  $55 \times 55$  micrometers, 200  $\mu\text{m}$ -thick to a 200  $\mu\text{m}$ -  
508 thick ASIC specially developed for LHCb and coming from the Medipix family (sec. ??),  
509 which can handles hit rates up to 900 MHz per chip. Since the detector is operated under  
510 vacuum near the beam pipe, the heat removal is particularly difficult and evaporative CO<sub>2</sub>  
511 microchannel cooling are used.

512 **BelleII**

513 Due to the high background level coming from the nanobeam used at SuperKEKB in order  
514 to achieve a such high luminosity ( $4.7 \times 10^{34} \text{1/cm}^2/\text{s}$ ), silicon strip cannot be used in the  
515 inner layer of the tracker. The occupancy is too high to allow the usage of strips up to  
516 40 mm from the beam pipe. Moreover for a precise reconstruction of B-decay vertices, the  
517 usage of thin detector is mandatory at the low energy (4 GeV to 7 GeV) of the beam, in  
518 order to minimize the multiple scattering of particles.

519 The current vertex detector of BelleII, VXD, is made of a pixel detector (PXD), fab-  
520 ricated with 2 layers of DEPFET-based pixels, and 4 layers of a double-sided silicon strip  
521 detectors (SVD)[5]. Due to the small capacitance of the collection node, DEPFET presents  
522 a high signal-to-noise ratio (in 30-50) thanks to the low instrinsic noise and to the large  
523 signal achieved with he fully depleted bulk: pixels are thinned to 75  $\mu\text{m}$  in the active  
524 region, then a MIP is supposed to create a signal of  $\sim 6000 e^-$ , while the typical noise of  
525 DEPFET is around 200  $e^-$ . The ASIC read out is still based on a rolling shutter logic,  
526 with an integration time of 20  $\mu\text{s}$ . In order to reduce the data-storage memory PXD hits  
527 are only used to improve spatial resolution of tracks: the SVD informations are used by  
528 the High Level Trigger (HLT) to look for regions of interest in the pixel ladders just by  
529 extrapolating back the tracks found in the tracker detector, and this method allows to  
530 store only data belonging to these areas; the PXD hits are then used in offline track fit to  
531 improve the vertex resolution.

532 MAPS have been proposed for the replacement of VXD during the Long Shut Down  
533 2 (LSD2) foreseen around 2026-27; the new vertex detector, VTX, should be made of 5  
534 layers fabricated by the optimized Belle II pixel sensor (OBELIX), a detector based on  
535 TJ-Monopix have been selected (look at chapter ??). The main advantages VTX should  
536 bring are a obvious improving in the track and vertex resolution (14  $\mu\text{m}$  before upgrade,  
537  $\lesssim 10 \mu\text{m}$  expected after upgrade) and a reduction in the  $X_0$  (da.. a..), a higher background  
538 tolerance because of the smaller sensor than strips dimension and a low bandwidth due to  
539 the on-chip sparsification.

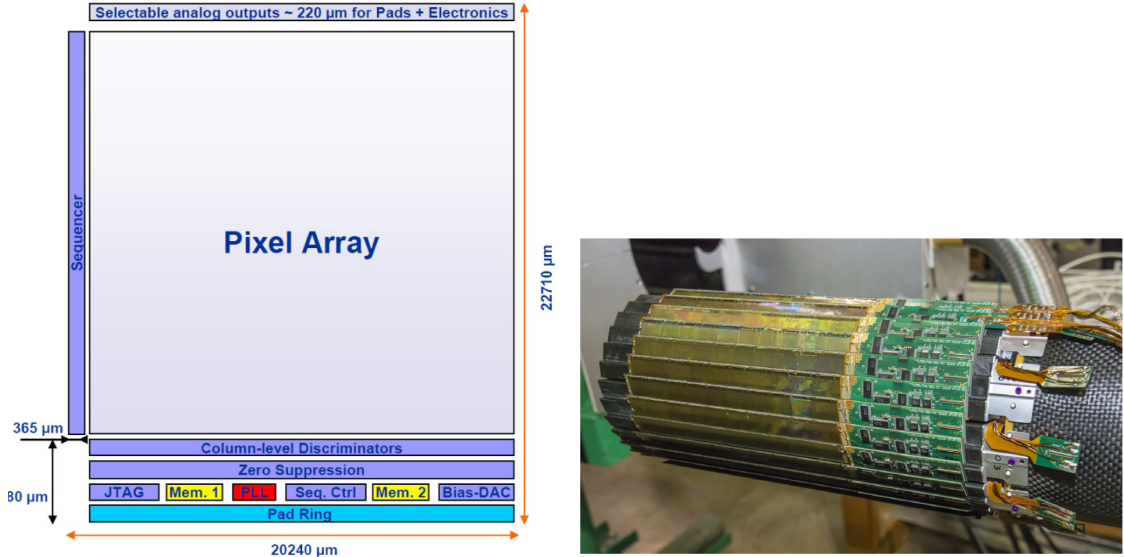


Figure 3.2: (a) The HFT PXL detector; (b) Block-diagram of the ULTIMATE-2 sensor

### 540 3.1.2 First attempts to MAPS

#### 541 MIMOSA at EUDET and STAR

542 MIMOSA [6][7] (standing for Minimum Ionizing MOS Active pixel sensor), designed in  
 543 2008, prefigured the architecture of MAPS for coming vertex detector being the first large  
 544 scale sensor to be employed as detector. MIMOSA-26 equipped the final version of EUDET  
 545 high resolution beam telescope both at CERN-SPS and at DESY while the MIMOSA-  
 546 28 devices are used for the first MAPS-based vertex detector at the STAR experiment.  
 547 MIMOSA-26 is fabricated in a 350 nm, and a module features 1152 columns, split into  
 548 18 independent groups, and 576 rows, with square pixels having a side of 18.4 μm length;  
 549 the epitaxial layer is not fully depleted and the charge collection is mostly by diffusion,  
 550 resulting in charge sharing between pixels and collection time bigger than 100 ns.

551 The readout is done in a rolling shutter mode and it is the first MAPS integrating on  
 552 chip the zero suppression: the chip is an Active Pixels (APS) and therefore it incorporates  
 553 the amplification on pixel, while the signal discrimination and zero-suppression logic are  
 554 placed at the EoC, where is also placed a memory. The chip is an Active Pixels (APS)  
 555 and therefore it incorporates the amplification on pixel, while the signal discrimination  
 556 and zero-suppression logic are placed at the EoC: the readout is done in a rolling shutter  
 557 mode with a frame integration time that can be lowered down to 85 ms, and a memory  
 558 allowing to store up to six hits is.

559 The EUDET telescope, equipped with six sensor planes, requires highly granular and  
 560 thin pixel detectors in order to achieve an excellent track resolution (around 2 μm) even at  
 561 the rather low particle energies of up to 6 GeV. The STAR experiment at the Relativistic  
 562 Heavy Ion Collide (RHIC) accelerator at the Brookhaven National Laboratory (BNL) is  
 563 the first to include MAPS in the vertex detector[8]. The main tracking detector in STAR is  
 564 a TPC with radii 60-190 cm embedded in a 0.5 T solenoidal magnetic field, that provides  
 565 a pointing resolution of approximately 1 mm. The pixel detector, PXL, is a part of a  
 566 3-detector system, Heavy Flavor Tracker (HFT), that has been added to the pre-existing  
 567 STAR apparatus just before the 2014 Run in order to improve the impact parameter

resolution and to enable the direct reconstruction of hadronic decays of heavy flavor mesons and baryons. The Heavy Flavor Tracker (HFT) is composed by the Silicon Strip Detector (SSD), the Intermediate Silicon Tracker (IST) and the Pixel Detector (PXL); the first one is placed at 22 cm from the beam pipe and consists of double sided strips with 95  $\mu\text{m}$  inter-strip pitch, the second one, placed at 14 cm, is made of single sided silicon pads with  $600 \mu\text{m} \times 6 \text{ mm}$  pitch and the last one made by two layers is placed at 2.8 cm and 8 cm fabricated with ULTIMATE2 (also known as MIMOSA-28), a successor of MIMOSA-26 sensor, with pitch 20.7  $\mu\text{m}$  and thinned down to 50  $\mu\text{m}$ . An area of  $0.16 \text{ m}^2$  are covered by 400 MAPS sensor, corresponding to 356 millions of pixels divided into array size of  $928 \times 960$ . Each pixel includes circuitry for readout, amplification, and Correlated Double Sampling (CDS) for signal extraction and noise subtraction and the frame integration time is 185.6  $\mu\text{s}$ ; after the subtraction the signal to noise ratio is  $\sim 30$ , with a noise between 10-12 electrons and a signal of  $1000 \text{ e}^-$ . Thanks to the HFT system and the PXL, STAR achieved a track pointing resolution 46  $\mu\text{m}$  for 750 MeV/c kaons, and better than 30  $\mu\text{m}$  for particle momenta bigger than 1 GeV/c: this performance enabled the study of D-meson production with a high significance signal.

#### 584 ALPIDE at ALICE

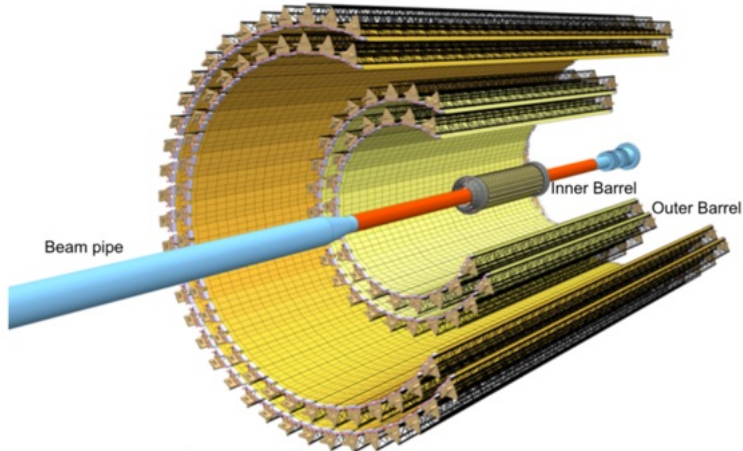


Figure 3.3

585 ALICE (A Large Ion Collider Experiment) is a detector dedicated to heavy-ion physics  
 586 at the LHC. The tracking detector consists of the Inner Tracking System (ITS), the gaseous  
 587 Time Projection Chamber (TPC) and the Transition Radiation Detector (TRD), and all  
 588 those are embedded in a magnetic field of 0.5 T. The ITS is made by six layers of detectors,  
 589 two for each type, from the interaction point outwards: Silicon Pixel Detector (SPD),  
 590 Silicon Drift Detector (SDD) and Silicon Strip Detector (SSD). Contrary to the others  
 591 LHC experiments, ALICE tracker is placed in a quite different environments: the expected  
 592 dose is smaller by two order of magnitude and the rate of interactions is few MHz instead  
 593 of 40 MHz, but the number of particles comes out of each interaction is higher (the SPS is  
 594 invested by a density of particles of  $\sim 100 \text{ cm}^{-2}$ ). The reconstruction of very complicated  
 595 events with a large number of particles is a challenge, hence to segment and to minimize  
 596 the amount of material, which may cause secondary interaction complicating further the  
 597 event topology, is considered a viable strategy.

598 ITS2, upgraded during the LHC long shut down in 2019-20, was the first large-area  
599 ( $\sim 10 \text{ m}^2$  covered by 2.5 Gpixels) silicon vertex detector based on CMOS MAPS. The  
600 detector employes the ALPIDE chip, developed by ALICE collaboration, fabricated in the  
601 180 nm CMOS Imaging Sensor process of TowerJazz, whose design takes full advantage  
602 of process feature which allows full circuitry within the pixel matrix. Thanks to the  
603 reduction of the material budget, ITS2 obtained an amazing improvement both in the  
604 position measurement and in the momentum resolution, improving the efficiency of track  
605 reconstruction for particle with very low transverse momentum (by a factor 6 at  $pT \sim$   
606 0.1 GeV/c). Further advancements in CMOS MAPS technology are being aggressively  
607 pursued for the ALICE ITS3 vertex detector upgrades (foreseen around 2026-27), with  
608 the goals of further reducing the sensor thickness and improving the readout speed (which  
609 now is completely asynchronous) of the devices, while keeping power consumption at a  
610 minimum.

### 611 3.2 Other applications

612 Historically for imaging purpose the CCDs were the favoured device: they can be used as  
613 single photon counter or integrating and collecting the charge released by more impinging  
614 particles. The utilisation in the first case is similar to the tracking one, except that the  
615 requirements are less tight, so much that two noteworthy of microchips originally meant  
616 for detectors in particle physics at the LHC, and later employed in other fields are Medipix  
617 and Timepix. They are read-out chips developed by the Medipix Collaborations since early  
618 1990s. For two decades, different Medipix generations have been produced, having a rough  
619 correlation with the feature size used: Medipix2 (1999) used 250 nm feature size CMOS  
620 while Medipix3 (2005) 130 nm. For photons imaging other materials with higher atomic  
621 charge than silicon could be preferred, as a high photon absorption efficiency is needed: it  
622 was for this reason that Medipix2 was bump bonded to identically segmented sensors of  
623 both silicon and GaAs.

624 The applications in scientific imaging vary from astrophysics and medical imaging and  
625 dosimetry to more exotic domains as studies of protein dynamics, material science, art  
626 authentication and archaeology. One of the most important employment of Medipix is as  
627 X-ray single photon counting in industrial and medical radiography and in 3D computed  
628 tomography<sup>2</sup>. Thanks to a New-Zealand company, the MARS Bioimaging detector has  
629 been fabricated, which is capable of resolving the photons energy and produce 3D coloured  
630 images. Besides tracking in HEP (I have already cited the use of Timepix3 is in the beam  
631 telescope of the LHCb VELO), an important use of Timepix is in dosimetry. **Timepix**  
632 **Detector for Imaging in Ion Beam Radiotherapy- articolo e qualche info.** A small-Timepix  
633 detector with the dimension of a USB can also be found at the International Space Station,  
634 where it is exploited for radiation, principally made of heavy-ion, monitoring.

#### 635 3.2.1 Applicability to FLASH radiotherapy

636 A possible new application of pixels detector is dosimetry or beam monitoring of charge  
637 particles in high intensity radiography. Recently<sup>3</sup> a promising method for RT at ultra high

<sup>2</sup>The analysis of the direction dependence of X-ray absorption is performed, for example, in order to obtain an image in Computed Tomography (CT)

<sup>3</sup>The first evidences have been observed on mice experiments in 1966 and in 2014 by the group of Favaudon and Vozenin. After this, many tests on cats and pigs have been performed, and also there has

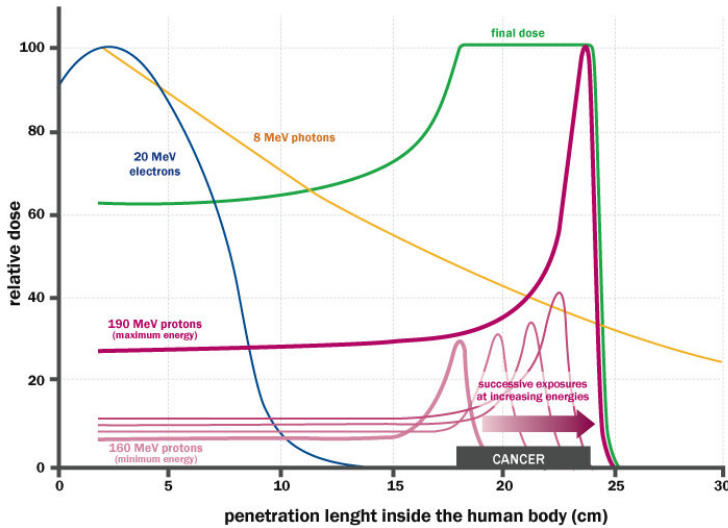


Figure 3.4: The Spread Out Bragg Peak (SOBP) curve (green), which is a constant dose distribution, is obtained from the superposition of many Bragg peak of hadrons with different energy.

638 dose rate (at least 40 Gy/s) and for this reason called FLASH-RT[9], instead of CONV-RT  
 639 (0.03 Gy/s), came out. However, finding dosimeters suitable at ultra high dose rate is still  
 640 an open issue since almost all standard online dosimeters have shown saturation problems.

#### 641 Radiotherapy

642 The radiological treatment is a common method used in 60% of tumors both as palliative  
 643 care and as treatment. It can be given before, after or during a surgery, (Intra operative  
 644 radiation therapy-IORT) and many different types of radiations (photons, electrons,  
 645 protons and ions, which mainly are hydrogen and carbon) can be used to irradiate the  
 646 affected tissues. Exploiting the ionizing energy loss, that can be parametrized by the  
 647 Linear Energy Transfer (LET), a biological damage can be delivered to the tissue: while  $\alpha$   
 648 and  $\beta$  particles are high LET radiations with values in  $100 \text{ keV}/\mu\text{m}$  to  $200 \text{ keV}/\mu\text{m}$ , x-rays  
 649 and gamma-rays are low LET radiations with values in range  $0.2 \text{ keV}/\mu\text{m}$  to  $2 \text{ keV}/\mu\text{m}$ . If  
 650 x-ray photons, with energy in 4 MeV to 25 MeV are used, the ionization is caused by the  
 651 Compton electrons and is more in the superficial layers of the tissue due to the exponential  
 652 attenuation of the beam. The hardrons energy loss, instead, is strongly localized in  
 653 the last region of the track, that is the Bragg peak, such as the the treatement typically  
 654 requires the scanning of the target. The Relative Biological Effectiveness (RBE) of ions  
 655 near th Bragg peak depends on their mass, and in particular it increases with the ion's  
 656 mass; even though, too heavy ions generally increases the damage produced also in the  
 657 entrance region. Carbon is considered the optimum between the two trends.

658 Electrons, instead, of energy in range of a dozen of MeV tend to spread out on a  
 659 bigger region of a few centimeters in both the diameter and thickness. Using Very High  
 660 Energy Electrons (VHEE) has been taken into account for irradiation of deeper tissues,  
 661 however, to date, the FLASH effect has been tested and demostrated only using low-energy

---

been a clinical trial on a cutaneous tumor-patient

	CONV-RT	FLASH-RT
Dose rate	0.03 Gy/s	40 Gy/s
Intra pulse dose rate	100 Gy/s	106 Gy/s
Treatment duration	~minutes	$\lesssim 500$ ms
Dose Per Pulse	0.3 mGy	1 Gy to 10 Gy
Pulse width	3 $\mu$ s	$\sim 2 \mu$ s

Table 3.1: Typical value of treatment parameters

662 electrons.

### 663 FLASH effect

664 This treatment takes advantages of biological differences between tumors and healthy  
 665 tissues: it is characterized by reducing normal tissue toxicity and maintaining equivalent  
 666 tumor damage. The response to dose can be described by the survival fraction probability,  
 667 describing the fraction of surviving cell as a function of the dose:

$$S(D) = S(0) e^{-(\alpha D + \beta D^2)} \quad (3.1)$$

668 where  $\alpha$  and  $\beta$  respectively represents the rate of cell killing by single ionizing events and  
 669 by double hits. Hence, at high doses the density of damages increases and the cells repair  
 670 becomes more difficult. Even if the FLASH effect is not yet completely understood and  
 671 the underlying mechanisms are not clear, it looks like there are two different recipes which  
 672 are involved:

- 673 • **The dose rate:** higher dose rate produce bigger damages (fig. 3.5(a)) since this  
 674 prevent cells from sparing.
- 675 • **The presence or absence of oxygen:** while hypoxic cells are very resistant to radi-  
 676 ation, normal oxygenated cells are highly radiosensitive. This is because if molecules  
 677 containing  $O_2$  break due to the impinging radiation, then the oxygen can build Re-  
 678 active Oxygen Species (ROS) (fig.3.5(b))

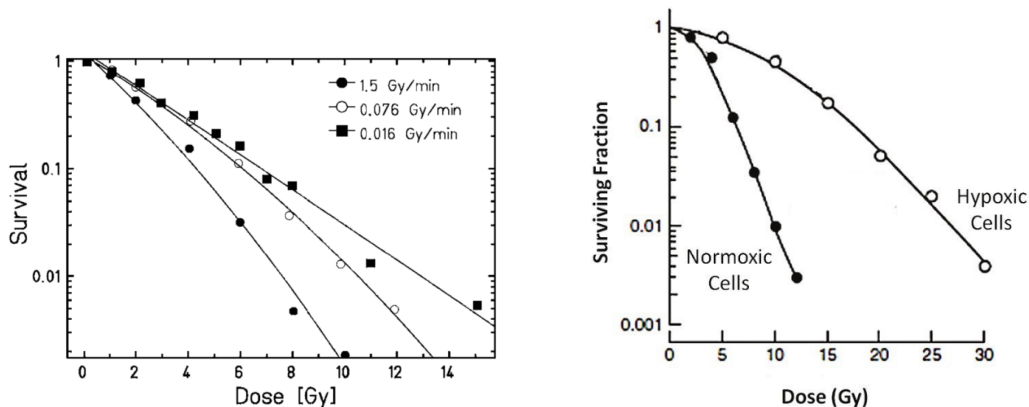


Figure 3.5: (a) Survival curve for different dose rate and (b) for different oxygen cell content

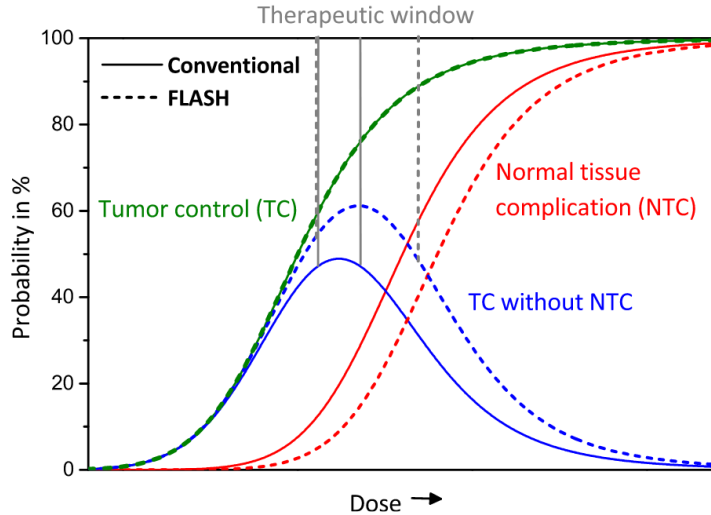


Figure 3.6: Illustration of dependence of TCP, NTCP and therapeutic window on dose, for CONV-RT ad FLASH-RT.

679 The Tumor Control Probability (TCP) and the Normal Tissue Complication (NTC) functions  
 680 parametrize respectively the efficiency of damaging on the tumor after having released  
 681 a certain dose and the probability of not affecting the healthy tissues. The intermediate  
 682 zone between the increase of the TC and of the NTC is called therapeutic window, and  
 683 the wider it is and the more effective the treatment is.

#### 684 Dosimetric problems

685 Up to now, all online dosimeters have shown saturation problems at high DDP, differently  
 686 from radiochromic films, which are the standard passive dosimeters and have shown a  
 687 dose-rate independence up to 109 Gy/s. Even though the linear response in wide dynamic  
 688 range, they do not provide any online dosimetric informations, since the time required to  
 689 extract the physical value from the reading is not instantaneous<sup>4</sup>.

690 Ionization Chambers (ICs), which are the online reference dosimeter also according to  
 691 law, at high level of radiation (already at dose per pulse two orders of magnitude lower  
 692 than the ones used for FLASH-RT) show both problems of saturation and recombination.  
 693 When a high density of ions and electrons is produced in the gas, a high counter electric  
 694 field opposed to the drift one might be generated; if a neutral region build up, both the  
 695 recombination of i/e pairs, with a subsequent photoemission and abrupt discharge can  
 696 happen<sup>5</sup>. For low level of radiation a correction factors,  $k_{sat}$ , can be introduced and a  
 697 dose measurement can still be done: with Dose Per Pulse (DDP) lower than 1 mGy the  
 698 correction factor is <5%. Non sono sicurissima di aver capito davvero il punto per quanto  
 699 riguarda i semiconduttori e gli scintillatori

700 In reference [10] are presented some results related with saturation problems at high  
 701 DDP of different types of detectors. The dosimeters tested and their value at which satura-  
 702 tion becomes are reported in table 3.2, while in figure 3.7 are reported the measurements.  
 703 The DrR is then defined as the ratio between the signal response of each dosimeters at a

<sup>4</sup>COSA sono e più o meno come funzionano

<sup>5</sup>This is called Raether-Meek condition

Commercial detector	Detector type	saturation [Gy/p]
PTW TW34045 Advanced Markus EC	ionization chamber	0.3
PTW TM60017 Dosimetry Diode E	silicon diode	0.15
PTW TW60019 microDiamond	diamond	0.15
DoseVue DoseWireTM Series 100	scintillator fiber	11-26

Table 3.2: Results obtain in [10]

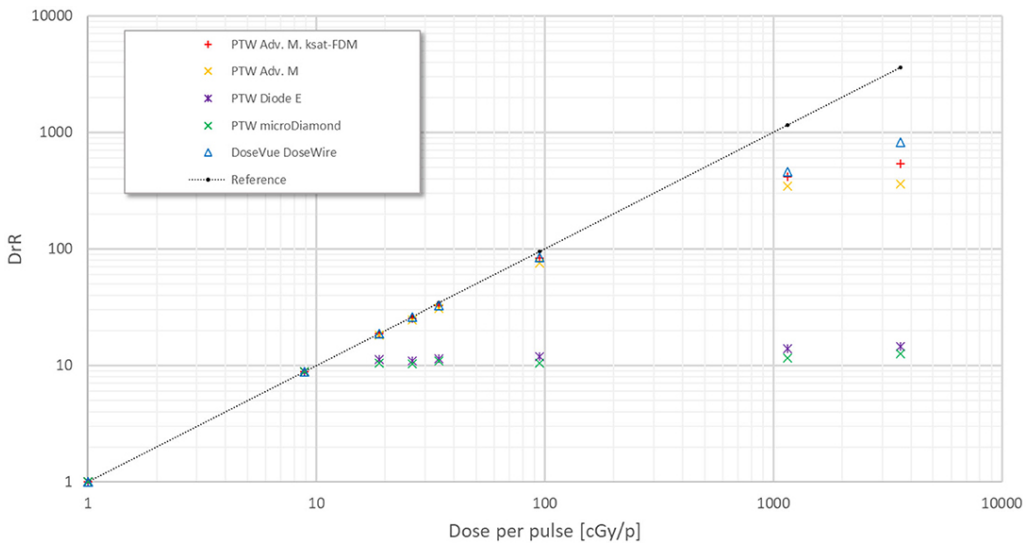


Figure 3.7: Saturation problems underlyed in [10].

704 fixed DDP of 1 cGy/p and is called dosimeter reading ratio (DrR):

$$DrR = \frac{R}{R|_{Dp=1cGy/p}} = \frac{R}{R_{ref}} \quad (3.2)$$

705 Then, for a saturation not affected by saturation problems DrR should be a straight line  
 706 with a slope equal to 1; since the reference measurements of dose has been performed with  
 707 radiochromic films (GAFCHROMIC EBT-XD), whose dose indipendence has been tested<sup>6</sup>  
 708 in range from 0 Gy to 15 Gy, the dotted black line in figure 3.7 represents the reference  
 709 measurement done with it.

710 Besides the linearity of the response, two other important requirements for beam mon-  
 711 itoring in radiotherapy are both high temporal and space resolutions. Concerning time  
 712 resolution I recall that MAPS could handle with rate up to hundreds of MHz, so the pos-  
 713 sibility application of these detectors probably strictly depends on their particular usage.  
 714 However MAPS might be well suited given that their spatial resolution and their thinness  
 715 (they can be thinned down to about 50 μm), which is an obvious requirement for beam  
 716 monitor.

---

<sup>6</sup>The radiochromic films calibration has been obtained by irradiating the films with dose values in range from 0 Gy to 15 Gy, by positioning the films in a polymethylmethacrylate (PMMA) phantom at R<sub>100</sub> depth, corresponding to 10 cm

<sup>717</sup> **Chapter 4**

<sup>718</sup> **TJ-Monopix1**

<sup>719</sup> TJ-Monopix1 is a small electrode DMAPS with fast R/O capability, fabricated by Tow-  
<sup>720</sup> erJazz foundry in 180 nm CMOS imaging process. It is part, together with prototypes  
<sup>721</sup> from other series such as TJ-MALTA, of the ongoing R&D efforts aimed at developing  
<sup>722</sup> DMAPS in commercial CMOS processes, that could cope with the requirements at ac-  
<sup>723</sup> celerator experiments. Both TJ-Monopix and TJ-MALTA series [11], produced with the  
<sup>724</sup> same technology by TowerJazz (the timeline of the foundry products is shown in figure  
<sup>725</sup> 4.1), are small electrode demonstrators and principally differ in the readout design: while  
<sup>726</sup> Monopix implements a column-drain R/O, an asynchronous R/O without any distribution  
<sup>727</sup> of BCID has been used by TJ-Malta in order to reduce power consumption.



Figure 4.1: Timeline in TowerJazz productions in 180 nm CMOS imaging process

<sup>728</sup> Another Monopix series, but in 150 nm CMOS technology, has been produced by  
<sup>729</sup> LFoundry [12]. The main differences between the LF-Monopix1 and the TJ-Monopix1  
<sup>730</sup> (summarized in table 4.2), lay in the sensor rather than in the readout architecture, as  
<sup>731</sup> both chips implements a fast column drain R/O with ToT capability [13][14]. Concerning  
<sup>732</sup> the sensors, either are based on a p-type substrate, but with slightly different resistivities;  
<sup>733</sup> in addition LFoundry pixels are larger, thicker and have a large fill factor (the very deep n-  
<sup>734</sup> well covers ~55% of the pixel area). The primary consequence is that LF-Monopix1 pixels  
<sup>735</sup> have a higher capacity resulting in higher consumption and noise. As I discussed in section  
<sup>736</sup> 2.4.1, the fact that LF-Monopix has a large fill factor electrode is expected to improve its  
<sup>737</sup> radiation hardness. Indeed, a comparison of the performance of the two chips showed that  
<sup>738</sup> TJ-Monopix suffers a comparatively larger degradation of efficiency after irradiation, due  
<sup>739</sup> to the low electric field in the pixel corner; on the other hand, a drawback of the large fill  
<sup>740</sup> factor in LF-Monopix is a significant cross-talk.

	LF-Monopix1	TJ-Monopix1
Resistivity	$>2 \text{ k}\Omega\text{cm}$	$>1 \text{ k}\Omega\text{cm}$
Pixel size	$50 \times 250 \mu\text{m}^2$	$36 \times 40 \mu\text{m}^2$
Depth	$100\text{-}750 \mu\text{m}$	$25 \mu\text{m}$
Capacity	$\sim 400 \text{ fF}$	$\sim 3 \text{ fF}$
Preamplifier	charge	voltage
Threshold trimming	on pixel (4-bit DAC)	global threshold
ToT	8 bits	6 bits
Consumption	$\sim 300 \text{ mW/cm}^2$	$\sim 120 \text{ mW/cm}^2$
Threshold	$1500 e^-$	$\sim 270 e^-$
ENC	$100 e^-$	$\sim 30 e^-$

Table 4.1: Main characteristics of Monopix1 produced by TowerJazz and LFoundry [13][14]

741        The TJ-Monopix1 chip contains, apart from the pixels matrix, all the required support  
 742        blocks used for configuration and testing:

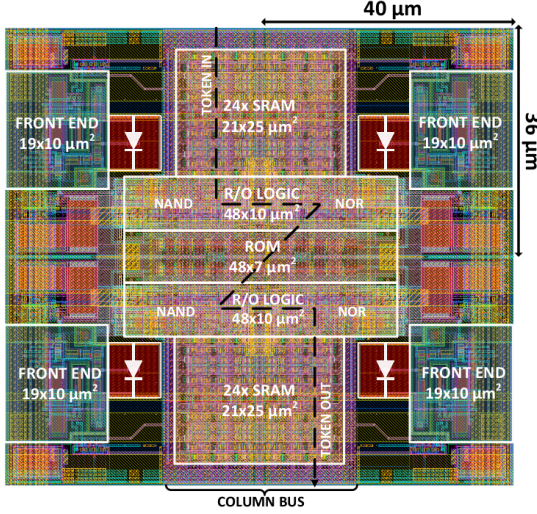
- 743        • the whole matrix contains  $224 \times 448$  pixels, yielding a total active area approximately  
 744        equal to  $145 \text{ mm}^2$  over a total area of  $1 \times 2 \text{ cm}^2$ ;
- 745        • at the chip periphery are placed some 7-bit Digital to Analog Converter (DAC), used  
 746        to generate the analog bias voltage and current levels and to configuire the FE;
- 747        • at the EoC is placed a serializer to transferred datas immediately, indeed no trigger  
 748        memory is implemented in this prototypes;
- 749        • the matrix power pads are distributed at the sides
- 750        • four pixels which have analog output and which can be monitored with an oscillo-  
 751        scope, and therefore used for testing

752        Pixels are grouped in  $2 \times 2$  cores (fig. 4.2a): this layout allows to separate the analog  
 753        and the digital electronics area in order to reduce the possible interference between the  
 754        two parts. In addition it semplifies the routing of data as pixels on double column share  
 755        the same column-bus to EoC. Therefore pixels can be addressed through the physical  
 756        column/row or through the logical column/row, as shown in fig. 4.2b: in figure is also  
 757        highlighted the token propagaion path, whose I will discuss later.

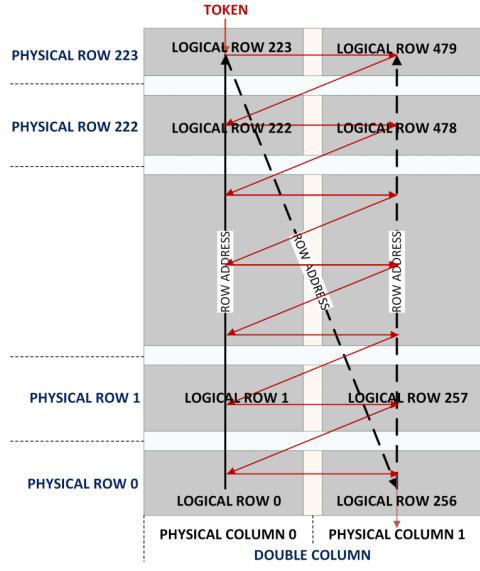
758        Concerning the integration7.7 of the chip in a readout path, TJ-Monopix1 chips have  
 759        been wire-bonded on a dedicated carrier board , the Printed Circuit Board (PCB). Two  
 760        other board between the DAQ and the chip: the General Purpose Analog Card (GPAC),  
 761        which provides power supply channels, current/voltage bias sources and I/O buffer, and  
 762        the MIO3 FPGA, which strictly interacts with the DAQ.

## 763        4.1 The sensor

764        As already anticipated, TJ-Monopix1 has a p-type epitaxial layer and a n doped small  
 765        collection electrode ( $2 \mu\text{m}$  in diameter); to avoid the n-wells housing the PMOS transistors  
 766        competing for the charge collection, a deep p-well substrate, common to all the pixel FE



(a) Layout of a core containing 4 pixels. The analog FE and the digital part are separated in order to reduce cross-talk be



(b)

Parameter	Value
Matrix size	$1 \times 2 \text{ cm}^2$
Pixel size	$36 \times 40 \mu\text{m}^2$
Depth	$25 \mu\text{m}$
Electrode size	$2 \mu\text{m}$
BCID	40 MHz
ToT-bit	6
Power consumption	$\sim 120 \text{ mW/cm}^2$

Table 4.2

area, is used. TJ-Monopix1 adopts the modification described in section 2.4.2 that allows to achieve a planar depletion region near the electrode applying a relatively small reverse bias voltage. This modification improves the efficiency of the detector, especially after irradiation, however a simulation of the electric field in the sensor, made with the software TCAD (Technology Computer Aided Design), shows that a nonuniform field is still produced in the lateral regions of the pixel compromising the efficiency at the corner. Two variations to the process have been proposed in order to further enhance the transversal component of electric field at the pixel borders: on a sample of chip, which includes the one in Pisa, a portion of low dose implant has been removed, creating a step discontinuity in the deep p-well corner (fig. 4.3); the second solution proposed[MOUSTAKAS THESY, PAG 58] consists in adding an extra deep p-well near the pixel edge. A side effect of the alteration in the low dose implant is that the separation between the deep p-well and the p-substrate becomes weak to the point that they cannot be biased separately to prevent the punchthrough.

Moreover, to investigate the charge collection properties, pixels within the matrix are split between bottom top half and bottom half and feature a variation in the coverage of the deep p-well: the electronics area can be fully covered or not. In particular the pixels

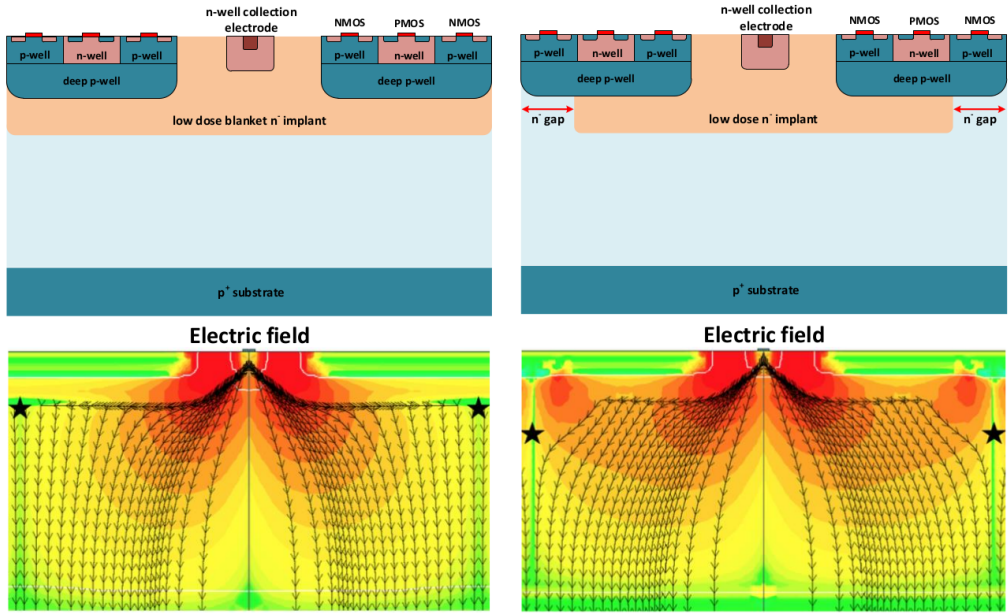


Figure 4.3: (a) The cross-section of a monolithic pixel in the TJ-Monopix with modified process; additionally in (b) a gap in the low dose implant is created to improve the collection of charge due to a bigger lateral component of the electric field. this point in figure is indicated by a star . transversal component of the electric field drops at the pixel corner

784 belonging to rows from 0 to 111 are fully covered (FDPW) and pixels belonging to rows  
 785 from 112 to 223 have a reduced p-well (RDPW), resulting in a enhancement of the lateral  
 786 component of the electric field.

## 787 4.2 Front end

788 One of the main advantage of this chip is the small collection electrode, which results in a  
 789 small capacitance ( $C_{in}=3\text{ fF}$ ) allowing for high input signal amplitude and single stage of  
 790 amplification, which obviously improves the signal to noise ratio performance of the FE.  
 791 Assuming a fully depleted epitaxial layer of  $25\text{ }\mu\text{m}$ , which corresponds approximately to  
 792 a  $20\text{ }\mu\text{m}$  of deep sensing volume, a MIP should produce  $\sim 1600\text{ e}^-$ , then:

$$V_{in} = \frac{1600\text{ e}^- \times 1.6 \cdot 10^{-19}\text{ C}}{3\text{ fF}} = 85\text{ mV} \quad (4.1)$$

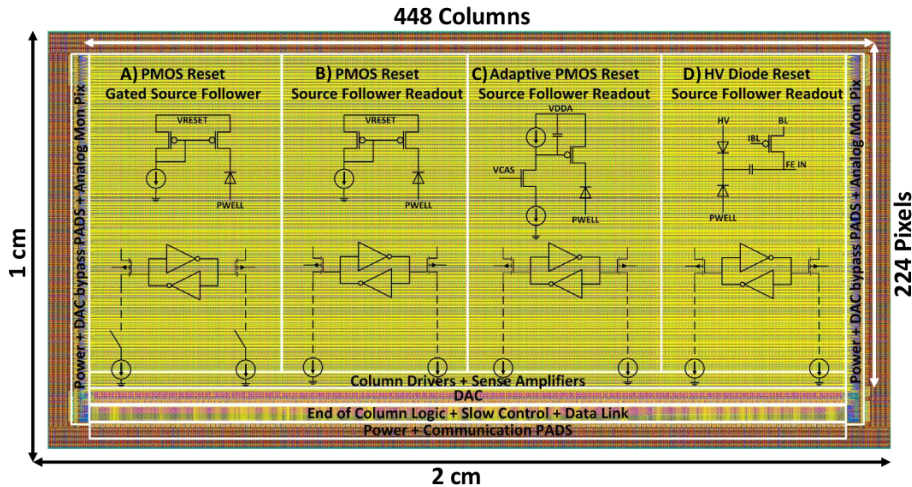
793 Secondly, a reset mechanism which slowly discharges the detector capacitance must be  
 794 included in the circuit:

$$V_{in} = \frac{Q_s}{C_{in}} e^{-t/R_b C_{in}} \quad (4.2)$$

795 where  $R_b$  is the equivalent reset element. The general constraint which must be satisfied  
 796 is that the discharge time  $\tau = R_b C_{in}$  must be slower than the characteristic time of  
 797 the amplifier, otherwise a signal loss could occurs. Traditionally the reset can be  
 798 implemented in two different way: with a forward biased diode, that might be implemented  
 799 by a simple p+ diffusion inside the well of the collection electrode n, or with a PMOS  
 800 transistor. Despite of the semplicity of the diode reset, since it is a non-linear element,  
 801 the discharge would depend on the quantity of charge Q generated on the n electrode,

802 prejudicing the linearity of the analog output (Q-ToT). To solve the issue, a PMOS reset  
 803 is the method preferred in design such TJ-Monopix1 with analog output; the PMOS  
 804 transistor, indeed, can acts as a constant current source and then used to discharge the  
 805 sensor. Although the PMOS reset is capable of providing a constant current, it has to be  
 806 manually re-tuned every time in order to restore the input DC baseline voltage; to do that  
 807 a low-frequency feedback is used.

808 The matrix is split in four sections, each one corresponding to a different flavor of the  
 809 FE, implemented in order to test more options.



808 Figure 4.4: TJ-Monopix1 has been developed in four different flavor. The flavor PMOS  
 809 reset (B) is considered as the reference one.

810 All the flavors implement a source-follower double-column bus readout: the standard  
 811 variation is the flavor B, that features a PMOS input reset (refered as "PMOS reset").  
 812 Flavor A is identical to flavor B except for the realization of the source follower (it is a  
 813 gated one): in the circuit of the gated versione there is a transistor more that operates on  
 814 the baseline and on the feedback mechanism; this aim to reduce the power consumption  
 815 and results in a higher signal baseline, and then in a lower effective threshold. C instead  
 816 implements a novel leakage compensation circuit, with a PMOS reset configuration. More-  
 817 over the collection electrode can be either DC-coupled to the readout electronics, as in  
 818 flavors A, B, C, or AC-coupled through a metal-oxide-metal (MOM) capacitor, as in D  
 819 is AC-coupled. The latter one allows applying a high bias voltage to the electrode n and  
 820 for this reason the flavor D is also called "HV flavor". Unfortunately the "HV" suffer  
 821 from a signal loss, which can achieve even the 50%, due to the additional parasitic capac-  
 822 ity introduced at the input node. The HV voltage above which the breakdown begins is  
 823  $\sim 50$  V; however at values bigger than 20 V, the gain does not increase anymore, since the  
 824 depletion zone is already fully depleted.

#### 825 4.2.1 ALPIDE-like

826 ALPIDE chips, developed by the ALICE collaboration, implemented a standard FE to the  
 827 point that many CMOS MAPS detectors used a similar FE and are called "ALIPDE-like".  
 828 Considering that both TJ-Monopix1 and ARCADIA-MD1 have an ALPIDE-like FE, I am  
 829 going to explain the broad principles of the early FE stage. The general idea is of the  
 830 amplification to transfer the charge from a bigger capacity[15],  $C_{source}$ , to a smaller one,

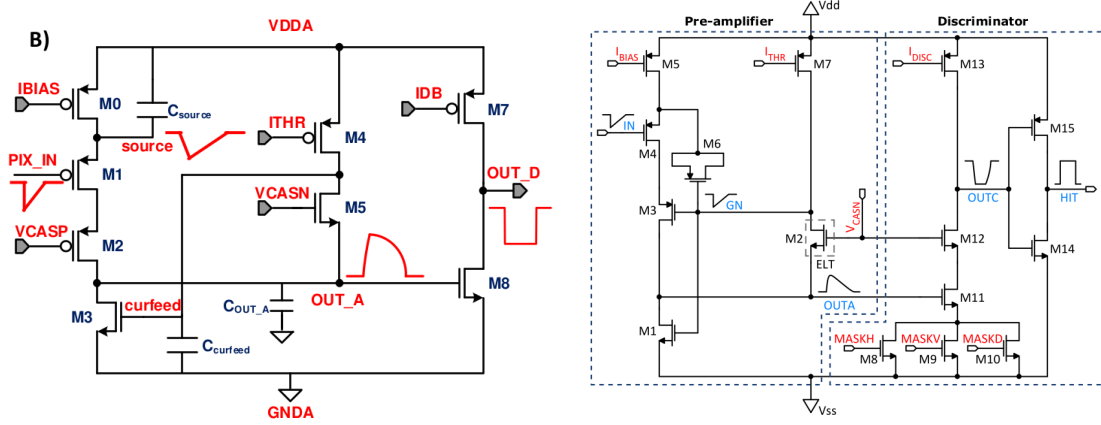


Figure 4.5

831  $C_{out}$ : the input transistor M1 with current source IBIAS acts as a source follower and this  
 832 forces the source of M1 to be equal to the gate input  $\Delta V_{PIX\_IN} = Q_{IN}/C_{IN}$ .

$$Q_{source} = C_{source} \Delta V_{PIX\_IN} \quad (4.3)$$

833 The current in M2 and the charge accumulates on  $C_{out}$  is fixed by the one on  $C_{source}$ :

$$\Delta V_{OUT\_A} = \frac{Q_{source}}{C_{OUT\_A}} = \frac{C_{source} \Delta V_{PIX\_IN}}{C_{OUT\_A}} = \frac{C_{Source}}{C_{OUT\_A}} \frac{Q_{IN}}{C_{IN}} \quad (4.4)$$

834 A second branch (M4, M5) is used to generate a low frequency feedback, where VCASN  
 835 and ITHR set the baseline value of the signal on  $C_{OUT\_A}$  and the velocity to goes down  
 836 to the baseline. **IL RUOLO DI CURVFEED NON L'HO CAPITO.** Finally IDB defines  
 837 the charge threshold with which the signal  $OUT\_A$  must be compared: depending on if  
 838 the signal is higher than the threshold or not, the  $OUT\_D$  is high or low respectively.

839 The actual circuit implemented in TJ-Monopix1 is shown in figure 4.5: the principal  
 840 difference lays in the addition of disableing pixels' readout. This possibility is uttermost  
 841 important in order to reduce the hit rate and to avoid saturating the bandwidth due to the  
 842 noisy pixels, which typically are those with manufacturing defects. In the circuit transis-  
 843 tors M8, M9 and M10 have the function of disabling registers with coordinates MASKH,  
 844 MASKV and MASKD (respectively vertical, orizontal and diagonal) from readout: if all  
 845 three transistors-signals are low, the pixel's discriminator is disabled. Compared with a  
 846 configurable masking register which would allow disableing pixels individually, to use a  
 847 triple redundancy reduces the sensistivity to SEU but also gives amount of intentionally  
 848 masked ("ghost") pixels. This approach is suitable only for extremely small number N of  
 849 pixel has to be masked: if two coordinate projection scheme had been implemented, the  
 850 number of ghost pixels would have scale with  $N^2$ , if instead three coordinates are used,  
 851 the N's exponential is lower than 2 (fig. 4.6)

852 Foto dell'oscilloscopio per far vedere cosa fanno i parametri

### 853 4.3 Readout logic

854 TJ-Monopix1 has a triggerless, fast and with ToT capability R/O which is based on a  
 855 column-drain architecture. On the pixel are located two Random Access Memory (RAM)  
 856 cells to store the 6-bit LE and 6-bit TE of the pulse, and a Read-Only Memory (ROM)

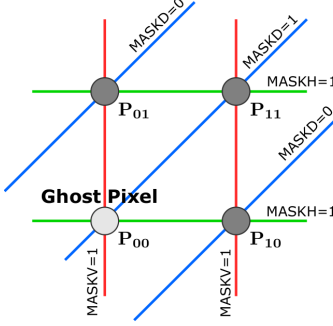


Figure 4.6

Parameter	Meaning	
IBIAS	mainly controls the rise time	yes
IDB	sets the discriminator threshold	yes
ITHR	sets the velocity of the return to the baseline	yes
ICASN	sets the baseline of the signal	yes
VRESET	sets the gain of the preamplifier	yes
IRESET	sets the gain of the preamplifier	no

Table 4.3: FE parameters which must be setted through the DAQ. "Function" means that higher parameter implies higher value

857 containing the 9-bit pixel address. Excluded these memories, TJ-Monopix1 hasn't any  
 858 other buffer: if a hit arrives while the pixel is already storing a previous one, the new  
 859 data get lost. After being read, the data packet is sent to the EoC periphery of the  
 860 matrix, where a serializer transfers it off-chip to an FPGA (4.7). There a FIFO is used  
 861 to temporarily stored the data, which is transmitted to a computer through an ethernet  
 862 cable in a later time.

863 The access to the pixels' memory and the transmission of the data to the EoC, following  
 864 a priority chain, is managed by control signals and is based on a Finite State Machine  
 865 (FSM) composed by four state: no-operation (NOP), freeze (FRZ), read (RD) and data  
 866 transfer (DTA). The readout sequence (??) starts with the TE of a pulse: the pixel  
 867 immediately tries to grab the column-bus turning up a hit flag signal called *token*. The  
 868 token is used to control the priority chain and propagates across the column indicating  
 869 what pixel that must be read. To start the readout and avoid that the arrival of new hits  
 870 disrupt the priority logic, a *freeze* signal is activated, and then a *read* signal controls the  
 871 readout and the access to memory. During the freeze, the state of the token for all pixels  
 872 on the matrix remains settled: this does not forbid new hits on other pixels from being  
 873 recorded, but forbids pixels hit from turning on the token until the freeze is ended. The  
 874 freeze stays on until the token covers the whole priority chain and gets the EoC: during  
 875 that time new token cannot be turned on, and all hits arrived during a freeze will turn  
 876 on their token at the end of the previous freeze. Since the start of the token is used to  
 877 assign a timestamp to the hit, the token time has a direct impact on the time resolution  
 878 measurement; this could be a problem coping with high hits rate.

879 The analog FE circuit and the pixel control logic are connected by an edge detector  
 880 which is used to determine the LE and the TE of the hit pulse(fig. 4.9): when the TE

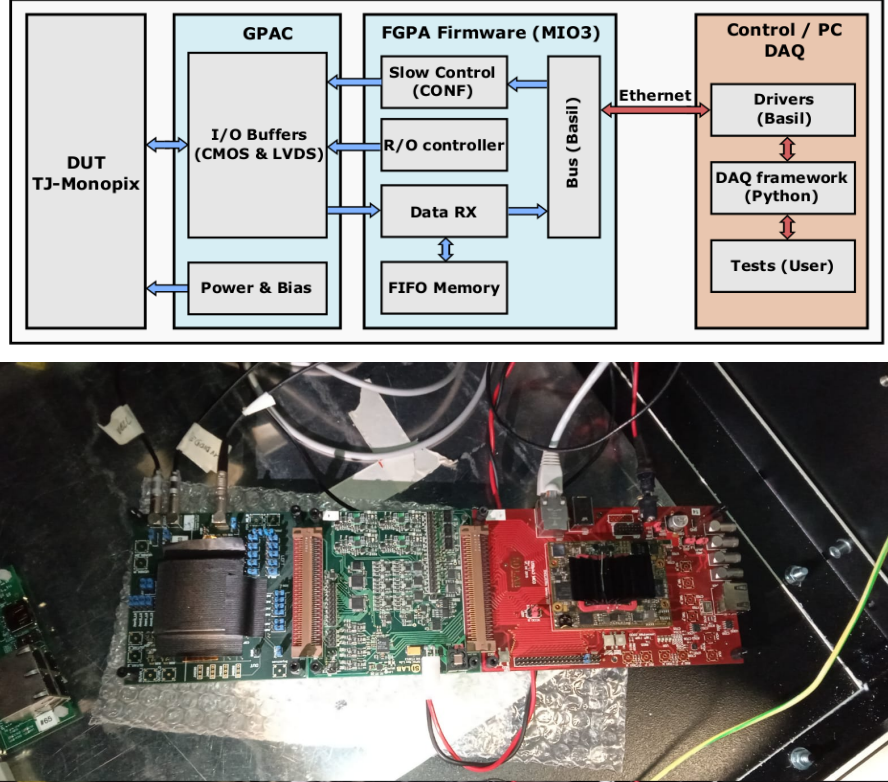
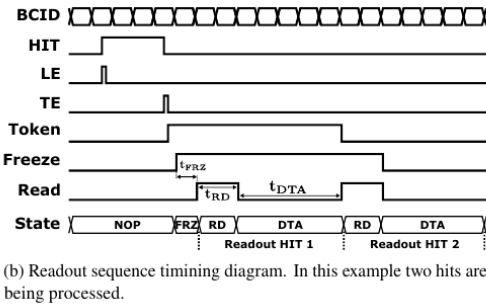


Figure 4.7: Main caption



(b) Readout sequence timing diagram. In this example two hits are being processed.

Figure 4.8: Readout timing diagram: in this example two hits are being processed

is stored in the first latch the edge detector is disabled and, if the **FREEZE** signal is not set yet, the readout starts. At this point the **HIT** flag is set in a second latch and a **Token** signal is produced and depending on the value of **Token** in the pixel can be read or must wait until the **Token in** is off. In figure an OR is used to manage the token propagation, but since a native OR logic port cannot be implemented with CMOS logic, a sum of a NOR and of an inverter is actually used; this construct significantly increases the propagation delay (the timing dispersion along a column of 0.1-0.2 ns) of the token and to speed up the circuit optimized solution are often implemented. When the pixel become the next to be read in the queue, and at the rising edge of the **READ** signal, the state of the pixel is stored in a D-latch and the pixel is allowed to use the data bus; the **TE** and the **HIT** flag latches are reset and a **READINT** signal that enable access of the RAM and ROM cells is produced.

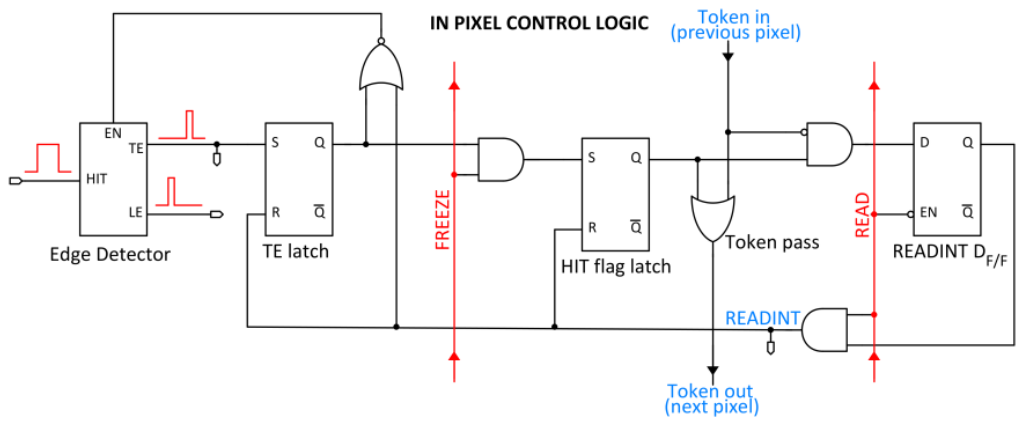


Figure 4.9

893        The final data must provide all the hits' information: the pixel address, the ToT and  
 894        the timestamp. All those parts are assigned and appended at different time during the  
 895        R/O chain:

- 896        • **Pixel address:** while the double column address (6-bit) is appended by the EoC  
 897        circuit, the row address (8-bits for each flavor) and the physical column in the doublet  
 898        (1-bit) are assigned by the in-pixel logic
- 899        • **ToT:** is obtained offline from the difference of 6-bits TE and 6-bits LE, stored by  
 900        the edge detector in-pixel; since a 40 MHz BCID is distributed across the matrix,  
 901        the ToT value is range 0-64 clock cycle which corresponds to 0-1.6  $\mu$ s
- 902        • **Timestamp:** The timestamp of the hit correspond to the time when the pixel set  
 903        up the token; it is assigned by the FPGA, that uses the LE, TE and a 640 MHz  
 904        clock to derive it. For all those hits which arrived while the matrix is frozen, the  
 905        timestamp is no more correlated with the time of arrival of the particle

906        When the bits are joined up together the complete hit data packet is 27-bit.

907 **Chapter 5**

908 **Arcadia-MD1**

909 [16] [17]

910 Breve introduzione analoga a Monopix1 in cui descrivo brevemente la "timeline" da  
911 SEED Matisse a Md1 e Md2

912 **5.1 The sensor**

913 ARCADIA-MD1 is an LFoundry chip which implements the technology 110 nm CMOS  
914 node with six metal layer ???. The standard p-type substrate was replaced with an n-type  
915 floating zone material, that is a technique to produce purified silicon crystal. (pag 299  
916 K.W.).

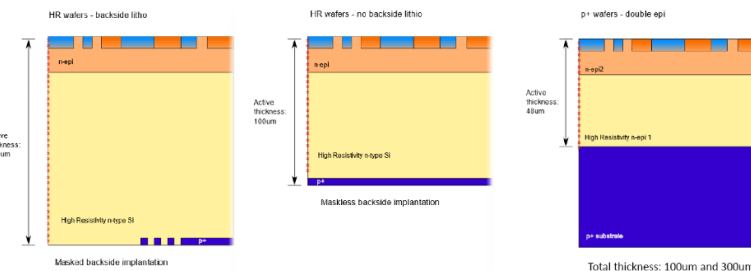


Figure 5.1

917  
918 Wafer thinning and backside lithography were necessary to introduce a junction at the  
919 bottom surface, used to bias the substrate to full depletion while maintaining a low voltage  
920 at the front side.

921 C'è un deep pwell per - priority chainseparare l'elettronica dal sensore; per controllare il  
922 punchthrough è stato aggiunto un n doped epitaxial layer having a resistivity lower than  
923 the substrate.

924 It is part of the category of DMAPS Small electrode to enhance the signal to noise  
925 ratio.

926 It is operated in full depletion with fast charge collection by drift.

927 Prima SEED si occupa di studiare le prestazioni: concept study with small-scale test  
928 structure (SEED), dopo arcadia: technology demonstration with large area sensors Small  
929 scale demo SEED(sensor with embedded electronic development) Quanto spazio dato

930 all'elettronica sopra il pwell e quanto al diodo. ..

## 931 5.2 Readout logic and data structure

### 932 5.2.1 Matrix division and data-packets

933 The matrix is divided into an internal physical and logical hierarchy: The 512 columns are  
 934 divided in 16 section: each section has different voltage-bias + serializzatori. Each section  
 935 is devided in cores () in modo che in ogni doppia colonna ci siano 1Pacchetto dei dati 6  
 936 cores. ricordati dei serializzatori: sono 16 ma possono essere ridotti ad uno in modalità  
 spazio

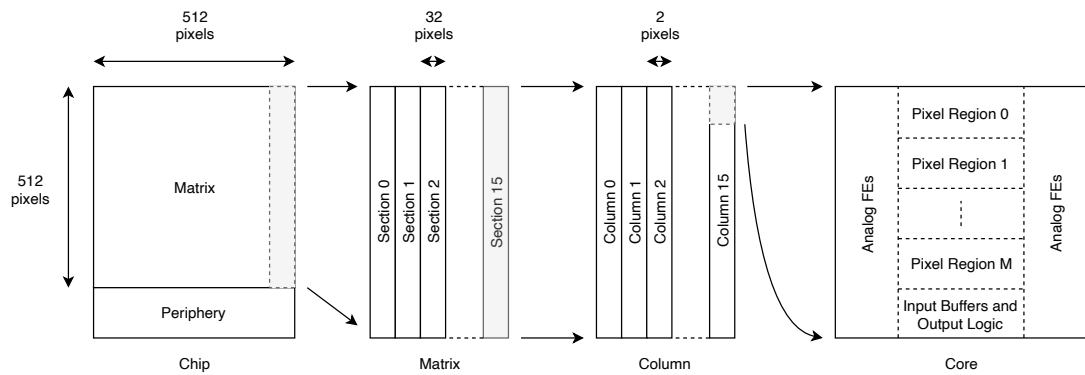


Figure 5.2

937

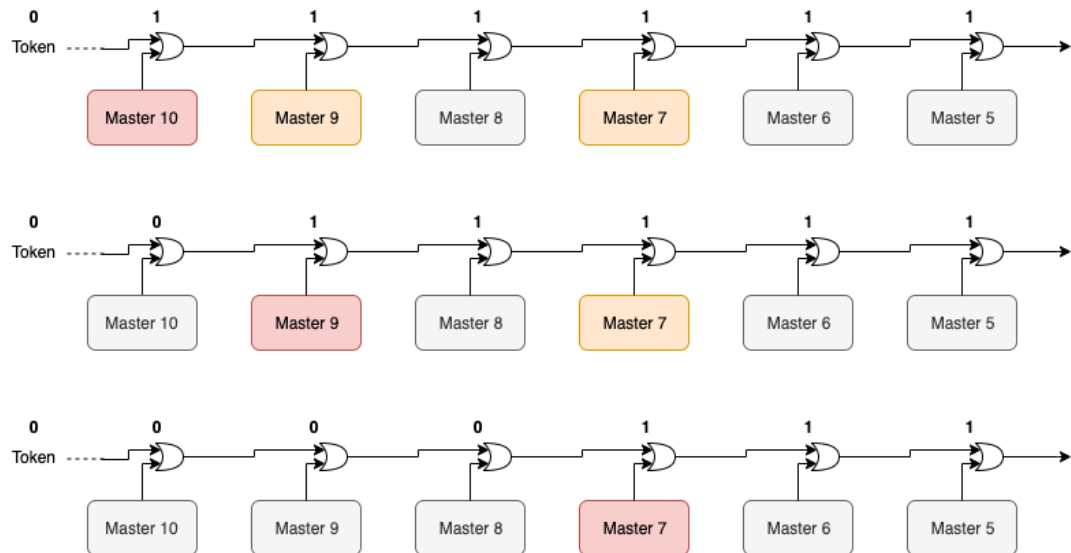


Figure 5.3

938 Questa divisione si rispecchia in come sono fatti i dati: scrivi da quanti bit un dato è  
 939 fatto e le varie coordinate che ci si trovano dentro; devi dire che c'è un pixel hot e spieghi  
 940 dopo a cosa serve, e devi accennare al timestamp

941 "A core is simply the smallest stepped and repeated instance of digital circuitry. A  
 942 relatively large core allows one to take full advantage of digital synthesis tools to imple-  
 943 ment complex functionality in the pixel matrix, sharing resources among many pixels as

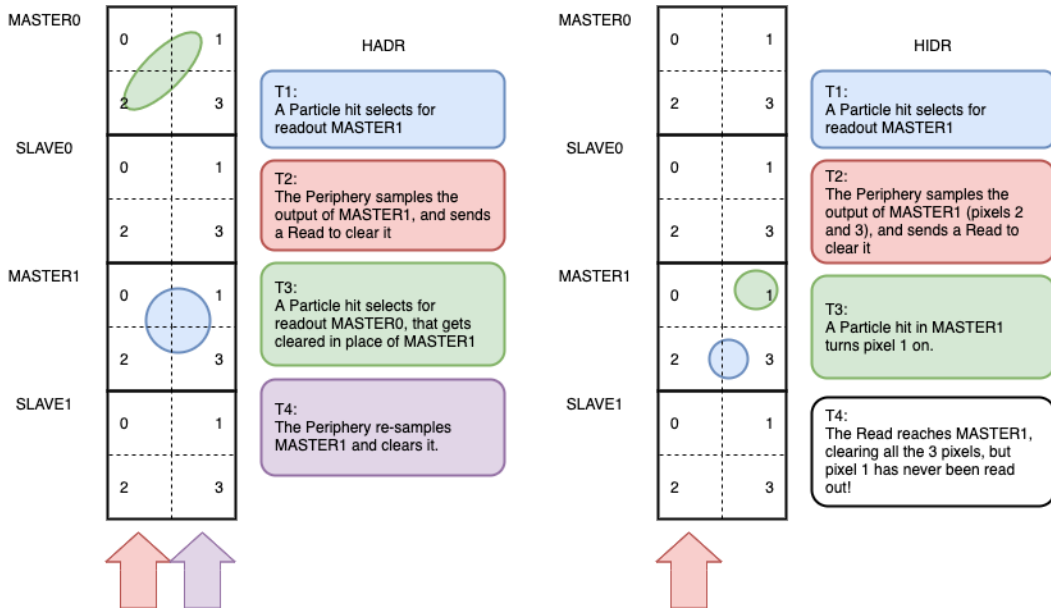


Figure 5.4

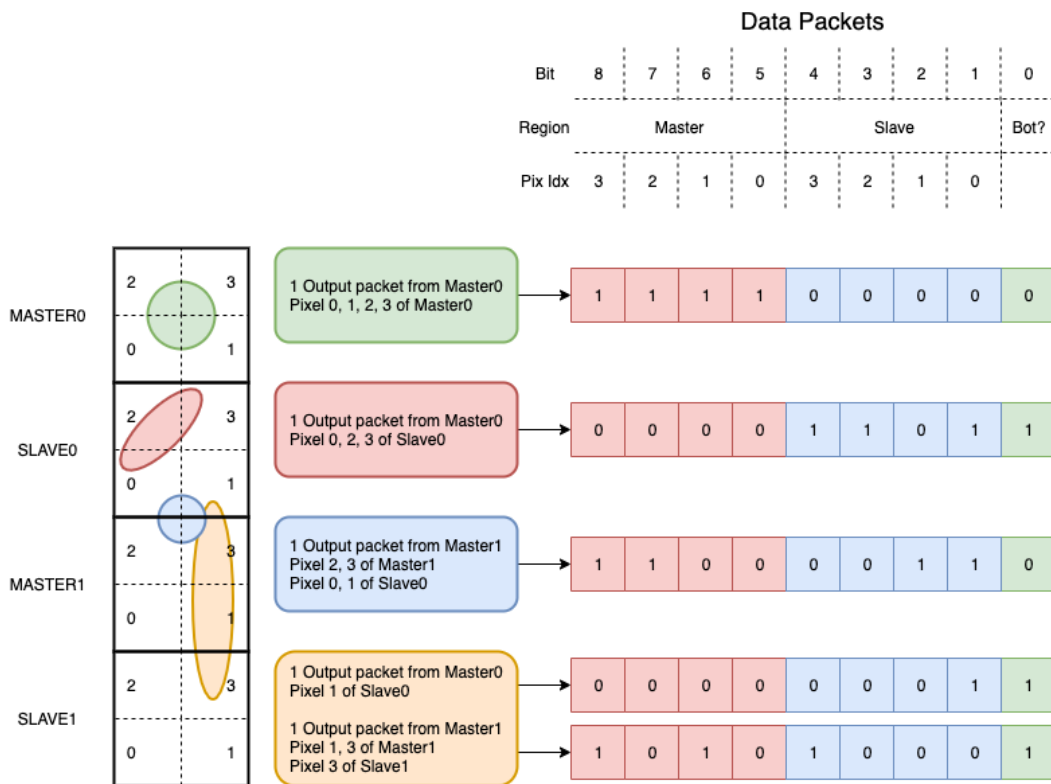


Figure 5.5

needed.”. pagina 28 della review.

945

946 TABELLA: con la gerarchia del chip Matrix (512x512 pixels) Section (512x32 pixels)  
947 Column (512x2) Core (32x2) Region (4x2)

948

Nel chip trovi diverse padframe: cosa c’è nelle padframe e End of section.

949

”DC-balance avoids low frequencies by guaranteeing at least one transition every n

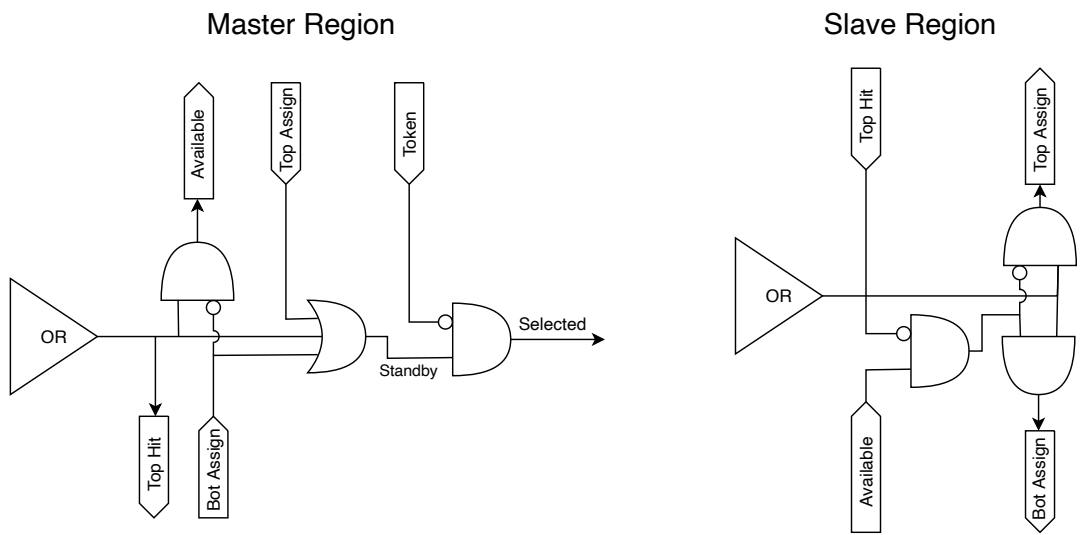


Figure 5.6

950 bits; for example 8b10b encoding  $n = 5$ "

951    **Chapter 6**

952    **Characterization**

953

- 954    • rifai il conto della lunghezza di attenuazione. Ho trovato (presentazione Luciano  
955    Mus) 29 um per ka e 37 um per kb.
- 956    • Con il PMOS la configurazione del FE di default è: e richiama i significati delle  
957    variabili.
- 958    • soglia dell'automasking a 10 Hz.
- 959    • parla dell HV

960    **6.1 TJ-Monopix1 characterization**

961    **6.1.1 Threshold and noise: figure of merit for pixel detectors**

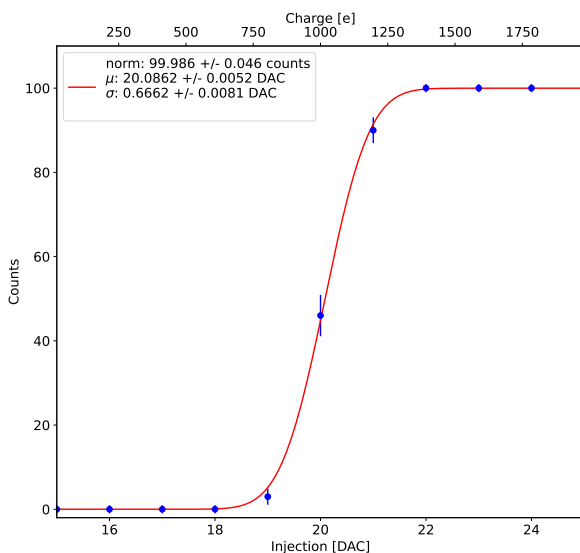


Figure 6.1: S-curve for pixel (10, 10) of the PMOS flavor (flavor 1) with IDB fixed at 40 DAC. The conversion of charge injected from DAC to electrons has been done assuming a conversion factor of 20 e-/DAC.

962 A characterization of threshold and noise is typically necessary since these values have  
 963 an impact on the operating conditions and on the performance of the chips, so much that  
 964 the signal to threshold ratio may be considered as the figure of merit for pixel detectors  
 965 rather than the signal to noise ratio. The mean minimum stable threshold evolved through  
 966 different generation of chips: in the 1st generation it was around  $2500\text{ e-}$  while in the 3rd  
 967 (corresponding to nowadays chips) is less than  $500\text{ e-}$ . This allows in thinner sensors with  
 968 smaller signals: from  $16\,000\text{ e-}$  produced in  $200\text{ }\mu\text{m}$ , the signal expected moved down to  
 969  $2000\text{ e-}$  produced in  $25\text{ }\mu\text{m}$ . According with this, the threshold of TJ-Monopix1 is around  
 970  $500\text{ e-}$ .

971 Obviously the threshold has to be located between the noise peak around the baseline  
 972 and the signal distribution, in particular it has to be low enough to mantain a high signal  
 973 efficiency, but also high enough to cut the noise: for a low threshold many pixels can fire  
 974 at the same time and a positive feedback can set off a chain reaction eventually, causing  
 975 all the other pixels to fire. Thus, the noise sets a lower bound to the threshold: if an  
 976 occupancy  $\leqslant 10^{-4}$  is required, for example, this correspond to the Gaussian 1-sided tail  
 977 fraction for  $3.7\sigma$ . In this case, if the noise is  $100\text{ e-}$  (resonable), the threshold must be  
 978 higher than  $3.7 \times 100\text{ e-}$ . Typically this argument sets only a minimal bound to the  
 979 threshold since the variation with time and from pixel to pixel have to be taken into  
 980 account: the temperature, the annealing (for example, the radiation damages in the oxide  
 981 layer causes shift of MOSFET threshold voltage) and the process parameters variation  
 982 across the wafer (as for example process mismatch between transistors).

983 Given that the first stage of amplification is the most crucial, since in the following  
 984 stages the signal amplitude is high compared to additional noise, the noise is valued at  
 985 the preamplifier input node. Then, the noise is parameterized as Equivalent Noise Charge  
 986 (ENC), which is defined as the ratio between the noise N at the output expressed in Volt  
 987 and the out voltage signal S produced by  $1\text{ e-}$  entering in the preamplifier:

$$ENC = \frac{N_{out}[V]}{S_{out}[V/e-]} = \frac{V_{noise}^{RMS}}{G} \quad (6.1)$$

988 with G expressed in  $\text{V/e-}$ ; as the gain increases, the noise reduces . **Servirebbe una misura**  
 989 Considering the threshold dispersion a requirement for the ENC is:

$$ENC < \sqrt{(T/3.7)^2 - T_{RMS}^2(x) - T_{RMS}^2(t)} \quad (6.2)$$

990 where the T is the threshold setted,  $T_{RMS}$  is the threshold variation during time (t) and  
 991 across the matrix (x); a typical reasonable value often chosen is 5 ENC.

992 Because of the changing of the 'real' threshold, the possibility of changing and adapting  
 993 the setting parameters of the FE, both in time and in space is desiderable: these parameters  
 994 are usually set by Digital to Analog Converter (DAC) with a number of bit in a typical  
 995 range of 3-7. Unfortunately DAC elements require a lot of space that may be not enough  
 996 on the pixel area; therefore, the FE parameters are typically global, which means that they  
 997 are assigned for the whole chip, or they can be assigned for regions the matrix is divided  
 998 into. The former case corresponds to TJ-Monopix1's design in which 7 bits are used for  
 999 a total 127-DAC possible values, while the latter corresponds to the ARCADIA-MD1's  
 1000 one, **where quanti bit??**. An other possibility, for example implemented in TJ-Monopix2,  
 1001 is allocate the space on each pixel for a subset of bits, then combinig the global threshold  
 1002 with a fine tuning. If so, the threshold dispersion after tuning is expected to be inversely

	DAC units	electrons
Threshold	$24.529 \pm 0.049$	$511.0 \pm 1.0$
Threshold dispersion	$1.848 \pm 0.033$	$36.96 \pm 0.66$
Noise	$0.8222 \pm 0.0043$	$16.444 \pm 0.086$
Noise dispersion	$0.0975 \pm 0.0030$	$1.95 \pm 0.06$

Table 6.1: Flavor PMOS, IDB fixed at 40 DAC

1003 proportional to the tuning DAC number of bits and thus be improved a lot:

$$\sigma_{THR,tuned} = \frac{\sigma_{THR}}{2^{nbit}} \quad (6.3)$$

1004 where  $\sigma_{thr}$  is the RMS of the threshold spread before tuning.

1005 To measure the threshold and noise of pixels a possible way is to make a scan with  
 1006 different known injected charge: the threshold corresponds to the value where the efficiency  
 1007 of the signal exceeds the 50%, and the ENC is determined from the width of this edge.  
 1008 Following this path, I have used the injection circuit available on the chip to inject 100  
 1009 pulses for each input charge for a fixed threshold. The injection comes on a capacity at the  
 1010 input of the FE circuit, whose mean value is 230 aF and from which the conversion factor  
 1011 from DAC units to electrons can be obtained: for the PMOS flavor, for example, since  
 1012 the DAC are biased at 1.8 V, the Least significant Bit (LSB) corresponds to a voltage of  
 1013 14.7 mV from which the charge for LSB  $1.43 \text{ e-}/\text{mV}$  and the conversion factor therefore  
 1014 is  $20.3 \text{ e-}/\text{DAC}$ . While this value is equivalent for all the PMOS flavor, the HV flavor  
 1015 is expected to have a different conversion factor,  $\sim 33 \text{ e-}/\text{DAC}$ , because of the different  
 1016 input capacity.

1017 Besides the charge, also the duration and the period of the injection pulse can be set;  
 1018 it is important to make the duration short enough to have the falling edge during the dead  
 1019 time of the pixel (in particular during the FREEZE signal) in order to avoid the undershoot,  
 1020 coming at high input charge, triggering the readout and reading spurious hits. Since the injection circuit is coupled in AC to the FE, if the falling edge of the pulse  
 1021 is sharp enough to produce an undershoot, this can be seen as a signal.

1023 Assuming a gaussian noise, the efficiency of detecting the signal can be described  
 1024 through a modification of the error function:

$$f(x, \mu, \sigma) = \frac{1}{2} \left( 1 + erf \left( \frac{x - \mu}{\sigma\sqrt{2}} \right) \right) \quad (6.4)$$

1025 with: where the threshold and the ENC corresponds to the  $\mu$  and  $\sigma$ . Therefore I perform  
 1026 a fit of the counts detected using the function in equation 6.4. In figure 6.1 there is an  
 1027 example with IDB equal to 40 DAC of fit for a pixel belonging to the flavor B, while in  
 1028 table 6.1 and figure ?? there are the histograms and the maps of the parameters of the  
 1029 scurve-fit. As expected, the flavor PMOS reset gated (A), thanks to the transistor which  
 1030 change the baseline value, has a lower threshold and noise

1031 Small threshold variations have been observed in the first biasing section (columns from  
 1032 0 to 14) with IDB=40 DAC; the same structure appears more evident both at other IDBs  
 1033 and in the slope and offset distribution at IDB=40 DAC I will talk about in the next  
 1034 section. **metti un plot con IDB 90/100 DAC** The systematic threshold variation across  
 1035 the biasing group can be due, for example, to the transistor mismatch of the biasing DAC

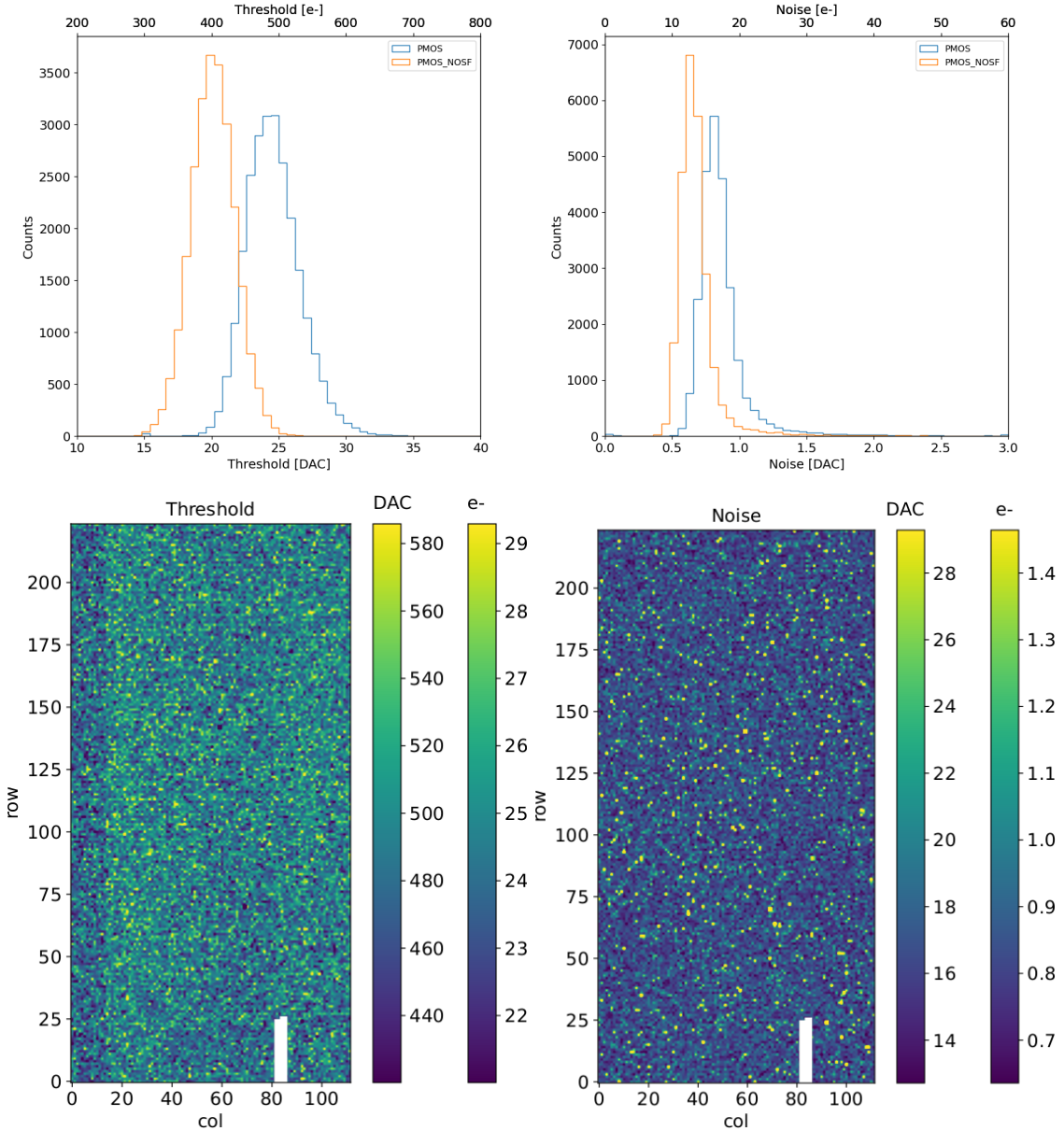


Figure 6.2: Histograms of the threshold (a) and the noise (b) found fitting the s-curve of all flavor with IDB fixed at 40 DAC. Below there are the maps of the threshold (a) and the noise (b), respectively, found fitting the s-curve with IDB fixed at 40 DAC for the PMOS flavor (B). The white pixels have the injection circuit broken.

register IDB or to the value of the baseline (setted by ICASN). A solution, implemented in TJ-Monopix2, has been to include more columns in each biasing group increasing the effective transistor area.

1039

To verified the trend of the threshold as a function of the front end parameter IDB and find its dynamic range, I have permormed different scans changing the IDB: I have injected the whole matrix and found the means and the standard deviation of the distributions. The results are shown in figure 6.3: the blue points are the mean threhsold found whithin the matrix, while in green is shown the width of the threshold distribution, aka the threshold dispersion. While the threshold increases, the ENC decreases of  $\sim 4 \text{ e-}$ , which is  $\sim 1/3$  of

the noise at IDB=40 DAC.

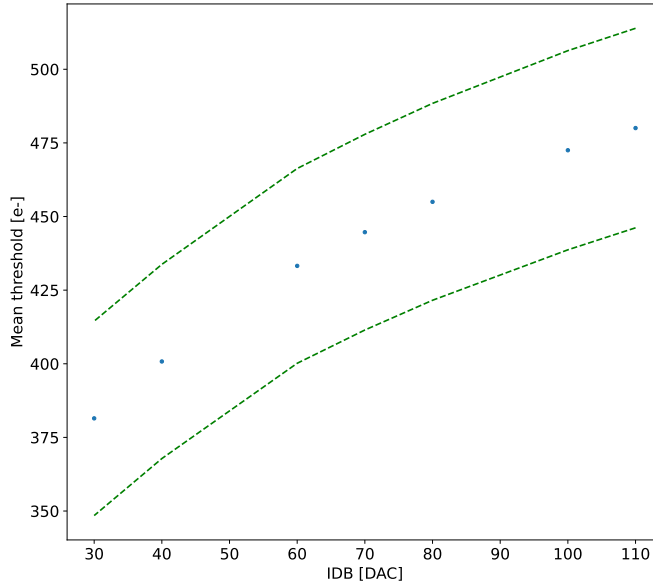


Figure 6.3: Flavor PMOS (B) with Psub-Pwell biased at -6 V. Threshold measured in electrons vs the register which sets the threshold, IDB.

1046

### 1047 6.1.2 Linearity of the ToT

1048 I have already said in chapter 4 that TJ-Monopix1 returns an output signal proportional to  
 1049 the charge released by a particle in the epitaxial layer, which is the Time over Threshold;  
 1050 the ToT is saved as a 6-bit variable and then has a dynamic range equal to 0-64, which  
 1051 corresponds to 0  $\mu$ s to 1.6  $\mu$ s assuming a clock frequency of 40 MHz. When a pulse is longer  
 1052 than 1.6  $\mu$ s the counter rolls back to zero and there is no way to distinguish that charge  
 1053 from a lower one with the same ToT: that is the rollover of the ToT (??(a)).

1054 In order to associate the ToT (in range 0-64) to the charge, a calibration of the signal  
 1055 is necessary. Assuming the linearity between ToT and the charge, Q can be found:

$$Q [DAC] = \frac{(ToT [au] - q [au])}{m [au/DAC]} \quad (6.5)$$

1056 where m and q are the fitted parameters of the calibration. It is important to keep in mind  
 1057 that the main application target of TJ-Monopix1 is in the inner tracker detector of HEP  
 1058 experiments, then the main feature is the efficiency, then a rough calibration of the signal  
 1059 to charge is fine. The ToT information can be used both to better reconstruct the charge  
 1060 deposition in cluster in order to improve the track resolution, and for particle identification,  
 1061 especially for low momentum particles which do not reach the proper detectors.

1062 The study of the output signal is made possibile via the injection: since the pulses are  
 1063 triangular, the ToT is expected to be almost linear depending on the injection charge value.  
 1064 To verify this statement and study the deviations from linearity I've fit the ToT versus the  
 1065 charge injected for all pixel within the matrix. In figure ??(b) there is an example of fit

	PMOS 0	PMOS 1	PMOS 2	HV
Slope [au/DAC]	$0.75566 \pm 0.00149$	$0.57145 \pm 0.00025$		
Slope dispersion [au/DAC]	$0.03841 \pm 0.00037$	$0.01685 \pm 0.00016$		
Intercept [au]	$-11.6070 \pm 0.0089$	$-10.824 \pm 0.019$		
Intercept dispersion [au]	$1.5176 \pm 0.0063$	$1.225 \pm 0.013$		

Table 6.2: Mean calibration parameters for all flavor and their dispersion on the matrix.

for a pixel belonging to the flavor B, while in figure 6.5 there are the histograms and the maps of the parameters of the line-fit for all flavors with IDB fixed at 40 DAC. Here again a difference between biasing section appears: since the slope of the ToT is related with the gain of the preamplifier (increasing the gain also increases the ToT), the mismatch is probably due to the transistor contributing to the amplification stage.

Before performing the fit I have calculated the mean value of the ToT of the pulses recorded for each pulse amplitude and I used the mean ToT as value for the fit. The aim of the calibration obviously is finding a relation only in the range 0-64 without taking into account the rolling over hits: therefore, to prevent the rollover data from reducing the mean ToT introducing a bias in the mean value, I cut and I did not consider them. If a signal bigger than the  $1.6 \mu\text{s}$  is expected in the usage of the detector, the threshold must be raised or the gain reduced, making the expected output signal in range 0-64. In figure ?? (b) are shown both the fits with a line (red) and with a second order polynomial (green): at the bounds of the ToT range values deviate from the line model. Since the deviation is low than 1% and it only interest the region near the 0 and the 64, in first approximation it is negligible.

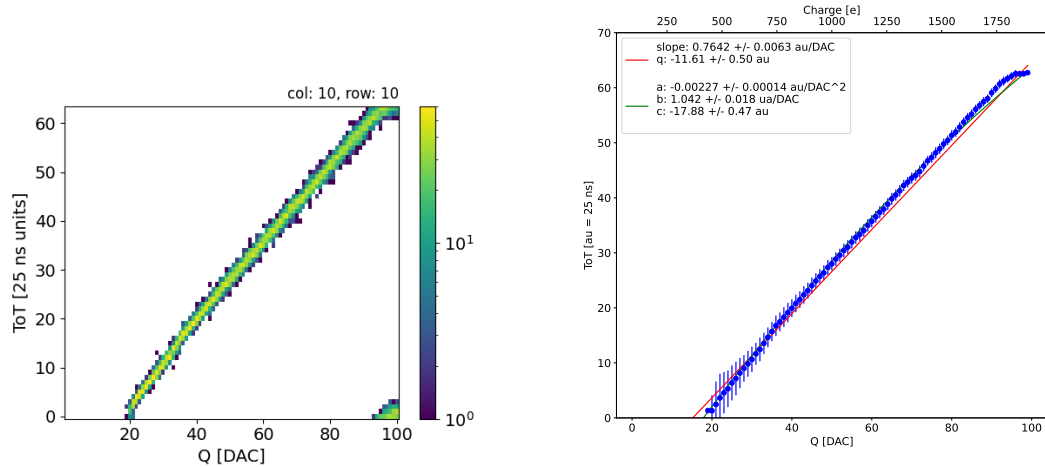


Figure 6.4: The figures refer to pixel (10,10) of the PMOS-reset flavor (1) with IDB fixed at 40 DAC for the PMOS flavor (B). (a) Histogram of the injection pulses: the ToT is in range 0-64 since it is represented by 6 bit, so when achieving the 64 it rolls over back to the zero. (b) Mean ToT vs the the charge: the mean has been calculated cutted the rolling hits.

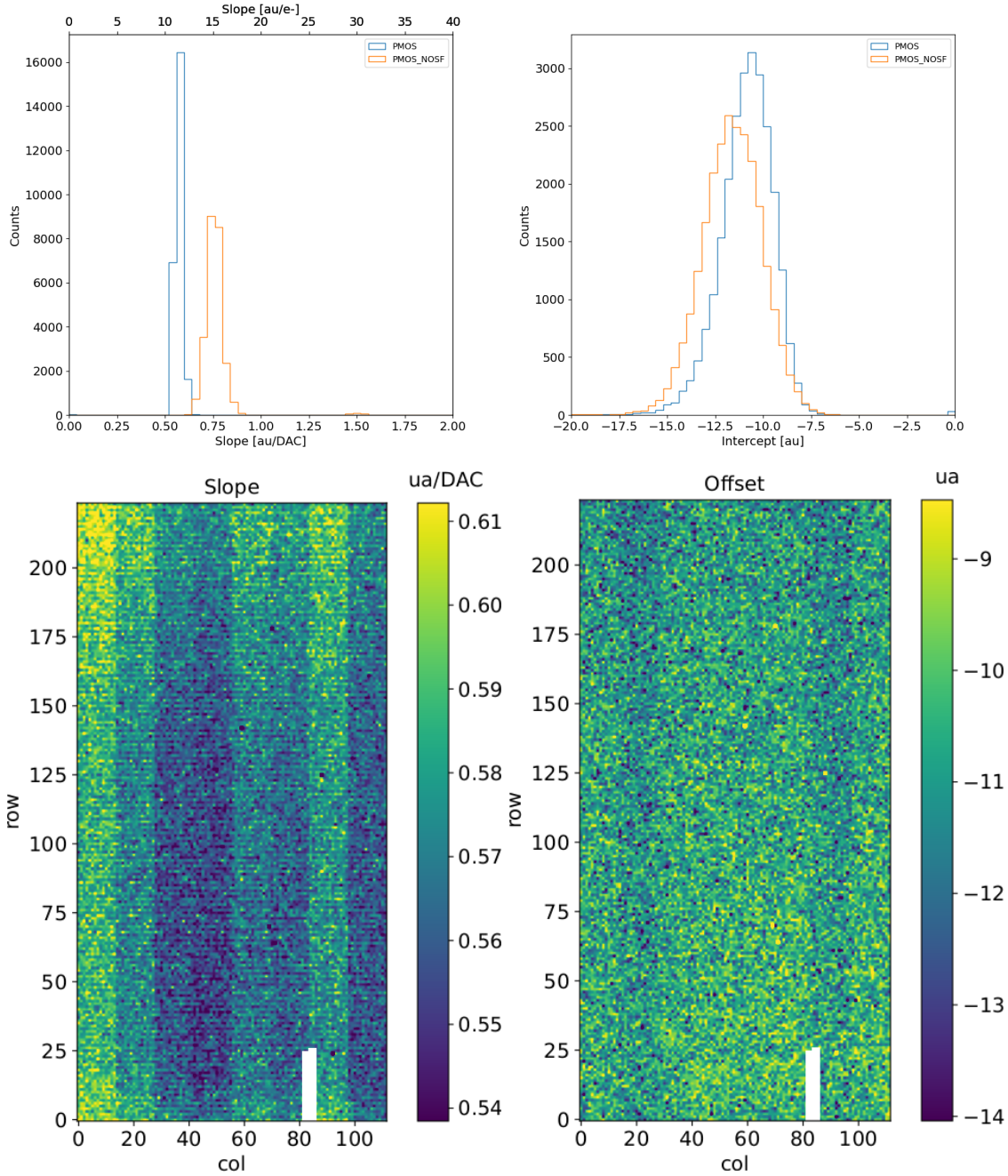


Figure 6.5: Histograms of the calibration parameters, slope (a) and offset (b), found fitting the ToT with a line, for all flavor and with IDB fixed at 40 DAC. Maps of the calibration parameters, slope (a) and offset (b), found fitting the ToT with a line, with IDB fixed at 40 DAC

### 6.1.3 Calibration of the ToT

Considering that the charge injected in the FE goes to fill capacitor which is different from pixel to pixel, the true charge injected does not correspond to what expected assuming C equal to 230 aF, the nominal value. Accordingly to that, a verification of the value provided and an absolute calibration of this capacity and of the conversion factor F is needed to have a correspondence of the signal in electrons; assuming C 230 aF, F is expected to be

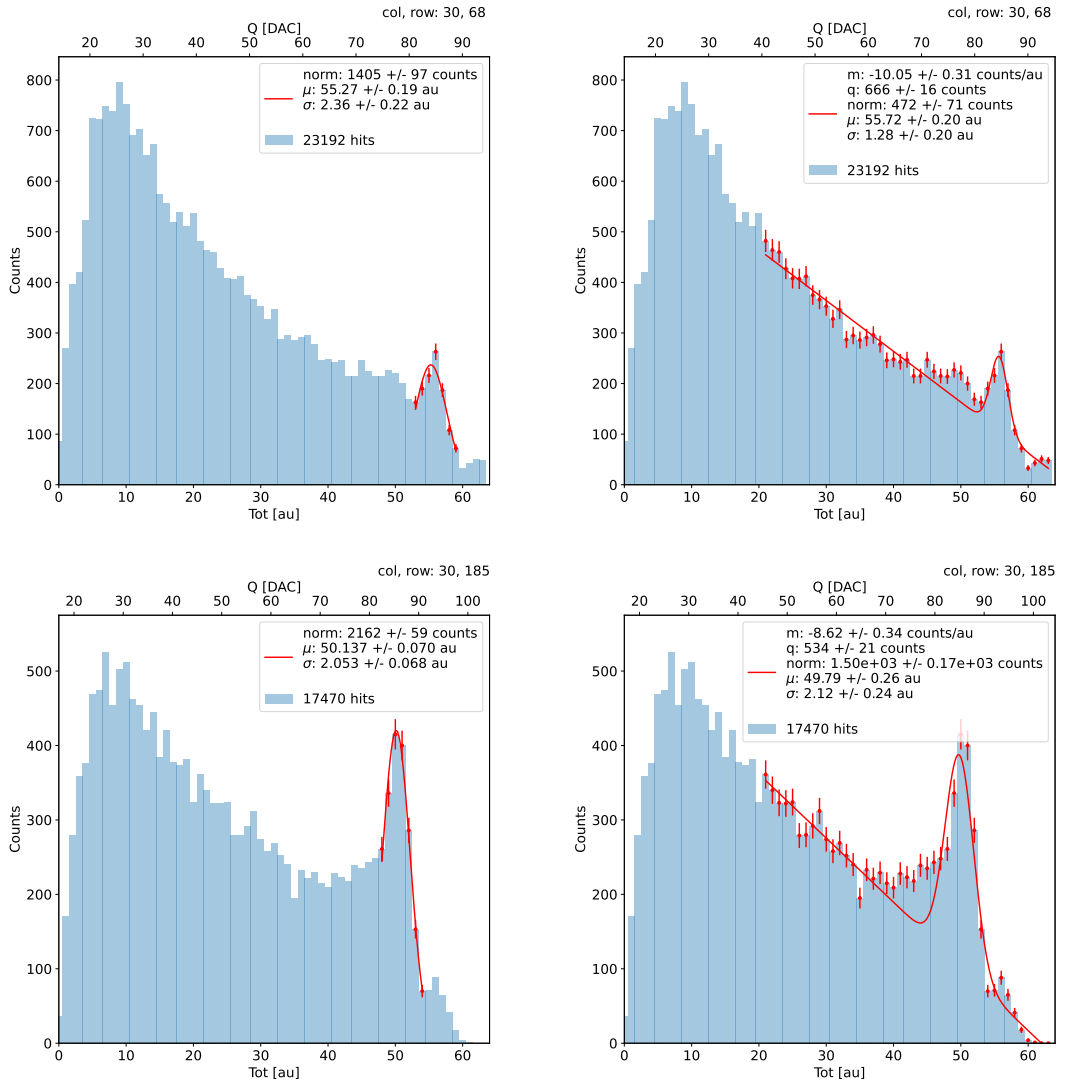


Figure 6.6: due pixel per far vedere la differenza tra i fit. Sottolinea che in rosso ci sono i bin fittati. La doppia scala utilizza le info trovate nel paragrafo precedente per il dato pixel in questione. Per avere una corrispondenza grezza in elettroni basta moltiplicare per 20 e- / dac.

1088 20 e-/DAC, and is defined as:

$$F[e- / DAC] = \frac{1616 e-}{Q [DAC]} \quad (6.6)$$

1089 For this purpose a Fe55 radioactive source has been employed; the Fe55 is an extremely  
 1090 important radionuclide in the calibration of X-ray spectrometers, proportional counter  
 1091 and scintillator detector since it emits two X-photons during the electron capture  
 1092 decay: the first one ( $K_\alpha$ ) at 5.9 keV and the second one ( $K_\beta$ ) at 6.5 keV. The  $K_\alpha$  photon,  
 1093 which does photoelectric effect in the silicon, has an absorption length  $\lambda=7 \mu\text{m}$  to  $8 \mu\text{m}$ ,  
 1094 and the probability of being absorbed in the  $25 \mu\text{m}$  thick epitaxial layer is  $\sim 0.95$ . The  
 1095 electron emitted has an energy equal to the photon one, so recalling that the mean energy  
 1096 needed to produce a couple electron-vacuum is 3.65 eV, the signal produced by the Fe55  
 1097 source is expected to be 1616 e-. In figures ?? and ?? are shown two histograms of the

1098 ToT spectrum of the Fe55 source for two different pixels. The peak corresponds to the  
 1099 events with completely absorption of the charge produced in the depleted region, while  
 1100 the long tail on the left to all the events with partial absorption due to charge sharing  
 1101 among neighbors pixels. In order to reduce the charge sharing, the pixel dimension in  
 1102 TJ-Monopix2 has been reduced down to  $30 \times 30 \mu\text{m}^2$ . The events on the right side of the  
 1103 peak, instead, corresponds to the  $K_\beta$  photons. Looking at the histograms for pixel (30,  
 1104 185) and (30,69) a significant difference in the peak to tail ratio leaps out. This difference  
 1105 in the efficiency of detecting the signal can be related with the position of the pixel in  
 1106 the matrix: in particular pixels in the upper part of the matrix (rows 112-224) have a  
 1107 more prominent peak, while in pixels in the lower part (rows 0-111) there is a higher  
 1108 partial absorption. I recall now that there is a slightly difference in the structure of the  
 1109 low dose-epi layer (??) among the rows in the matrix, in particular pixels in rows 112-224  
 1110 are supposed to have a higher efficiency in the pixel corner.

1111 For the calibration I have need to establish the peak position; to do that I perform a  
 1112 fit of the ToT histogram of each pixels. As fit functions I test both the solutions below:

$$f(x, N, \mu, \sigma) = \frac{N}{\sigma\sqrt{2\pi}} e^{-\frac{1}{2}\left(\frac{(x-\mu)}{\sigma}\right)^2} \quad (6.7)$$

$$f(x, m, q, N, \mu, \sigma) = m x + q + \frac{N}{\sigma\sqrt{2\pi}} e^{-\frac{1}{2}\left(\frac{(x-\mu)}{\sigma}\right)^2} \quad (6.8)$$

Nel primo caso ho fissato pochi pixel attorno a picco: il range è stato determinato ..

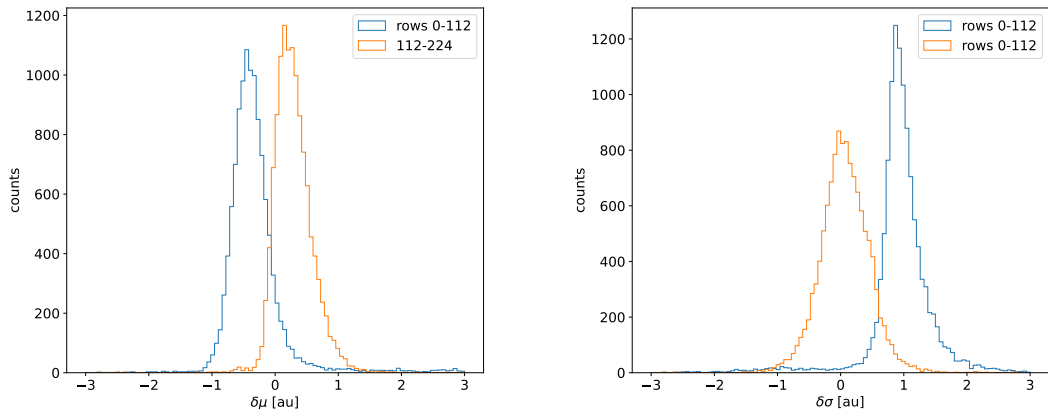


Figure 6.7: Here there are shown the defference between the parameters  $\mu$  and  $\sigma$  fitted with only a gaussian and with a gaussia plus a line. When  $\mu < 0$  the fit function 6.7 has given a worst peak (shifted on the left); when  $\sigma < 0$ , 6.8 has given a worst peak width (larger sigma)

1113  
 1114 **controlla. Nel secondo caso invece il range è.. Controlla sullo script** Even if the difference  
 1115 in the peak position between the two cases is not really relevant (6.7) being of the order  
 1116 of 0.8-1.5 %, it still introduces a systematic effect moving the peak on the left beacuse of  
 1117 the contribution of the tail. Indeed, we know that the sharp edge on the right corresponds  
 1118 to the complete absorption of the photon, so excluding the little bump on the right, the  
 1119 more the fitted parameter is on the right, the better the fit is. Moreover, there is also  
 1120 systematic effect on the peak width, infact the worst fit also gives an overestimation of

1121 the peak width. Even looking at the  $\chi^2$ , the fit function 6.7 seems so be the better choise,  
1122 except for a sample of pixels on the lower part of the matrix, the one with lower efficiency.

1123 Mappa del ferro da cui, come descritto enll'equazione si ricava la capacity. La struttura  
1124 a bande della capacità ha origine nel plot... e quindi nella calibrazione. Andando a vedere  
1125 gli istogrammi di queste due variabili si vedono dei picchi. C'è qualche struttura nella  
1126 matrice che condiziona il funzionamento delle righe? Larghezza della gaussiana: fai il  
1127 discorso a cosa contribuisce ad un picco così largo. è compatibile con quanto ti aspetti?  
1128 The voltage fluctuation around the peak is caused by the number fluctuation of generated  
1129 carriers (Fano noise) and the noise introduced by the detector (sensor and front-end pre-  
1130 amplifier).The ENC can be estimated from the standard deviation of the Kalpha voltage  
1131 distribution.  $ENC = \text{sqrt}(\sigma_{\text{misurata}} - \sigma_{\text{aspettata}})$  quella che ti aspetti dal fattore di Fano). E  
1132 è compatibile con quanto trovato? se non fosse compatibile rimaneggia questa frase:  
is added from the system (test setup) at the analog monitoring pixel output.

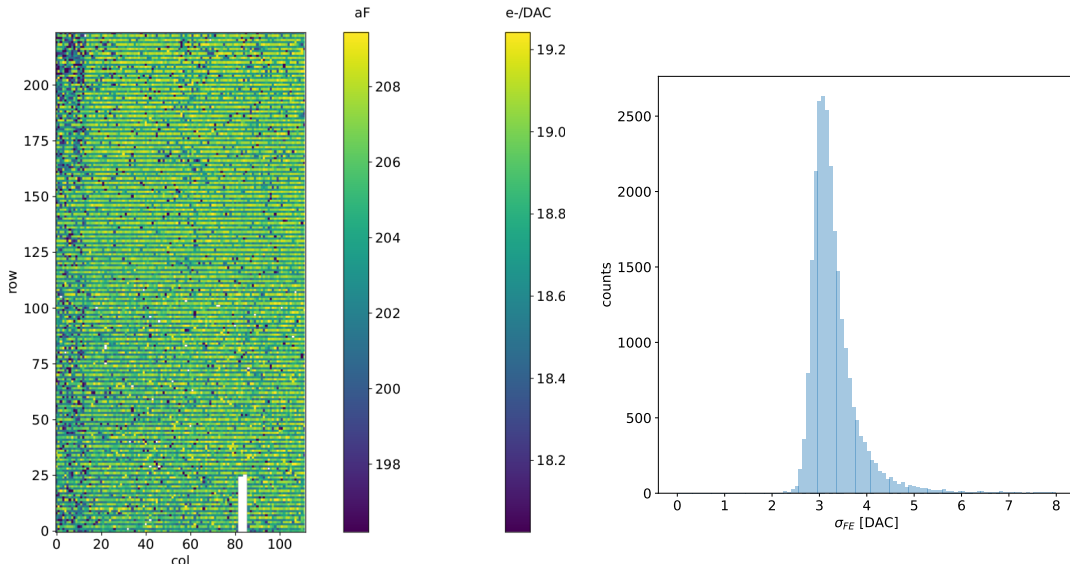


Figure 6.8

1133

#### 1134 6.1.4 Changing the bias

1135 In order to study the behavior of the sensor changing the bias, I perform some injection  
1136 scans in different configurations. The thickness of the depletion has to be considered  
1137 indeed an important parameters for the efficiency of the signal, and in particular it affects  
1138 the charge released by a particle which cross the sensor (since the signal is proportional to  
1139 the thickness of the epitaxial layer). Given that the chip under examination has a gap in  
1140 the low dose epi-layer (look at chapter 4.1) we were not able to change independently the  
1141 bias of the substrate (PSUB) and of the p-well (PWELL), but they must be kept at the  
1142 same value, differently from other chips, where on which some test has been performed, as  
1143 reported in figure 6.9. A 2D map of the measured output voltage amplitude and resulting  
1144 gain in the case of the PMOS and HV are reported.

1145 Turning down the bias, the depletion region narrows and the efficiency reduces in  
1146 particular in the pixel corner; La soglia si alza di meno di 1/3, mi sarei aspettata un po'  
1147 di più guardando il plot. Attenzione che il plot non è fatto con un ngap, quindi ci sta che  
1148 il guadagno lì cali più bruscamente. poi non si capisce benissimo dalla colormap. Anche

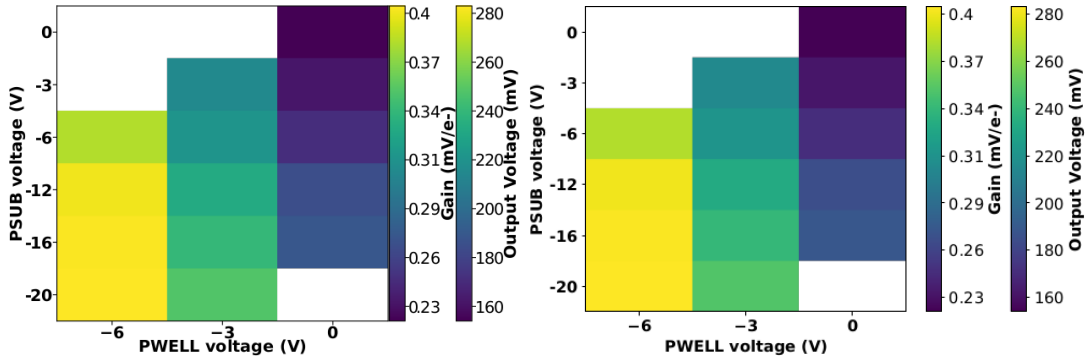


Figure 6.9: 2D map of the output voltage amplitude and gain with respect to the p-well and p-substrate in the case of the PMOS reset front-end (B)

	-6 V	-3 V	0 V
Threshold [DAC]	$20.04 \pm 1.6$	$21.0 \pm 1.6$	$24.5 \pm 1.8$
Noise [DAC]	$0.613 \pm 0.075$	$0.625 \pm 0.078$	$0.822 \pm 0.098$
Slope [au/DAC]	$0.726 \pm 0.027$	$0.707 \pm 0.028$	$0.573 \pm 0.021$
Offset [au]	$-10.8 \pm 1.9$	$-11.2 \pm 1.8$	$-11.1 \pm 1.5$

Table 6.3: The errors are the standard deviations of the corresponding distributions.

1149 la slope diminuisce di circa meno di un terzo. Il noise aumenta leggermente. Il picco del  
 1150 ferro invece si sposta a sinistra di un terzo. Lo spostamento è dovuto alla diminuzione  
 1151 del gain, che influisce sul ToT.

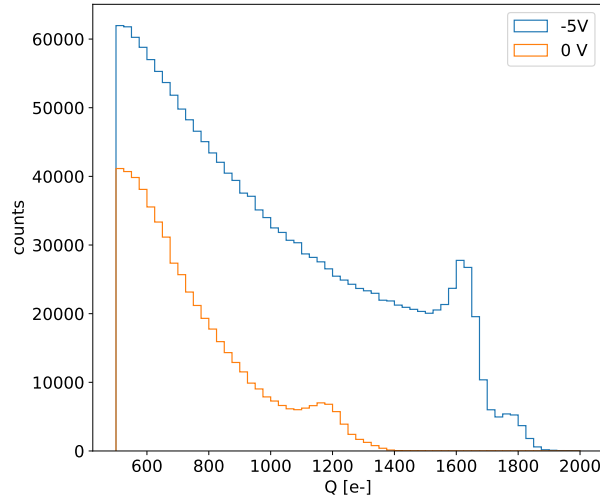


Figure 6.10: Two acquisition with the Fe55 source at different bias.

1152 Potresti dire che a bias più bassi il picco si allarga perchè hai una C più grande e  
 1153 quindi più rumore. In order to look at the changing in the ... ho guardato alla posizione  
 1154 del picco, alla normalizzazione avendo quantificato con una retta. Ho normalizzato tutto  
 1155 a quanto trovato nelle acquisizioni standard. Il fatto che il rate abbia dei piccoli bump

1156 in negativo è probabilmente dovuto al fatto che non ho tenuto ferma la sorgente, ma l ho  
1157 mossa da acquisizione ad acquisizione.

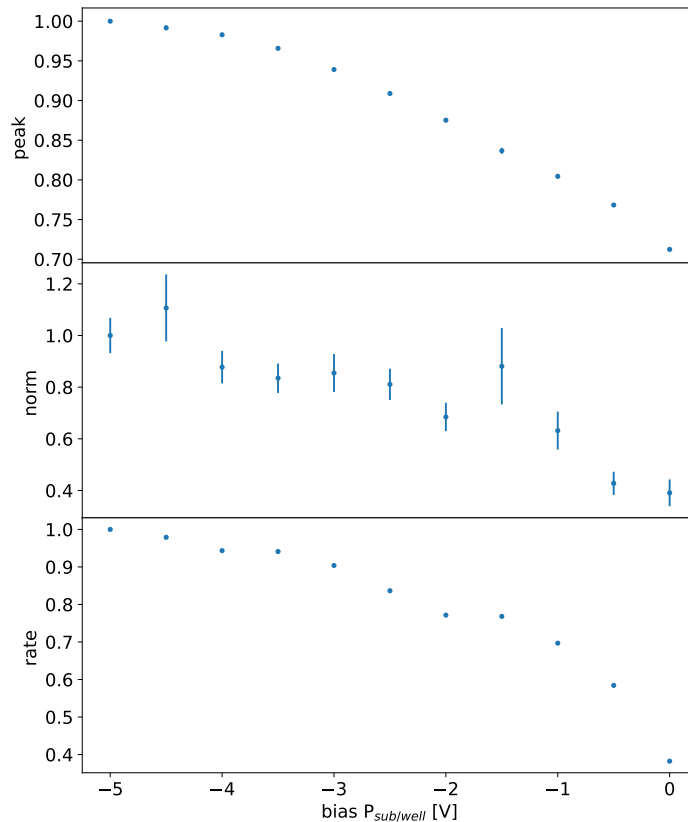


Figure 6.11

### 1158 6.1.5 Measurements with radioactive sources

1159 Signal response characterization using radioactive sources and cosmic rays have been made.  
1160 The Sr90 source emits electrons that: lo spettro ha un cutoff a che E?

1161 **conto/plot sulla differenza elettrone sr e mip.** The signal generated by electrons is sim-  
1162 ilar to the one generated by minimum ionizing particle (MIPS). The spectrum is expected  
1163 to follow a Langau-Gauss distribution

- 1164 • sommato i cluster Spiega la tua definizione di cluster.
- 1165 • plot dello spettro del ferro convertendo in elettroni per il PMOS flavor e facendo la  
1166 somma dei cluster.
- 1167 • di che la tua definizione di cluster è ok perchè sono quasi tutti vicini: plot con la  
1168 distanza e qualche stima delle coincidenze casuali.
- 1169 • mappa di qualche evento di cluster sia per Sr che per FE
- 1170 • istogrammi in carica, con carica sommata di Sr e Fe, oer il flavor PMOS dove hai  
1171 fatto la calibrazione o per tutti?

1172 Spiega che con il flavor HV abbiamo una perdita di segnale, fai vedere uno spettro di  
 1173 delle misure dell'8 marzo.

### 1174 6.1.6 Dead time measurements

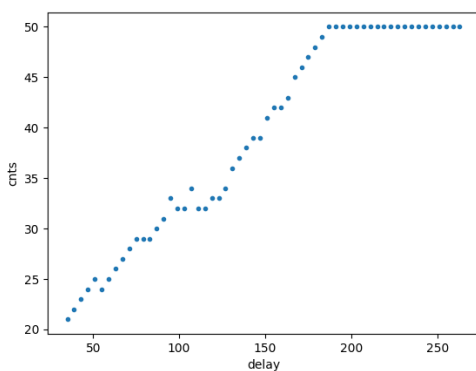
1175 The hit loss is due to analog and digital pile up: the first one occurs when a new hit  
 1176 arrives during the pre-amplifier response, the second instead, which is the more relevant  
 1177 contribution with high rate, while the information of the previous hit has not yet been  
 1178 transferred to the periphery. As only one hit at a time can be stored on the pixel's RAM,  
 1179 until the data have completed the path to get out, the pixel is paralyzed and the dead time  
 1180  $\tau$  almost corresponds with the time needed to transmit the data-packets off-chip. Since the  
 1181 exportation of data from pixel to the EoC occurs via a 21-bits data bus, only one clock  
 1182 cycle is needed to transfer the data to the end of column and the dead time bottleneck is  
 1183 given by the bandwidth of the serializer at the EoC. In our setup the serializer operates  
 1184 at 40 MHz, thus to transmit a data packet (27-bit considering the addition at the EoC)  
 1185 at least 675 ns are needed. For what we have said so far, the R/O is completely sequential  
 1186 and therefore is expected a linear dependence of the reading time on the number of pixels  
 1187 to read:

$$\tau = 25 \text{ ns} \times (\alpha N + \beta) \quad (6.9)$$

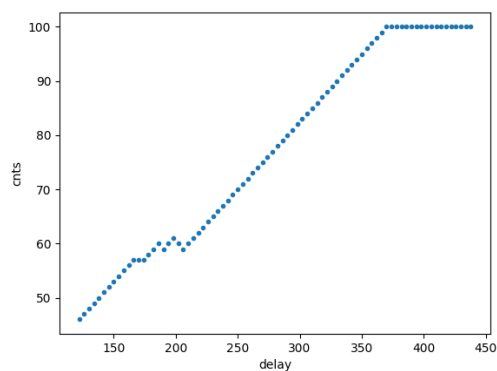
1188 where  $\alpha$  and  $\beta$  are parameters dependent on the readout chain setting.

1189 To measure and test the linearity of the reading time with the number of pixels firing,  
 1190 I have used the injection mode available on the chip. Indeed, the injection mode allows  
 1191 fixing not only the amplitude of the pulse, which corresponds to the charge in DAC units,  
 1192 but also the period and the width. I have injected a fix number of pulses (100) and looked  
 1193 for the rate when the efficiency decreases. Moreover to test that there is no dependence of  
 1194 the digital readout time from the charge of the pulse, I have tried to change the amplitude of  
 1195 the pulse injected, but the parameters found were consistent with the default configuration  
 1196 ones.

1197 Al posto degli esempi con 5 e 10 pixels metterei un esempio dell'efficienza vs il periodo  
 1198 quando leggo un singolo pixel. Una cosa che volevo fare era anche provare a fissare la slope  
 1199 con cui l'efficienza scende: se la slope è uguale per tutti il readout diventa completamente  
 predittivo.



(a) efficiency vs DELAY 5 pixels



(b) efficiency vs DELAY per 10pixels

1200 While the single pixel reading time and the dead time do not depend on the position  
 1201 on the pixel matrix and are equal to 106 (46+60) clock counts within 1 clock count, on  
 1202

Parameter	Value [DAC]	Value [ $\mu$ s]
START_FREEZE	64	1.6
STOP_FREEZE	100	2.5
START_READ	66	1.65
STOP_READ	68	1.7

Table 6.4: Default configuration of the R/O parameters

1203 the other hand the  $\tau$  depends on the pixel position on the matrix when more than one  
 1204 pixel are firing. In particular the priority chain goes from row 224 to row 0, and from col  
 1205 0 to 112, that means the last pixels to be read is the one on le bottom right corner of the  
 1206 matrix.

1207 In figure 6.14 is reported the reading time versus the number of pixels injected; the  
 1208 R/O parameters that control the reading time and their default values are reported on  
 1209 table ??.

1210 The factor  $\alpha$ , referring to eq. 6.9 is proportional to the difference (STOP\_FREEZE  
 1211 - START\_READ), while the offset  $\beta$  lies between 5 and 15 clock counts. Since through  
 1212 the injection a random hit rate on the matrix can't be simulated, as the coordinates  
 1213 of the pixels to inject must be specified, for convenience I used the pixels on the same  
 1214 column/row. No difference in the  $\alpha$  and  $\beta$  coefficients has been observed between the two  
 case.

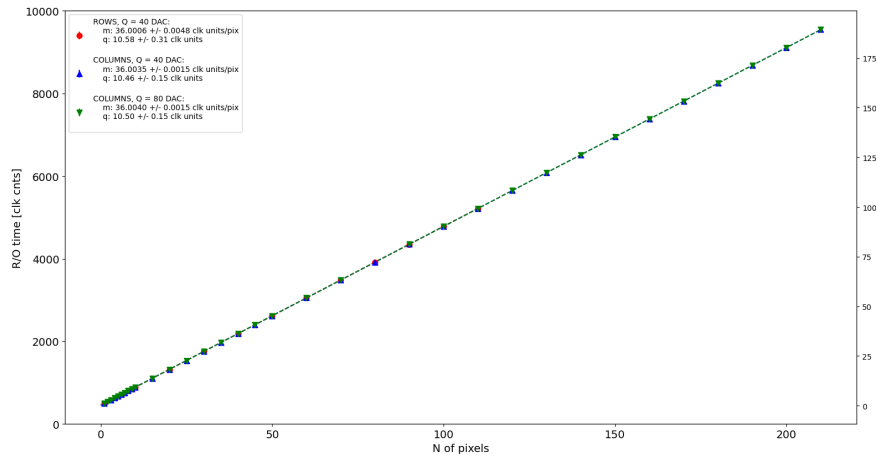


Figure 6.13

1215  
 1216 Ci sarebbe da spiegare perchè i parametri che usiamo noi come default non sono quelli  
 1217 che minimizzano il tempo di lettura. La spiegazione è che "Abbiamo copiato i valori  
 1218 dal repository di quelli di Bonn". Un'altra domanda potrebbe essere: come mai non ho  
 1219 esplorato una zona più vasta per i parametri del R/O. Cambiando molto i parametri del  
 1220 R/O la lettura non funzionava per niente: ad esempio CONF\_STOP\_FREEZE non può  
 1221 essere impostato nè sopra 105 nè sotto 95

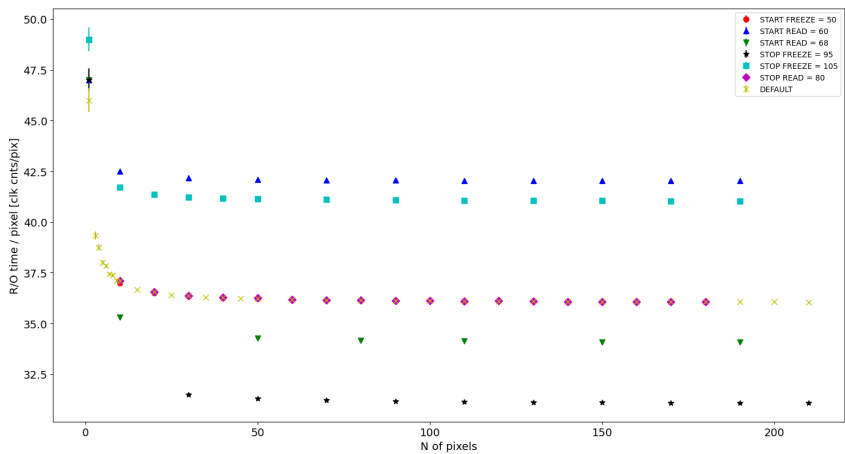


Figure 6.14

## 1222 6.2 ARCADIA-MD1 characterization

<sub>1223</sub> **Chapter 7**

<sub>1224</sub> **Test beam measurements**

<sub>1225</sub> At PRF smaller than 100 Hz, all the dosimeters analyzed have a shorter signal collection  
<sub>1226</sub> time with respect to the repetition time of the pulses (maggiore uguale 10 ms), and,  
<sub>1227</sub> consequently, the saturation is influenced only by the dose-per-pulse (duration of the  
<sub>1228</sub> pulse is around 2.5 us)

<sub>1229</sub> During August 2022 a testbeam took place in Santa Chiara hospital in Pisa, where a  
<sub>1230</sub> new accelerator designed for both medical research and R&D in FLASH-RT, and for this  
<sub>1231</sub> reason called "ElectronFlash", have been installed a few months ago.

<sub>1232</sub> The motivation of the testbeam measurements were testing TJ-Mopopix1 in condition  
<sub>1233</sub> different from the one foreseen during the design and also testing the mechanical and the  
<sub>1234</sub> DAQ setup for other future measurement. TJ-Monopix1 is supposed to be employed for  
<sub>1235</sub> tracking in HEP experiments while our goal was testing the possibility of integrating the  
<sub>1236</sub> charge released by more particles at ultra high hit rate achievable with the accelerator.  
<sub>1237</sub> **Una frase di disclaimer sul fatto che non siamo riusciti a testare quello che volevamo.**

<sub>1238</sub> In medical physics the dose is indeed the standard parameter to characterize the beam  
<sub>1239</sub> because of its obvious relation with the damage caused in the patient: firstly the oncolo-  
<sub>1240</sub> gists prescribe a certain dose taking into account the efficacy of the treatment and then  
<sub>1241</sub> the medical physicists, on the basis of simulations, decide the energy and the intensity of  
<sub>1242</sub> the beams to dispense the prescribed dose amount. By the point of view of the instrumen-  
<sub>1243</sub> tation and the testing on it, a more common and useful parameter is instead the rate or  
<sub>1244</sub> the fluence of particles. The conversion between the two quantity can be found thinking to  
<sub>1245</sub> the definition of dose: it is the concentration of energy deposited in tissue as a result of an  
<sub>1246</sub> exposure to ionizing radiation. Assuming total absorption of electrons in water, defined  
<sub>1247</sub> by law as the ordinary reference medium, the dose can be expressed as:

$$D[Gy] = \frac{NE[eV]}{\rho[g/cm^3]A[cm^2]x[cm]} \quad (7.1)$$

<sub>1248</sub> After having applied the conversion of the energy from eV to J and noticed that  $E/\rho x$   
<sub>1249</sub> roughly corresponds to the stopping power S of electrons in water, a simple estimation of  
<sub>1250</sub> the dose released in water is:

$$D[Gy] = 1.602 \cdot 10^{-10} N[cm^{-2}] S[MeV cm^2/g] \quad (7.2)$$

<sub>1251</sub> **7.1 Apparatus description**

<sub>1252</sub> The accelerator is placed in a bunker inside the hospital: to shield the outdoor from  
<sub>1253</sub> ionizing radiation the bunker has very thick walls of cementum and both the control units

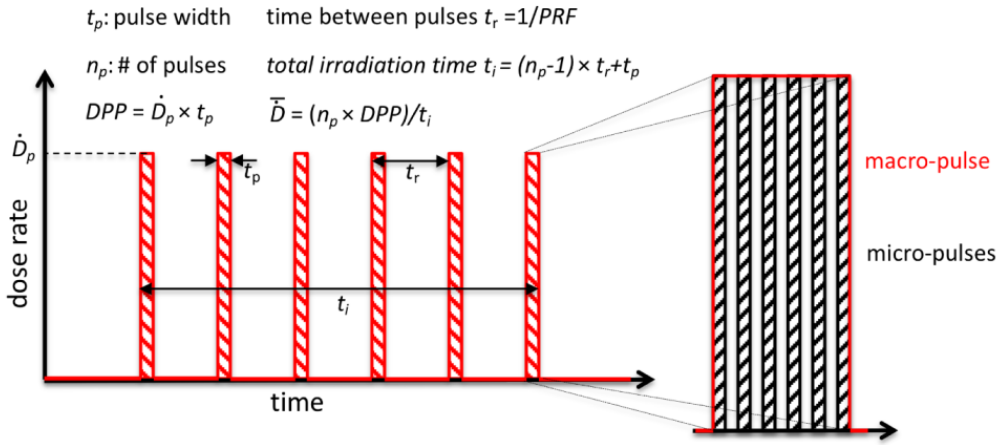


Figure 7.1: Typical beam structure of a beam with the standard characteristic quantity

$\bar{D}$	Dose rate (mean dose rate for a multi-pulse delivery)	0.005-10000 Gy/s
$\dot{D}$	Intra pulse dose rate (dose rate in a single pulse)	0.01-1 $10^6$ Gy/s
DDP	Dose in a single pulse	0.04-40 Gy
PRF	Pulse repetition frequency (number of pulses delivered per unit of time)	1-350 Hz
$t_p$	Pulse width	0.2-4 $\mu$ s
n	Number of pulses	single/pulse train

Table 7.1: The parameters that can actually be set by the control unit are the PRF, DDP,  $t_p$  and n (in particular singular irradiation or pulse train), while the other changes consequently.

1254 of the accelerator and of the detector were placed outside the bunker. For practicability  
1255 reasons the power supply were the only device to be placed inside the bunker.

### 1256 7.1.1 Accelerator

1257 The ElectronFlash accelerator is an electron Linear Accelerator (LINAC) with two energy  
1258 configurations, at 7 MeV and 9 MeV, and it can reach ultra high intensity (40 Gy/pulse)  
1259 keeping the possibility of accessing many different beam parameters and changing them  
1260 independently from each other. This characteristic is fundamental for research in FLASH-  
1261 RT, both for the medical aspects and for the studies on detectors; for example is not really  
1262 clear the dependence of the efficacy of the FLASH effect on the whole dose parameters.  
1263 ElectronFlash is **almost the only one** in the world having this characteristic, **ricontrolla sulla**  
1264 **review, c'era qualcosa che puoi dire.** The accelerator implements a standard beam struc-  
1265 ture for RT with electrons (fig. 7.1), that is a macro pulse divided in many micropulses;  
1266 the parameters used to set the dose and their range of values settable by the control unit  
1267 is reported in table 7.1.

1268 The accelerator is provided of a set of triod cannons  $\sim$ 1.2 m long and with diameters  
1269 from 1 cm to 12 cm and a collimator that can be used as beam shaper to produce a  
1270 squircle shape. The triode, which is made by plexiglass, must be fix to the gun during the  
1271 irradiation and is needed for producing an uniform dose profile (fig.7.2) which is desired  
1272 for medical purpose via the scattering of electrons with the plexiglass.

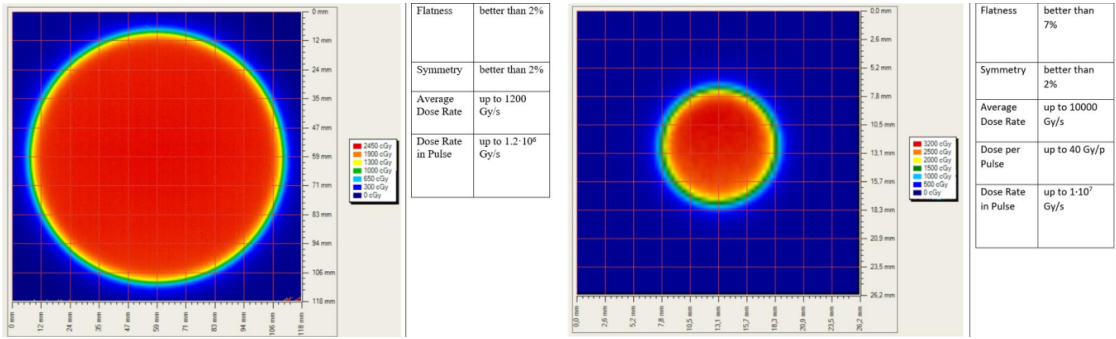


Figure 7.2: Two example of x-y isodose curves for two different triodes, 10 cm and 1 cm respectively, reported by the producer in the manual with the specific of the accelerator (S.I.T. - Sordina IORT Technologies S.p.A.). With the smaller collimator the dose rate in pulse is comparatively higher.

### 7.1.2 Mechanical carriers

The tested detector consists in one chip, the Device Under Test (DUT), mounted on a board and connected to FPGA with same arrangement of figure 7.7. These have been positioned vertically in front of the triode on a table specifically built for the testbeam. The tree board have been enclosed in a box of alluminium with a window on the DUT and with the required holes at the side to enable the biasing via cables and the connection with the DAQ provided via ethernet cable. A trigger signal coming from the control unity and synchronize with the pulses emitted from the beam has been also sent to the FPGA. This signal cannot be considered a trigger signal, since being a prototypes TJ-Monopix1 has been designed to be triggerless, but the time of arrival of this signal, which is saved by the FPGA, can allow the reconstruction of the of the arrival of the bunch during the analysis.

In order to shield the sensor from the whole particles emitted from the gun, two alluminium collimators have been fabricated: one has been positioned at the triode exit while the other in front of the DUT. The collimators are  $t=32$  mm thick and have a diameter  $d$  equal to 1 mm: assuming a beam divergence bigger than  $d/t=1/32 = 1.8^\circ$ , which is the case, the collimator at the triode output was supposed to work as a point source and to reduce the rate on the DUT of a factor at least  $4 \cdot 10^{-4}$ . The second one, being near the DUT, was instead supposed to shield the sensor from the electrons which have passed the first one, except for a region of  $1 \text{ mm}^2$  configurable using *come si chiamano quei cacciavitini per settare la posizione?*.

## 7.2 Measurements

Because of the dead time of TJ-Monopix1 it is not possible resolving the bunch substructure and almost no one pixel can read more than a hit per bunch. I recall, indeed, that the dead time per pixel depends on the location on the priority chain for the readout and for each pixel  $\lesssim 1 \mu\text{s}$  (fig. 7.7) are needed; therefore only a few pixels at the top of the priority chain (at the upper left of the matrix) can fire a second time, since they in principle can be read the first time before the end of the pulse (assuming a pulse duration in  $2 \mu\text{s}-4 \mu\text{s}$ ) and then can be hit again.

Since resolving the single electron track is impossible, a way this sensor could be used

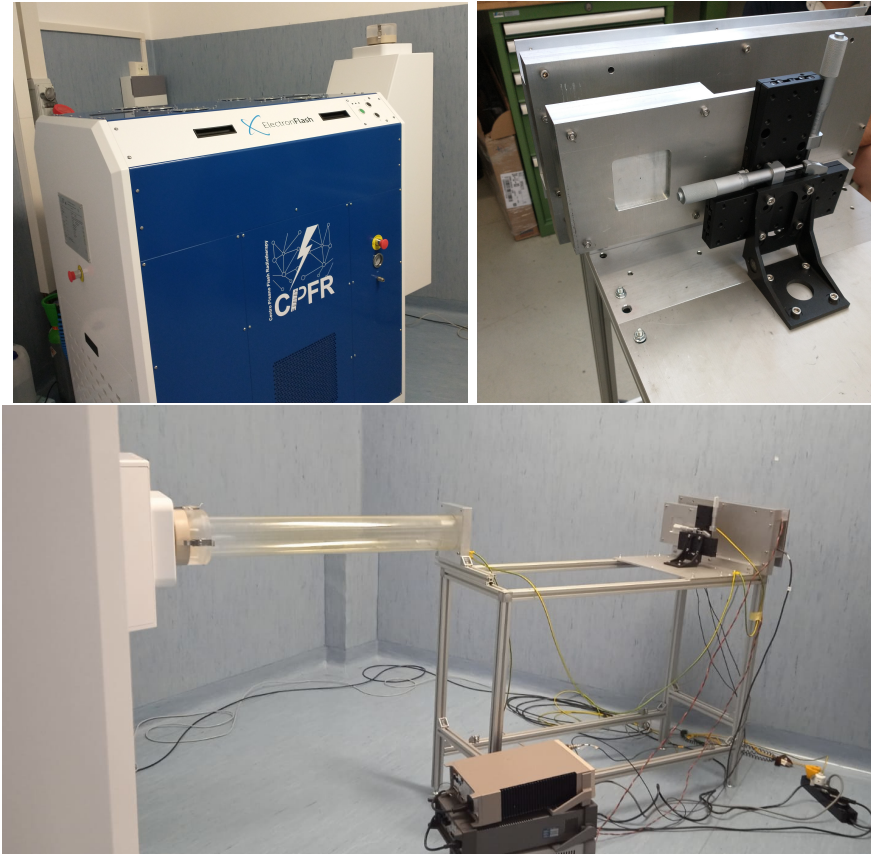


Figure 7.3: Experimental set up. (a) Electron flash accelerator: gantry rotante che consente un orientamento del fascio da 0° 90° (orizzontale / verticale) in tempo reale monitorato da un inclinometro integrato. the gun can be rotated from 90° to 0° (vertical/orizontal). (b) Collimator and DUT box. (c) Whole structure: we used the 10 cm diameter and 1.2 m long triode; the DUT which is in the box behind the two collimators is connected to the power supply units.

1303 in such context is reducing its efficiency and taking advantage of the analog pile up and  
 1304 of the linearity of the analog output (ToT), in order to see a signal produced not by the  
 1305 single particle but by more electrons. Reducing the efficiency and the sensibility of the  
 1306 sensor is essential in order to decrease the high charge signal produced in the epitaxial  
 1307 layer: if the sensor is completely depleted the collection efficiency is closer to 1% and if the  
 1308 whole charges produced by a MIP,  $80 \text{ e}^-/\mu\text{m}$  about, are collected, the saturation limit is  
 1309 soon reach. Then a condition where there is a partial recombination of the center electron-  
 1310 hole created in the bulk is desiderable. On the other hand, the smaller the output signal  
 1311 value and the higher the rate the detector can cope with: indeed, the rollover constitutes  
 1312 a limit for the usage of the analog output. With the standard configuration of the FE  
 1313 parameters and the epitaxial layer completely depleted, a MIP produces a ToT out of  
 1314 range of representation of 6-bit; so as to obtain smaller output signals one can operate  
 1315 on the reduction of the gain of the preamplifier or on the pulse velocity of returnig to  
 1316 the baseline. Recalling the results in section 6.1.4, I have shown that concerning the  
 1317 PMOS flavor 1, reducing the bias from -6 V to 0 V brings a reduction of efficiency down  
 1318 to 40 %, and a reduction in the gain of a factor  $\sim 1/3$ , while the reduction of the gain of  
 1319 the preamplifier allows a reduction of **circa 10, ma da controllare**.

1320 In order to taking advantage of the analog pile up and integrating the charge, for  
 1321 semplicity assume of two electrons, the second one must hit the pixel before the ToT goes  
 1322 under the threshold. The general condition is then  $\overline{\Delta T} < \overline{ToT}$ , but if a high  $P_\mu(n \geq 1)$  is  
 1323 required, a lower  $\overline{\Delta T}$  may be desired:

$$P(n \geq 1) = \sum_{n=1}^{\infty} \frac{e^{-\mu} \mu^n}{n!} = 1 - P(0) = 1 - e^{-\mu} \quad (7.3)$$

1324

$$\mu = \frac{\overline{ToT}}{\overline{\Delta T}} \quad (7.4)$$

1325 If a  $P_\mu(n \geq 1) = 99\%$  then the  $\overline{\Delta T}$  must be  $\sim 0.22 \overline{ToT}$ . The ToT is in range [0,64] but  
 1326 since the rollover must be avoided, the  $\overline{ToT}$  must be lower than 32, and then the minimum  
 1327 rate on the pixel must be 1.25 MHz.

1328

1329 During the testbeam many runs have been performed, spanning the energy, the dose  
 1330 per pulse and the four possible configurations with/without the collimators. We have used  
 1331 the PMOS flavor 1 in the standard configuration: we have biased the PWELL and PSUB  
 1332 at -6 V and set the standard default FE parameters reported in table ???. During all the  
 1333 acquisitions we have used pulses with  $t_p$  of 4  $\mu\text{m}$  and with the smallest PRF settable, which  
 1334 is 1 Hz, in order to start in the most conservative working point exluding the digital pile  
 1335 up of events from different bunch: even if the whole matrix turns on and there are 25000  
 1336 hits, the total readout time corresponding to 25 ms is still lower than the time between two  
 1337 consecutive pulses. The readout starts with the trailing edge of the first pulse going down  
 1338 the threshold,  $\sim 50$  clk = 1.25  $\mu\text{s}$  after this moment the FREEZE signal is sent to the whole  
 1339 matrix, and the trasmittion of the data to the EoC begins. The hits read are the ones  
 1340 whose TE occurred during the 50 clk counts; the ones, instead, whose TE occur during the  
 1341 FREEZE are stored in the pixel memory and read during a second readout. Obviously  
 1342 since the readout of the fist sub-pulse finishes much later than the bunch ends up, each  
 1343 pixel can be store only one hit. An example of the two sub-pulses is shown in figure ???:  
 1344 in the acquisition we injected 5 pulses with both the collimators mounted on the table.  
 1345 Looking at the spectrum *si vede che lo spettro del secondo pulse ha una coda più lunga a*  
*1346 destra: questo è dovuto al fatto che le hit con tot lungo hanno il TE che cade durante il*  
*1347 FREEZE e quindi vengono lette durante il secondo impulso.* On the other hand the 2D  
 1348 histograms, being uniform and not showing disomogenities, suggest that the collimators  
 1349 do not shield all the particles: this was due to a photon background higher than expected.  
 1350 When we have put aside the collimators, instead, the fluence was too high that **the whole**  
 1351 **matrix turns on in 50 clk counts; then the 2 pulses substructure no more appears (fig. 7.6).**  
 1352 **CONTROLLA PERCHÈ PORTEBBE ESSERE UNA CAZZATA**

1353 After the testbeam a simulation of the emission of electrons from the accelerator and  
 1354 their path across the triode and the collimators has been developed via Geant-4 *come si*  
 1355 *ringrazia il lavoro di qualcuno in maniera formale?* The high background we saw although  
 1356 the collimators were mainly produced by electrons Bremsstrahlung during the transition  
 1357 through the alluminium collimators. *dalla simulazione si è visto che nessun elettrone*  
 1358 *arriva sul chip quando ci sono montati i collimatori, mentre nel caso senza collimatori gli*  
 1359 *eventi sono sostanzialmente tutti elettroni (frazione di fotoni prodotti in aria è?).* The  
 1360 photons' simulated spectrum in the three configurations are shown in figure ???. *confronto*  
 1361 *con quello che vedo nello spettro sopra: dati.*

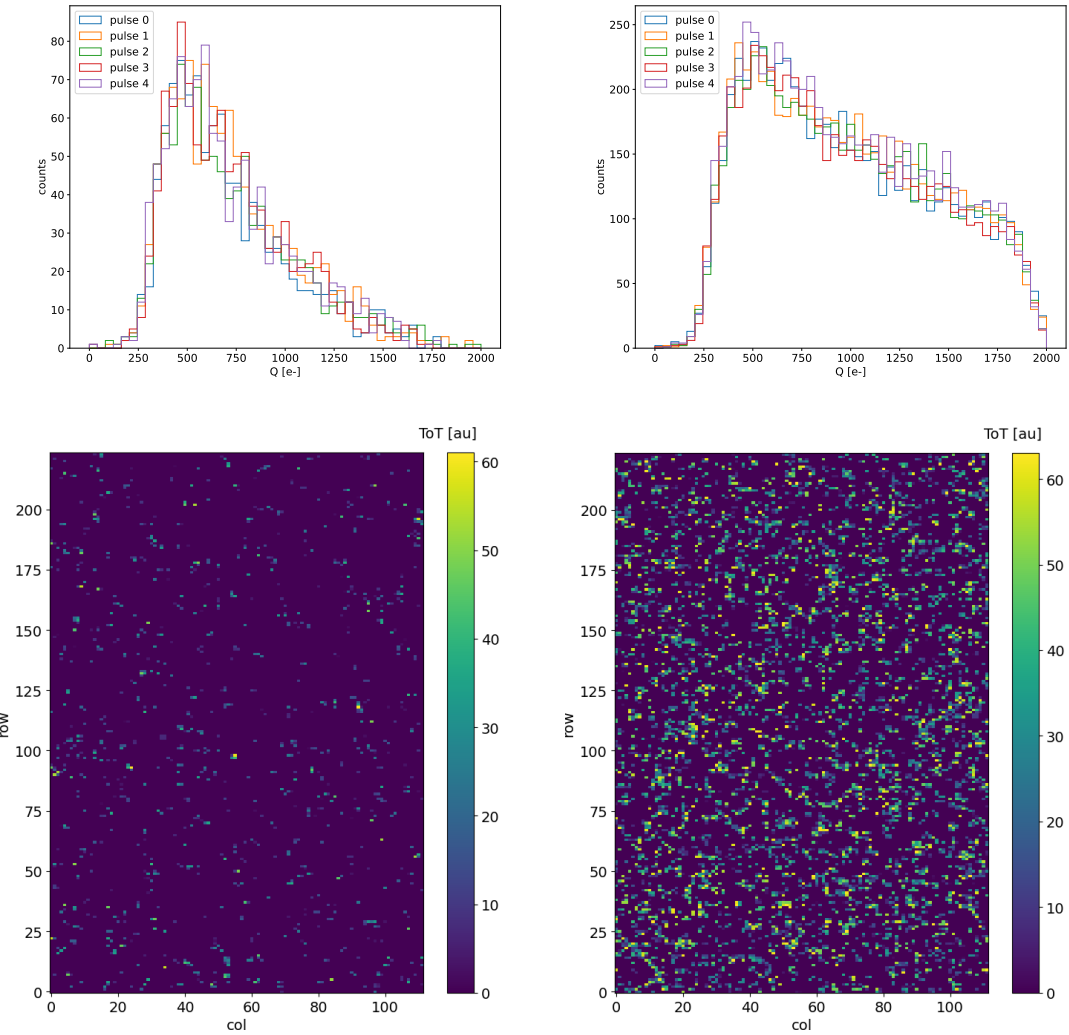


Figure 7.4: Acquisition with both the collimators: 5 pulses at  $DDP=0.07$  Gy. (a) Spectrum of the charge released in the sensor: to apply the conversion I used the information found in the previous chapter. (b) 2D histogram of the ToT of the hits arrived in the sub-pulses.

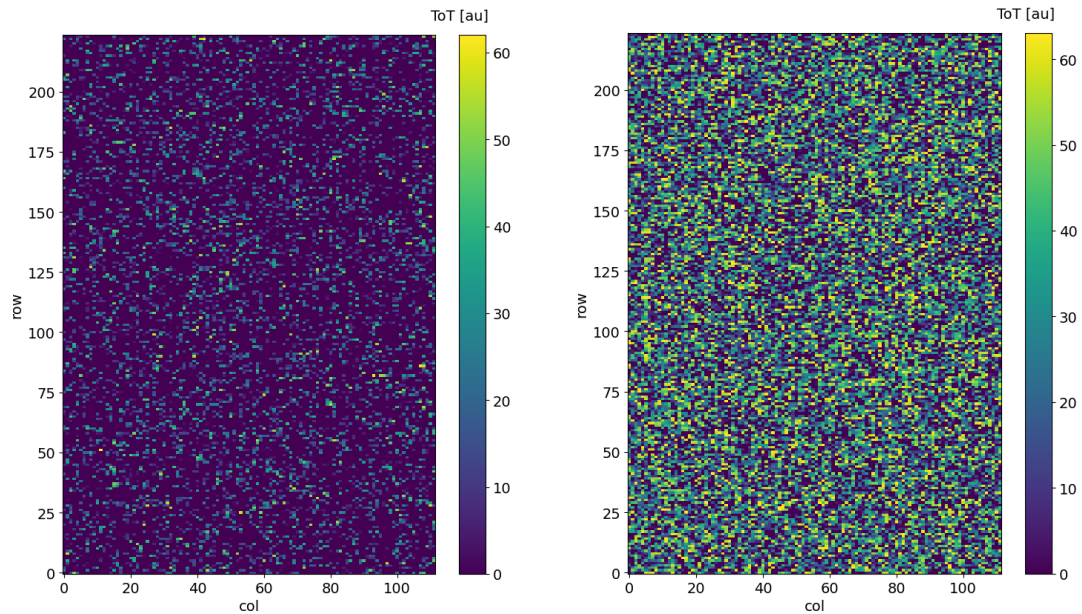


Figure 7.5: Acquisition with both the collimators: 5 pulses at DDP=0.6 Gy. 2D histogram of the ToT of the hits arrived in the sub-pulses. Compared with the previous maps, since the DDP is much higher, more pixels turn on.

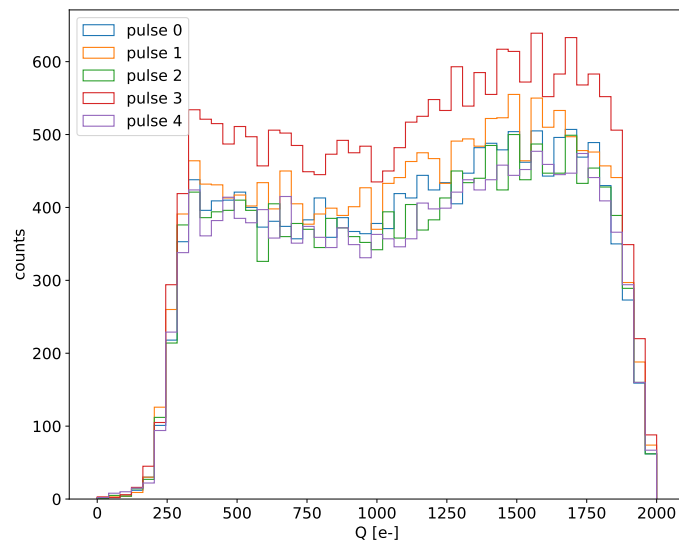


Figure 7.6: Acquisition without any collimator: 5 pulses at DDP=0.04 Gy.

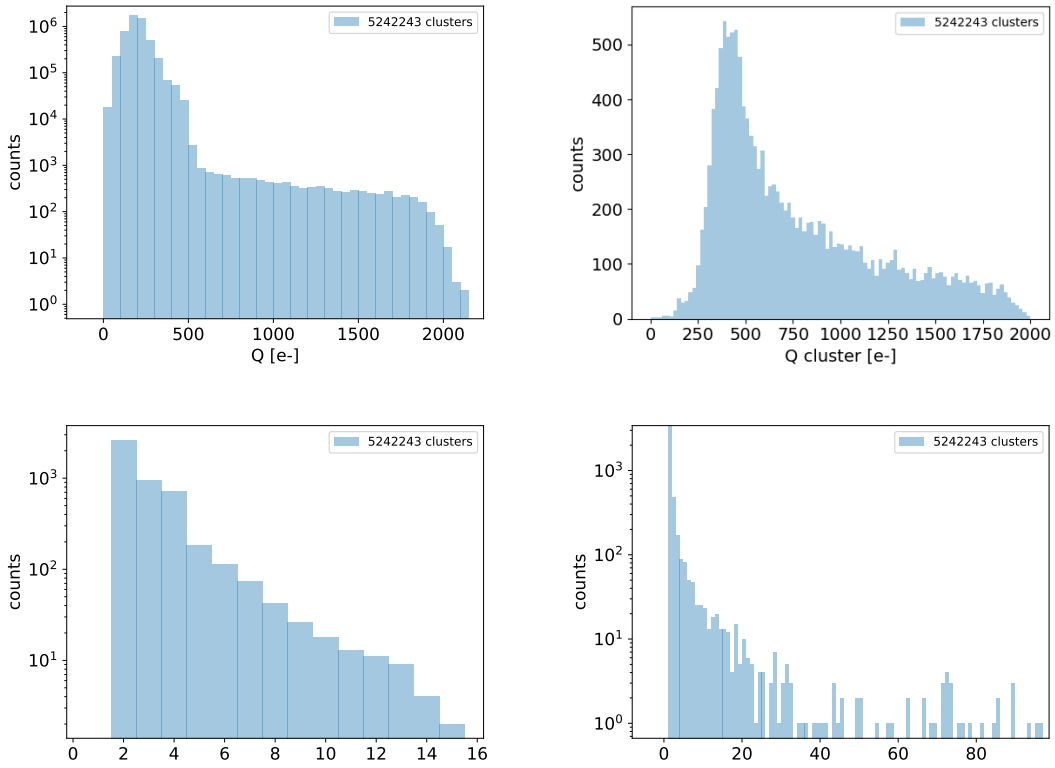


Figure 7.7: plot dei raggi cosmici da rigenerare

- 1362     • plot n di eventi che vedo con le diverse configurazioni
- 1363     • simulazione surya
- 1364     • confronta con misure dello spettro che vediamo senza e con collimatori.

### 1365    7.2.1 MIP spectrum using cosmic rays as source

1366 Since a MIP should produce about  $2\text{ ke-}$  in the epitaxial layer, it should provide a signal  
 1367 that in our conditions (full depletion and high gain) rolls over: in this situation making  
 1368 prediction on the spectrum expected for MIPs becomes hard. Therefore, in order to  
 1369 compare the spectrum observed at the testbeam with one certainly produced by MIP I  
 1370 have made some acquisitions without any radioactive source, in order to look at the cosmic  
 1371 ray events. To be confident with having selected MIPs from cosmic rays and cut the noise, I  
 1372 have selected only the events with multiple hits: these events are mainly clusters produced  
 1373 by the same impinging particle since the random coincidence probability is very low. In  
 1374 fact the cosmic rays and noise rates on the whole matrix are respectively  $0.02\text{ Hz}$  and  
 1375  $\sim\text{Hz}$ , the dead time in such a low occupancy condition can be always approximated with  
 1376  $1\text{ }\mu\text{m}$  (this is not completely true for multiple hits events for which the priority chain  
 1377 should be considered), the random coincidence rate is  $10^{-8}\text{ Hz}$ . Come mai lo spettro in  
 1378 lab è diverso da quello visto con gli elettroni da 9 MeV al santa chiara? Chiedi a Surya il  
 1379 rate visto sul detector senza collimatori.

<sub>1380</sub> **Appendix A**

<sub>1381</sub> **Pixels detector: a brief overview**

<sub>1382</sub> **A.1 Radiation damages**

<sub>1383</sub> Radiation hardness is a fundamental requirement for pixels detector especially in HEP  
<sub>1384</sub> since they are almost always installed near the interaction point where there is a high  
<sub>1385</sub> energy level of radiation. At LHC the  $\phi_{eq}$  per year in the innermost pixel detector is  
<sub>1386</sub>  $10^{14} n_{eq}/cm^2$ ; this number reduces by an order passing to the outer tracker layer [2] pag  
<sub>1387</sub> 341 Wermes. Here the high fluence of particles can cause a damage both in the substrate  
<sub>1388</sub> of the detector and in the superficial electronics.

<sub>1389</sub> The first one has a principal non ionizing nature, due to a non ionizing energy loss  
<sub>1390</sub> (NIEL), but it is related with the dislocation of the lattice caused by the collision with  
<sub>1391</sub> nuclei; by this fact the NIEL hypothesis states that the substrate damage is normalized to  
<sub>1392</sub> the damage caused by 1 MeV neutrons. Differently, surface damages are principally due  
<sub>1393</sub> to ionizing energy loss.

<sub>1394</sub> **DUE PAROLE IN PIÙ SUL SURFACE DAMAGE** A charge accumulation in oxide  
<sub>1395</sub> ( $SiO_2$ ) can cause the generation of parasitic current with an obvious increase of the 1/f  
<sub>1396</sub> noise. Surface damages are mostly less relevant than the previous one, since with the de-  
<sub>1397</sub>velopment of microelectronics and with the miniaturization of components (in electronic  
<sub>1398</sub> industry 6-7 nm transistors are already used, while for MAPS the dimensions of compo-  
<sub>1399</sub>nents is around 180 nm) the quantity of oxide in circuit is reduced.

<sub>1400</sub> Let's spend instead two more other words on the more-relevant substrate damages:  
<sub>1401</sub> the general result of high radiation level is the creation of new energy levels within the  
<sub>1402</sub> silicon band gap and depending on their energy-location their effect can be different, as  
<sub>1403</sub> described in the Shockley-Read-Hall (SRH) statistical model. The three main consequence  
<sub>1404</sub> of radiation damages are the changing of the effect doping concentration, the leakage  
<sub>1405</sub> current and the increasing of trapping probability.

<sub>1406</sub> **Changing of the effective doping concentration:** is associated with the cre-  
<sub>1407</sub>ation/removal of donors and acceptors center which trap respectively electrons/holes from  
<sub>1408</sub> the conduction band and cause a change in effective space charge density. Even an in-  
<sub>1409</sub>version (p-type becomes n-type<sup>1</sup>) can happen: indeed it is quite common at not too high  
<sub>1410</sub>fluences ( $\phi_{eq} 10^{12-13} n_{eq} cm^{-2}$ ). A changing in the doping concentration requires an adjust-  
<sub>1411</sub>ment of the biasing of the sensor during its lifetime (eq.2.2) and sometimes can be difficult  
<sub>1412</sub>keeping to fully deplete the bulk.

<sub>1413</sub> **Leakage current:** is associated with the generation-recombination centers. It has

---

<sup>1</sup>L'INVERSIONE OPPOSTA NON CE L'HAI PERCHÈ?

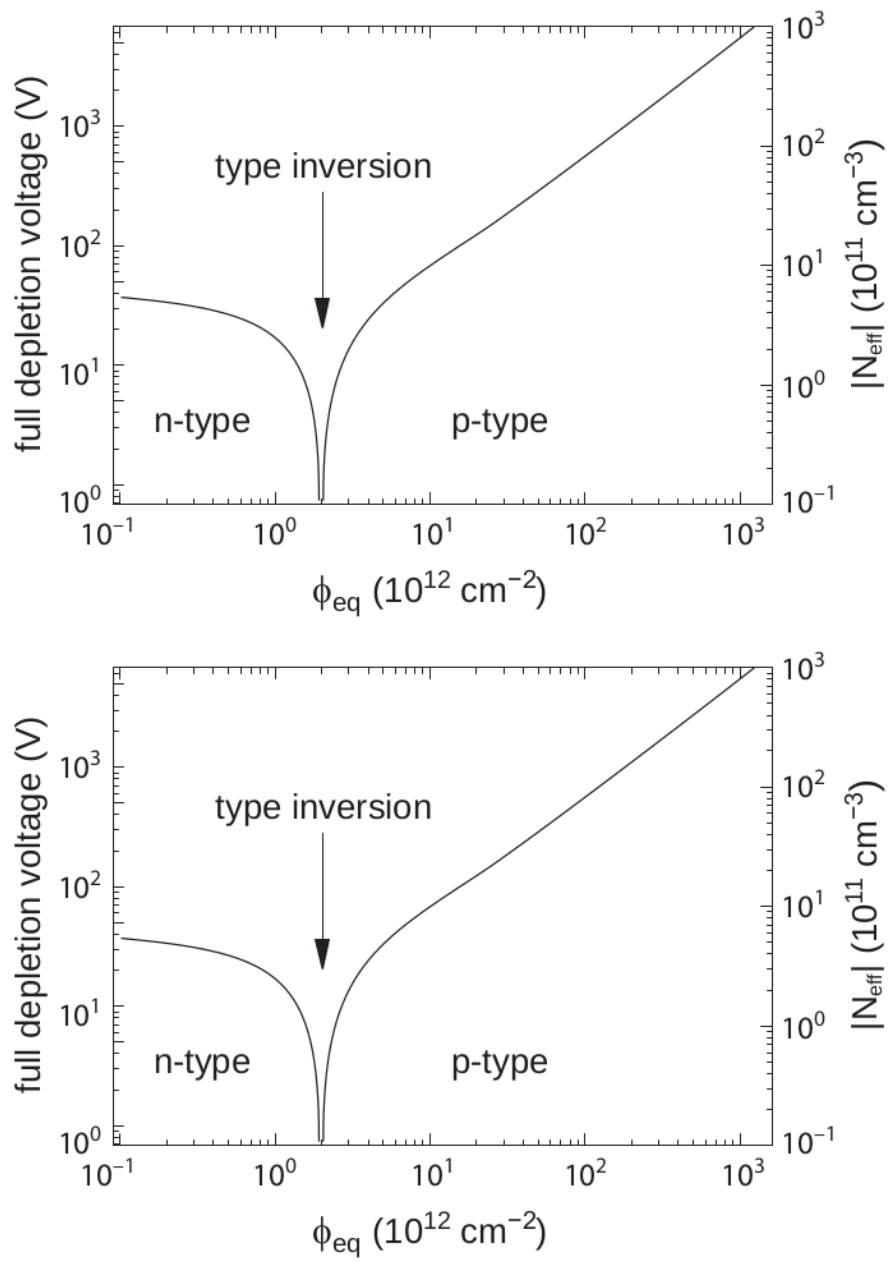


Figure A.1: 1b

1414 a strong dependence with the temperature ( $I_{leak} \propto T^2$ ), whose solution is therefore to  
1415 operate at lower temperature.

1416 **Increase of trapping probability:** since the trapping probability is constant in the  
1417 depleted region, the collected charge decreases exponentially with the drift path. The  
1418 exponential coefficient, that is the mean trapping path, decreases after irradiation and  
1419 typical values are 125-250  $\mu m$  and must be compared with the thickness of the depleted  
1420 region which () corresponds to the mean drift path.

1421 Different choices for substrate resistivity, for junctions type and for detector design are  
1422 typically made to fight radiation issues. Some material with high oxygen concentration  
1423 (as crystal produced using Czochralki (Cz) or float-zone (Fz) process (**CONTROLLA**  
1424 **LA DIFFERENZA TRA I DUE**)) for example, show a compensation effect for radiation  
1425 damage; another example is the usage of n+ -in-p/n sensors (even if p+ -in-n sensors are  
1426 easier and cheaper to obtain) to get advantage of inversion/to have not the inversion (since  
1427 they are already p-type). After inversion the n+p boundary, coming from n+ in-n, but to  
1428 keep using the sensor the depletion zone still must be placed near the diode.

1429 Single Event Upset, in sostanza è quando un bit ti cambia valore (da 0 a 1 o viceversa)  
1430 perché una particella deposita carica nell'elettronica che fa da memoria registro/RAM/....  
1431 Questo tipo di elettronica ha bisogno di un sacco di carica prima che il bit si "fippi"  
1432 (cambi valore), infatti tipicamente per avere un SEU non basta una MIP che attraversa  
1433 esattamente quel pezzo di chip in cui è implementata la memoria, ma un adrone che faccia  
1434 interazione nucleare producendo più carica di quanto farebbe una MIP. Questo metodo pur  
1435 essendo più comodo richiede less amount of area ha però come drawback che il registro può  
1436 essere soggetto a SEU problema non trascurabile in acceleratori come HL-LHC adronici

# <sup>1437</sup> Bibliography

- 1438 [1] W. Snoeys et al. “A process modification for CMOS monolithic active pixel sensors  
1439 for enhanced depletion, timing performance and radiation tolerance”. In: (2017).  
1440 DOI: <https://doi.org/10.1016/j.nima.2017.07.046>.
- 1441 [2] H. Kolanoski and N. Wermes. *Particle Detectors: Fundamentals and Applications*.  
1442 OXFORD University Press, 2020. ISBN: 9780198520115.
- 1443 [3] E. Mandelli. “Digital Column Readout Architecture for 10.1109/NSSMIC.2009.5402399  
1444 the ATLAS Pixel 0.25 um Front End IC”. In: (2002).
- 1445 [4] M. Garcia-Sciveres and N. Wermes. “A review of advances in pixel detectors for  
1446 experiments with high rate and radiation”. In: (2018). DOI: <https://doi.org/10.1088/1361-6633/aab064>.
- 1448 [5] C. Marinas. “The Belle-II DEPFET pixel detector: A step forward in vertexing in the  
1449 superKEKB flavour factory”. In: (2011). DOI: [doi:10.1016/j.nima.2010.12.116](https://doi.org/10.1016/j.nima.2010.12.116).
- 1450 [6] J. Baudot. “First Test Results Of MIMOSA-26, A Fast CMOS Sensor With Inte-  
1451 grated Zero Suppression And Digitized Output”. In: (2010). DOI: [doi:10.1109/NSSMIC.2009.5402399](https://doi.org/10.1109/NSSMIC.2009.5402399).
- 1453 [7] A. Dorokhov. “High resistivity CMOS pixel sensors and their application to the  
1454 STAR PXL detector”. In: (2011). DOI: [doi:10.1016/j.nima.2010.12.112](https://doi.org/10.1016/j.nima.2010.12.112).
- 1455 [8] Giacomo Contin. “The STAR MAPS-based PiXeL detector”. In: (2018). DOI: <https://doi.org/10.1016/j.nima.2018.03.003>.
- 1457 [9] Nolan Espplen. “Physics and biology of ultrahigh dose-rate (FLASH) radiotherapy:  
1458 a topical review”. In: (2020). DOI: <https://doi.org/10.1088/1361-6560/abaa28>.
- 1459 [10] Fabio Di Martino et al. “FLASH Radiotherapy With Electrons: Issues Related to  
1460 the Production, Monitoring, and Dosimetric Characterization of the Beam”. In:  
1461 *Frontiers in Physics* 8 (2020). ISSN: 2296-424X. DOI: [10.3389/fphy.2020.570697](https://doi.org/10.3389/fphy.2020.570697).  
1462 URL: <https://www.frontiersin.org/articles/10.3389/fphy.2020.570697>.
- 1463 [11] M. Dyndal et al. “Mini-MALTA: Radiation hard pixel designs for small-electrode  
1464 monolithic CMOS sensors for the High Luminosity LHC”. In: (2019). DOI: <https://doi.org/10.1088/1748-0221/15/02/p02005>.
- 1466 [12] M. Barbero. “Radiation hard DMAPS pixel sensors in 150 nm CMOS technology  
1467 for operation at LHC”. In: (2020). DOI: <https://doi.org/10.1088/1748-0221/15/05/p05013>.
- 1469 [13] K. Moustakas et al. “CMOS Monolithic Pixel Sensors based on the Column-Drain  
1470 Architecture for the HL-LHC Upgrade”. In: (2018). DOI: <https://doi.org/10.1016/j.nima.2018.09.100>.

- 1472 [14] I. Caicedo et al. “The Monopix chips: depleted monolithic active pixel sensors with  
1473 a column-drain read-out architecture for the ATLAS Inner Tracker upgrade”. In:  
1474 (2019). DOI: <https://doi.org/10.1088/1748-0221/14/06/C06006>.
- 1475 [15] D. Kim et al. “Front end optimization for the monolithic active pixel sensor of the  
1476 ALICE Inner Tracking System upgrade”. In: *JINST* (2016). DOI: doi:10.1088/  
1477 1748-0221/11/02/C02042.
- 1478 [16] L. Pancheri et al. “A 110 nm CMOS process for fully-depleted pixel sensors”. In:  
1479 (2019). DOI: <https://doi.org/10.1088/1748-0221/14/06/c06016>.
- 1480 [17] L. Pancheri et al. “Fully Depleted MAPS in 110-nm CMOS Process With 100–300-  
1481 um Active Substrate”. In: (2020). DOI: 10.1109/TED.2020.2985639.